Colloidal Lead Sulphide Nanostructures for Optoelectronics Applications

Paul Giraud

Exeter College

University of Oxford

A thesis submitted in fulfilment of the requirements for the degree of

Doctor of Philosophy in Engineering Science

Michaelmas Term 2019

Colloidal Lead Sulphide Nanostructures for Optoelectronics Applications

Paul Giraud, Exeter College, University of Oxford

ABSTRACT

Colloidal semiconductors are nanosized semiconducting materials that are grown in solution and dispersed in solvents. Since the first synthesis reports of colloidal nanocrystal quantum dots in the early 1990s, considerable progress has been made, enabling the production of monodisperse colloids that are tunable in size and shape over a wide range of semiconductors and alloys. In recent years, the deployment of these nanocrystals , has been considered in numerous optoelectronic devices such as solar cells, photodetectors, and light emitting diodes, covering areas as diverse as renewable energies, communications, medical imaging, displays, and lighting.

Lead sulphide (PbS) colloidal nanocrystals stand out, following ground-breaking discoveries in energy harvesting and near infra-red (NIR) photodetection. In order to achieve successful integration in the next generation of commercially available devices, several improvements must be made at the material, device, and manufacturing level. This thesis attempts to address these challenges by focusing on the application of PbS colloidal nanowires and quantum dots in NIR photodetection. Field effect transistors have been fabricated to study the transport properties of PbS nanowires and it is shown that p-type mobilities can reach values as high as 160 $cm^2V^{-1}s^{-1}$ thanks to the high degree of crystallinity. The devices also showed interesting photo-response behaviour in the infrared with a responsivity as high as 1.9×10^4 A/W, together with response times of the order of 30 ms.

Hybrid devices consisting of PbS nanowire FETs capped with PbS QDs were also made for the first time thanks to an innovative fabrication technique involving the dry printing of PbS QDs. It was shown that such hybrid structures exhibited substantial reduction in gate voltage hysteresis, which was attributed to charge transfer occurring at the QD/nanowire interface, helping to passivate localized trap states in the nanowire. PbS QDs were also used as standalone active materials in IR photodetectors. The impact on device performance of ligand exchange, a strategy used to increase the conductivity of QD films, was investigated in a study of two commonly used ligands, namely 1,2-Ethanedithiol (EDT) and tetrabutylammonium (TBAI). EDT-exchanged films showed better conductivity in the dark but a lower photosensivity than the TBAI-treated films.

The study on ligands served as a basis for the design of two photodetection devices, starting with the fabrication of nanogap Schottky photodiodes consisting of ligand exchanged PbS QDs that were sandwiched between gold (Au) and aluminium (Al) electrodes, with spacings of only a few tens of nanometres. The electrodes were made via adhesion lithography, a novel fabrication technique that holds great promise for probing charge transport properties as well as for large scale manufacturing of devices. The devices fabricated in this work exhibited a responsivity of R = 38.7A/W in reverse bias combined with a detectivity of 3.5×10^{12} and a bandwidth of 180 Hz. These results highlight the compatibility of colloidal PbS QDs with adhesion lithography fabrication processes for the development of IR detectors for the next generation of flexible and transparent electronics. The second type of devices consisted of patterned photodetectors made from printed micro arrays of PbS QDs. It was shown that transfer printing was a suitable method for the patterning of such devices and offered a viable alternative to commonly used non-patternable deposition techniques such as spin-coating. Because of the versatility in the process, it was also shown that this technique could be used with transparent and plastic substrates, leading to the realisation of transparent flexible photodetectors made of PbS QDs.

ACKNOWLEDGEMENTS

This thesis is the result of a long effort, which I could never have endured without the help and support of many, whom I would like to thank presently. I first begin with Professor Jong Min Kim who gave me this incredible opportunity. His patience and continuous support were instrumental in the completion of this work. I would also like to thank Professor Stephen Morris who took over as main supervisor after the departure of Professor Kim. His guidance and mentoring were invaluable to me, especially towards the latter stages of this work It is honest to state that this thesis would never have been finished without his backing. Professor Seung Nam Cha also played a significant role in this endeavour, I greatly benefited from his vast knowledge and expertise in the field of nanowires and quantum dots and for that I am extremely grateful.

I would also like to thank my colleagues, post-docs and DPhil students alike, with whom I have worked over the years. Bo Hou has been a great friend and mentor, especially in the first years when he undertook my training in the lab. Sangyo Lee, whose eternal good mood was deeply contagious and cheered me up many times. Yuljae Cho has always given me great advice and gave me the opportunity to improve my device modelling and simulation skills! John Hong who travelled with me to Korea and introduced me to the wonders of the Korean culture. I would particularly like to thank John and his family for welcoming me during my stay, they helped make this experience unforgettable. I am not forgetting Sangyeon Pak and the many fruitful discussions we had which significantly helped improving the quality of my research. I also have a particular thought for the former members of the group: Byung Sung Kim, Jong Bae Park, YoungWoo Lee, A-Rang Jang and thank them for their solicitude and helpfulness.

I had the opportunity to be part of a collaboration with the Department of Physics at Imperial College and am grateful to Dr Dimitra Georgiadou who supervised me on the project. Her rigorous approach to scientific work contributed to make me a better researcher. My gratitude also goes to Dr

Jonchul Lim from Professor Henry Snaith's group who kindly did transient spectroscopy analysis on the project.

My time at Oxford has been blessed with many new friendships which have helped me to put up with the hardships of the DPhil work. I thank my friends from the Exeter College MCR and especially those of the infamous 'tonight' group chat with whom I made the most of the Oxford social scene. My warmest gratitude also goes to the people of the Soft Matter Photonic group: Ellis, Chloe, John and Dave, who kindly welcomed me as one of theirs. I am also grateful to Br Joseph Bailham and Fr Paul Rowse of the Blackfriars community, as well as Dr Meriel Raymond, who all were the sources of great spiritual support. I am no less grateful to my housemates Marta, Pierre, and Nomi who put up with me during the last couple of years at Oxford. They made our home a haven of joy and positivity, and for that I cannot thank them enough. I am not forgetting my lifelong friends from my high school and undergrad years whose unconditional trust and support over the years has been an ever-giving and undeserved gift. Gonzague Saint-Paul has once again stepped up in arranging our Wednesdays chats which were tremendously helpful and comforting. He has been a mentor and role model since my teenage years, and I will forever be indebted to him for the many ways in which he has contributed to shape my thinking and perspectives on life.

Finally, I would like to express my deepest gratitude to my parents, Pascal and Isabelle, as well as my siblings and their families Pia, Guylain, Sixtine, Flavien, Baudouin, Gautier, and my grandmother Monique for their bottomless and unconditional love. I will never be able to thank my dad enough for his backing and moral support which has driven me over the years in many uncountable ways and without which I could never have finished this work. I would also take some time to remember my grandparents, Emile and Christiane Spy, who accompanied me since the beginning of my studies and left us during the completion of this work. This thesis is dedicated to their memory.

CONTENTS

LIST OF FIGURES

LIST OF TABLES

PUBLICATIONS

Chapter 4

Paul Giraud, Bo Hou, Sangyeon Pak, Jung Inn Sohn, Stephen Morris, SeungNam Cha, and Jong Min Kim. 2018. "Field Effect Transistors and Phototransistors Based upon P-Type Solution-Processed PbS Nanowires." *Nanotechnology* 29 (7). https://doi.org/10.1088/1361-6528/aaa2e6

Chapter 6

Paul Giraud, Georgiadou, Dimitra, Bo Hou, John Hong, Jongchul Lim, SeungNam Cha, Thomas Anthopoulos, Steve Morris, and Jong Min Kim. "PbS Quantum Dot Photodiodes based on asymmetric coplanar nanogap electrodes." *In preparation.*

Chapter 7

Paul Giraud, Sanghyo Lee, Bo Hou, Yuljae Cho, John Hong, SeungNam Cha, Steve Morris , and Jong Min Kim, "Transfer printed micropatterned PbS quantum dot photodetectors for flexible electronics." *In preparation.*

Others

Yuljae Cho, **Paul Giraud**, Bo Hou, Young-Woo Lee, John Hong, Sanghyo Lee, Sangyeon Pak, et al. 2018. "Charge Transport Modulation of a Flexible Quantum Dot Solar Cell Using a Piezoelectric Effect." *Advanced Energy Materials* 8 (3): https://doi.org/10.1002/aenm.201700809

Yuljae Cho, Bo Hou, Jongchul Lim, Sanghyo Lee, Sangyeon Pak, John Hong, **Paul Giraud**, et al. 2018. "Balancing Charge Carrier Transport in a Quantum Dot P–N Junction toward Hysteresis-Free High-Performance Solar Cells." *ACS Energy Letters* 3 (4): 1036–43. https://doi.org/10.1021/acsenergylett.8b00130

Hong, John, Bo Hou, Jongchul Lim, Sangyeon Pak, Byung-Sung Kim, Yuljae Cho, Juwon Lee, et al. 2016. "Enhanced Charge Carrier Transport Properties in Colloidal Quantum Dot Solar Cells via Organic and Inorganic Hybrid Surface Passivation." Journal of Materials Chemistry A 4 (48): 18769–75. https://doi.org/10.1039/C6TA06835A.

Juwon Lee, Sangyeon Pak, **Paul Giraud**, Young-Woo Lee, Yuljae Cho, John Hong, A-Rang Jang, et al. 2017. "Thermodynamically Stable Synthesis of Large-Scale and Highly Crystalline Transition Metal Dichalcogenide Monolayers and Their Unipolar n-n Heterojunction Devices." *Advanced Materials* 29 (33): 1702206. https://doi.org/10.1002/adma.201702206

Juwon Lee, Sangyeon Pak, Young-Woo Lee, Yuljae Cho, John Hong, **Paul Giraud**, Hyeon Suk Shin, et al. 2017. "Monolayer Optical Memory Cells Based on Artificial Trap-Mediated Charge Storage and Release." *Nature Communications* 8 (March): 14734. https://doi.org/10.1038/ncomms14734

1 INTRODUCTION

1.1 Scope

Optoelectronics combine the physics and engineering of electronic devices that interact with light, whether it be emission, control or detection. They have become ubiquitous in our everyday life through light emitting diodes in displays, photodetectors in smartphone cameras, laser diodes in telecommunications, or solar cells in energy harvesting. Modern optoelectronic devices primarily rely on semiconductors that can convert photons of different energies into electrical signals or vice versa. Historically, devices have been made using inorganic semiconductors such as silicon or alloys from the third and fifth columns of the periodic table (thus known as III-V semiconductors). Their synthesis is made thanks to epitaxial growth methods where bulk crystals are grown via deposition of precursor atoms on a source substrate.

Despite the high quality of the as-grown crystals, epitaxy requires high temperature and pressure growth conditions, and is limited by the nature of the source substrate, which induces strain in the layers due to atomic lattice mismatch. Furthermore, the substrate size ultimately limits the device fabrication throughput and places an upper bound on fabrication costs. The necessity to grow the materials on crystalline substrates also limits the compatibility with plastic substrates and therefore integration with flexible electronics. There has, therefore, been a lot of interest in finding alternative semiconductor synthesis methods, which would ideally be compatible with solution-based processes. These fabrication processes such as spin coating, doctor blading or inkjet printing are low cost and scalable methods that could leverage further reduction in manufacturing costs. It is in this context that the interest in colloidal nanocrystals for optoelectronics has emerged.

Colloidal nanocrystals are nanosized inorganic semiconductors dispersed in solvents. Their existence has been known since as far back as the 19th century with the observation of colour changing gold particles[1]. Likewise, gold and silver colloidal nanoparticles were used by roman glassmakers, albeit probably unknowingly; in the fabrication of dichroic glass as that of the famous Lycurgus Cup, which appears red when light is transmitted through the glass and green when light is reflected from it[2]. However, interest in the field only really developed at the beginning of the 1990s due to the observation of quantum confinement effects in semiconductor nanocrystals [3][4] and the first developments of fully solvent based growth processes[5][6]. Quantum confinement, which is manifested as the ability of semiconductors to change their optical properties as a function of size, focused the research towards the area of optoelectronics with the exciting prospect of spectrally tunable devices relying on nanocrystals as building blocks[7].

Since the initial developments, the ever-improving control on the shape, size, and surface chemistry has placed colloidal nanocrystals as one of the most versatile nanoscale materials, relying on widely available chemical synthesis apparatus for their fabrication, making them easy to produce at the research level in large amounts[8]–[10]. From a nanoscience point of view, colloidal nanocrystals became the perfect technological tool to understand material physics at the nanoscale, especially when compared to resource expensive top-down approaches such as electron beam lithography or bottom up methods such as molecular beam epitaxy.

The synthesis of nanocrystals has been developed for a variety of alloys (II-VI, III-V, IV-VI), however, one class of material, lead chalcogens, has recently stood out as a prime candidate for optoelectronics[11], [12]. Lead chalcogen nanocrystals are IV-VI semiconductors with a PbX composition of lead (Pb) and X standing for sulphur (S), selenium (Se), or tellurium (Te). Over the past decade they have been at the heart of colloidal nanocrystal research with notably ground-breaking discoveries in energy harvesting and infra-red (IR) photodetection. Due to improved understanding of

the carrier dynamics and better passivation strategies, solar cells based on PbS colloidal quantum dots reached power conversion efficiencies above 10% thus offering an alternative to organic devices for low cost solar energy harvesting[13]. PbS quantum dots are particularly efficient at absorbing light in the near infrared (NIR) ranging from 750nm to 2400nm, a spectral range of interest in many applications since it is the realm of standard optical communications (1300nm to 1550nm). In addition, it is also of interest in biological imaging as there exists transparent windows, which are required for deep tissue imaging, between 840 nm and 1680 nm. Infrared PbS QDs photodetectors such as hybrid photoconductors composed of PbS quantum dots and 2D materials (graphene, molybdenum disulphide) have achieved high photodetection performances, on a par with current state-of-the-art photodetectors[14], [15]. Because of their solution processability, colloidal nanostructures are also considered for use in the next generation of flexible and transparent devices, where the integration of standard semiconductors have proven difficult due to the need for low temperature processing. In this context, flexible electronic devices such as field effect transistors (FETs), inverters, and ring oscillators have been made using colloidal quantum dots and colloidal nanowires showing a promising alternative to the silicon CMOS technology that currently dominates this area[16], [17].

1.2 Aim

Despite the advances of the last few years, several challenges must be addressed to secure the integration of colloidal nanostructures, and more particularly PbS nanostructures, into future optoelectronic applications. For example, charge transport remains low in PbS devices and this limits their potential. Air stability is also an issue, causing hysteresis and performance degradation in ambient conditions. Moreover, if solution-based fabrication methods are low-cost and low temperature, they come at the expense of difficult integration with other devices, due to the lack of efficient patterning processes. These challenges can be addressed at three different levels:

i. At the material level: by a thorough understanding of the physics and of the interactions at play between the various interfaces of the components.

ii. At the device level: with the successful fabrication and demonstration of high-performance devices, matching the current state of the art.

iii. At the process level: where innovative technologies must be developed to integrate the colloidal semiconductors into current processes in a scalable, reliable and low-cost manner.

In the following thesis, different devices based on PbS colloidal nanostructures are used to study those three aspects. Nanowires (NWs) are used in field effect transistors (FETs) to investigate transport properties of PbS nanostructures and their interactions with surrounding interfaces. Photodetectors based on PbS QDs are also made to explore novel device structures such as coplanar nanogap electrodes. The thesis also reports the integration of PbS QDs using an innovative process, transfer printing. Transfer printing is a 'pick-up and print' deposition method using elastomeric stamps and has shown promises in the integration of QD-LEDs for pixels in displays[18]. This method is scalable, low-cost and compatible with colloidal nanocrystals. Here, it will also be used to demonstrate the integration of PbS QDs with flexible substrates, and as a dry deposition method allowing solvent contamination issues to be bypassed.

1.3 Outline

This work begins with an introductory chapter (Chapter 2) aimed at presenting the concepts and general physics used throughout the thesis. Colloidal nanostructures are presented in detail with a focus on PbS nanocrystals and their synthesis. A review of the working principle of the two main devices used in this work, transistors and photodetectors will also be discussed. Finally, Chapter 2 will close on a summary of the current state-of-the-art in PbS colloidal optoelectronics, to place this work, and its contributions, into context.

In Chapter 3 the experimental methods used for material analysis, device fabrication and characterisation will be described. In addition to the common analysis techniques, such as UV-Vis spectroscopy, scanning electron microscopy…, an emphasis will be put on transfer printing and its kinetics given its importance in the later chapters of the thesis.

The first experimental results will be presented in Chapter 4 where field effect transistors with a channel consisting of single PbS nanowires were made. After having introduced the synthesis of the nanowires, inspired from the synthesis of PbS QDs detailed in Chapter 2 and characterised their crystallography, the fabrication of the devices will be described. The electrical performances of the nanowires will be discussed, using conventional figure-of-merits such as transfer and output characteristics. The optoelectrical response will also be investigated in order to extract the device photoresponsivity and time response. The chapter will conclude with a discussion on an interesting effect observed during the investigation, where the devices showed enhanced performances with aging.

The electrical analysis of the PbS NWs FETs will be further investigated in Chapter 5 with an emphasis on the observed gate voltage hysteresis. A time dependent analysis will be conducted in order to identify the nature of the charge trapping effects assumed to be responsible for the hysteresis. We will also show that it is possible to control the amplitude of the gate hysteresis by fabricating hybrid NW/QDs heterostructures, which can play a role in the trapping/de-trapping mechanisms occurring at the NWs interfaces. The fabrication of the hybrid structures will be based notably on dry transfer printing methods so as to avoid damaging the nanowires with the further use of solvents.

Further investigations on PbS QDs were carried out with the fabrication of IR photodetectors, which will be presented in Chapter 6. The first part of the chapter will focus on QD surface chemistry and how passivation strategies, inspired from the research on PbS QDs solar cells, enable the significant improvement in the device performance. The second part of the chapter will use these passivation techniques in the fabrication of PbS QDs with a novel architecture using coplanar

electrodes separated by a nanosized gap (nanogap). It will be shown that solution processed colloidal QDs integrate perfectly into the nanogap architecture allowing for the realisation of IR photodiodes over a wide range of electrode aspect ratios. This work was carried out in collaboration with Dr Dimitra Papadopoulos from the Department of Physics at Imperial College, London who provided the nanogap electrodes.

Chapter 7 focuses on the patterning of PbS QDs using the transfer printing fabrication method. The design, fabrication, and characterisation of patterned stamps will be presented in detail together with the optimisation of the transfer printing process. As a proof-of-concept, arrays of PbS QDs photodetectors will be fabricated on silicon and glass substrates, together with, to the best of our knowledge, the first fabrication of PbS QDs IRs detectors on transparent, flexible substrates. Possible routes for device performance enhancements will also be discussed.

To conclude, Chapter 8 will summarise the key findings of this work and consider the future opportunities and challenges for PbS colloidal nanostructures in optoelectronics.

2 BACKGROUND AND LITERATURE REVIEW

2.1 Quantum size effects in nanostructures

2.1.1 Quantization of energy

Semiconductors

Semiconductors are materials whose electrical conductivity depends on their energy state. In a semiconductor, the energy levels are separated into insulating (valence) states and conductive states by a forbidden energy gap called the bandgap. The bandgap E_g represents the difference in energy between the lowest conducting energy level for the electrons E_C and the highest insulating level E_V

$$E_g = E_C - E_V. \tag{2.1}$$

If an electron in the valence state receives energy that equals the value of the bandgap then it can transition to the conduction band leaving a positively charged hole in the valence band. The excited electron eventually recombines and loses energy equivalent to the value of the bandgap. In case of radiative recombination, a photon of energy E_g is emitted. Such inter-band transitions between the valence and the conduction bands are the main mechanisms exploited in semiconductor optoelectronics. For instance, in solar cells, absorption of light creates excited charges which can then be collected to generate electricity. Conversely, spontaneous emission is used in LEDs and stimulated emission is used in lasers to create coherent sources of light. The electron-hole pair can remain physically bound by Coulomb attraction; in which case it is considered as a quasi-particle known as an exciton. Typically, the exciton energy is slightly lower than that of the bandgap and leads to below-energy gap transitions and the appearance of an effective bandgap[19].

Quantization of Energy

The dimensions of a semiconductor significantly affect its electrical and optical properties. As the physical dimensions approach nanoscale lengths, they become comparable to the wavelength of the free charge carriers, resulting in spatial confinement. This confinement impacts the nature and the position of the energy levels available for the electron and holes to occupy. Semiconductors of various dimensions are depicted in Figure 2.1. In a 3D bulk solid (Figure 2.1a), the free charges are able to move unrestricted in all directions and their energy is described by the dispersion relation[20]

$$E - E_C = \frac{\hbar^2}{2m^*}\left({k_x}^2 + {k_y}^2 + {k_z}^2\right), \tag{2.2}$$

with k_x, k_y, k_z being the Cartesian the coordinates of the wave vector.

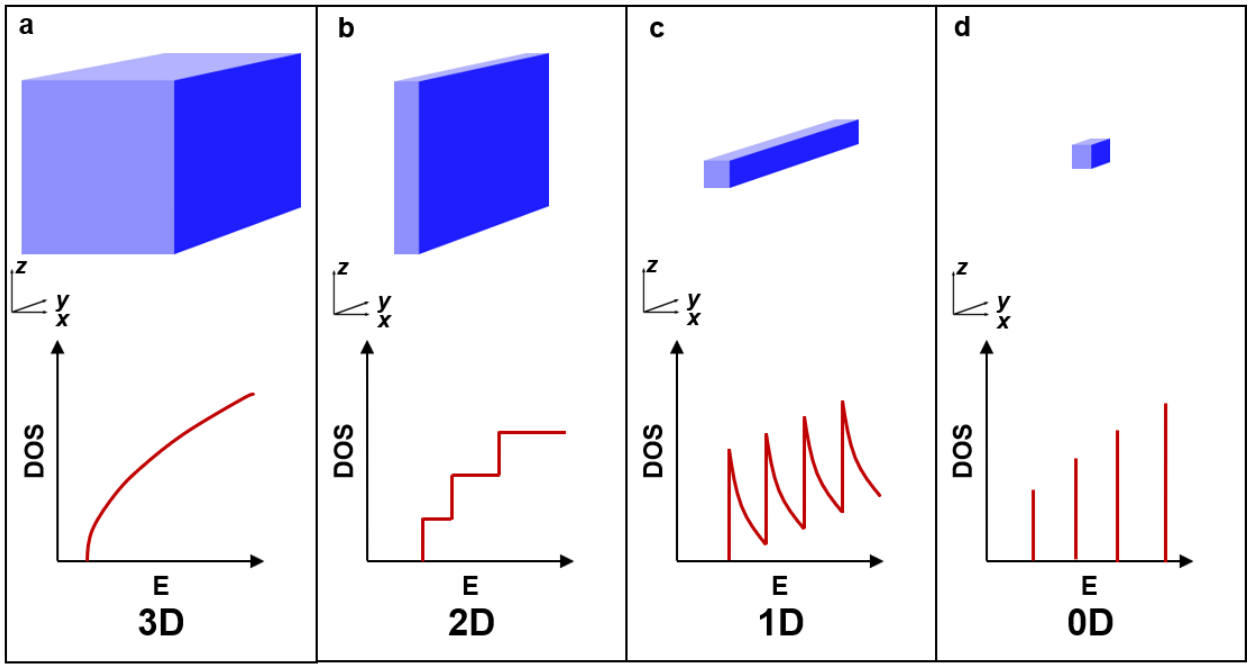

Figure 2.1. Confinement in semiconductors. (top) Schematic representation of the reduced dimensionality of a) bulk, b) 2D, c) 1D, and d) 0D semiconductors with their associated density of states (DOS).

Materials of lower dimensions have one or several dimensions reduced to a few hundred nanometres, confining the motion of the carriers along these directions. This induces a discretization

of the wave vector in the confined direction $k_{x,y,z} = \frac{n\pi}{L}$, with $n \in \mathbb{N}^*$. In two-dimensional materials, such as thin film semiconductors (Figure 2.1.b), quantum wells or monolayered materials (e.g. graphene, molybdenum disulphide), the charges can move freely along two directions (two degrees of freedom) whilst the motion in one dimension is confined. The k-vector is therefore discretized along one direction only. Similarly, one dimensional objects such as nanowires and nanotubes (Figure 2.1c) have only one degree of freedom and the carrier energy is therefore quantized along two directions.

In zero-dimensional structures (Figure 2.1d), the motion of the charges in constricted in all three directions and the energy is thus fully quantized. The confinement of the electrons and holes in all three directions induce strong quantum size effects and these materials are often referred to as quantum dots.

Density of States

Quantum confinement effect directly impacts the distribution of energy levels or density of states (DOS). The density of states describes the number of available energy states available for an electron (hole) over a small interval of energy. The DOS is proportional to the carrier concentration in a material and impacts, therefore, the operation of semiconductor devices. The analytic expressions for the density of states of 3D, 2D, 1D, and 0D semiconductors are plotted in Figure 2.1.

2.1.2 Quantum confinement impact on the bandgap

The bandgap is also affected by the physical dimensions of the semiconductor when it is of the order of the exciton Bohr radius a_b. The exciton Bohr radius represents the distance within which an electron and hole pair remain bound as an exciton. This value is specific to each material and can be expressed as[21]

$$a_b = \varepsilon a_0 m_0 \left(\frac{1}{m_e{}^*} + \frac{1}{m_h{}^*}\right), \tag{2.3}$$

where ε is the semiconductor dielectric constant, $m_h{}^*$ and $m_e{}^*$ are the carrier effective mass for holes and electrons, respectively, m_0 and a_0 are namely the electron mass and the conventional Bohr radius of the hydrogen atom. The Bohr radius gives a good indication of how effectively the quantum confinement is 'felt' in the crystal, with strong confinement effects when the crystal size is lower than this radius. It can be inferred from Equation 2.3 that a low effective masse implies a large Bohr radius, which is a desirable condition for strong confinement. Table 2-1 summarizes the Bohr radii values of common semiconductors from the II-VI, III-V and IV-VI categories. For strong confinement, the value of the bandgap is affected such that

$$E_{g,effective} = E_{g,bulk} + E_{confinement} + E_{exciton} \tag{2.4}$$

where $E_{confinement}$ represents an extra energy term accounting for the quantum confinement and $E_{exciton}$ accounts for the Coulombic attraction between electrons and holes which become important in confinement regime. Following the particle in a box approach [4], for a spherical quantum dot of diameter *R* such that $a_b \ll R$, the bandgap becomes [22]

$$E_{g,effective} = E_{g,bulk} + \frac{h^2\pi^2}{2R^2}\left(\frac{1}{m_e{}^*} + \frac{1}{m_h{}^*}\right) - \frac{1.8e^2}{\varepsilon R}. \tag{2.5}$$

The consequence of Equation 2.5 is that for small enough semiconductors ($R \ll 1$) there is a direct relationship between the material dimensions and its bandgap. For quantum wires and quantum wells, it has been shown that $\Delta E_g = E_{g,effective} - E_{g,bulk}$ also depends linearly on $1/d^2$ with d being respectively the well width or wire diameter[23], [24]. Interestingly, Yu *et al* established that for an identical critical dimension, d, the increase in bandgap due to the confinement followed the ratios $\Delta E_g^{well}/\Delta E_g^{wire}/\Delta E_g^{dot} = 1.00/1.17/2.00$ [25].

Class	Material	E_g (eV)	a_b (nm)
II-VI	CdS	2.48	2
	CdSe	1.73	4
III-V	InP	1.34	8
	InAs	0.35	29
IV-VI	PbS	0.41	18
	PbSe	0.28	55

Table 2-1. Bandgap and exciton Bohr radii of various semiconductors[21].

Figure 2.2 illustrates the size dependent energy level diagram implied by Equation 2.5, which highlights the main feature of quantum confinement in nanostructures: as the size of the material shrinks, the bandgap widens. In terms of wavelength, Planck's relation $E = h\frac{c}{\lambda}$ implies that as the bandgap increases, the absorption wavelength decreases towards UV wavelengths which is sometimes referred to as a blueshift. Therefore, by controlling the semiconductor dimensions, it is possible to control its bandgap and thus its optical properties. This bandgap engineering has great implications in optoelectronics as one could potentially build devices covering the whole UV-IR spectrum using only one class of semiconductors[7]. It is however clear that bandgap engineering relies on the existence of reliable synthesis methods that yield QDs with a narrow size dispersity. Top down techniques, which involve the cleaving of bulk semiconductors into smaller crystals (electron beam lithography, molecular epitaxy) were initially investigated and are still used in quantum information technology and quantum

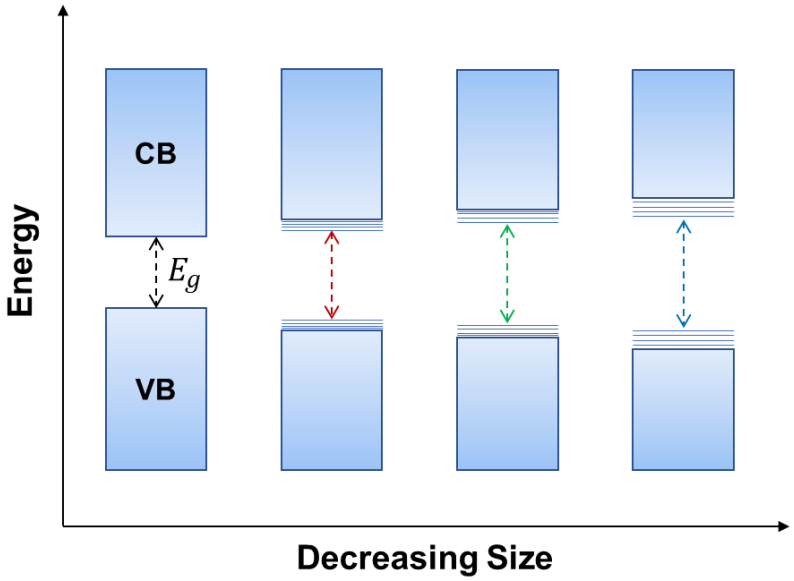

Figure 2.2. Schematic illustration of the quantum confinement effect in semiconductors. As the size of the semiconductor decreases, the bandgap increases, and discretised energy states appear. The smaller the material the more discretised the energy levels become

computing. Unlike top down approaches, bottom up techniques, and particularly chemical procedures such as colloidal synthesis, offer a cheap and scalable way to produce nanomaterials in a controlled manner and therefore present an interest for optoelectronic devices.

2.2 Colloidal nanostructures

2.2.1 Terminology

Colloidal nanostructures are nanomaterials that, as colloids, are dispersed in solvents. As opposed to those fabricated via top-down techniques, they are synthesized in solution via wet chemical processes where the aim is to grow the crystal by gathering inorganic monomers into specific crystalline directions (bottom-up methods)[8]. Whilst colloidal nanocrystals generally refer to inorganic semiconducting quantum dots, in this thesis two different kinds of nanocrystals, namely nanowires and quantum dots have been prepared. Therefore, in this work the term colloidal nanocrystals regroups both solution processed quantum dots and nanowires. Colloidal quantum dots will be referred to as quantum dots and colloidal nanowires as nanowires.

2.2.2 Colloidal synthesis

The wet chemical approaches used in colloidal synthesis have numerous benefits. First, they require widely available chemical equipment and inexpensive chemical precursors, which allows for large batch processing and potential factory-sized scalability. The solution processability is compatible with a range of deposition methods such as spin casting, doctor blading, inkjet printing, nanoimprinting, and transfer printing[16].

Second, during synthesis the tens of thousands of atoms forming the nanocrystals tend to arrange themselves according to the crystalline configurations of the bulk macro-crystal structures from which they are derived. This gives them a high degree of crystallinity, reducing the impact of defects and a necessary requirement for efficient charge transport.

Third, accurate control of the synthesis parameters, such as the reaction time and temperature allow us to obtain quasi-monodisperse size distribution of the nanoparticles. This translates into a narrow distribution of the particle bandgap and therefore narrow optical absorption and emission peaks. More generally, the tweaking of the synthesis parameters gives excellent control over the size and the shape of the nanocrystals. Using the same experimental set-up and similar reaction conditions, one can either obtain quantum dots, nanowires, nanorods, and nanoplatelets, thus opening the way to shape engineering.[26]

Finally, colloidal synthesis allows for efficient surface passivation and functionalization. Colloidal nanocrystals are encapsulated in long, insulating ligands, such as oleic acid (Figure 2.4c). This is a necessary requirement to keep the nanocrystals stable in solution and prevent them from aggregating together. When capped with such long ligands, nanocrystal films have little to no conductivity as there is weak electronic coupling between the nanocrystals and at the interface with the contact electrodes. Whilst these ligands work against efficient charge transport, they can however be exchanged with

shorter ligands in solution (solution ligand exchange)[27] or after deposition (solid state ligand exchange)[28]. Besides increasing the conductivity of the nanocrystal films, these short-length ligands also affect the doping levels of the nanocrystals, meaning that the same nanoparticle can exhibit either p-type or n-type conductivity depending on the nature of the encapsulating ligand[29]. The availability of various ligands offers another degree of functionalization of the nanostructure in addition to the size tunability.

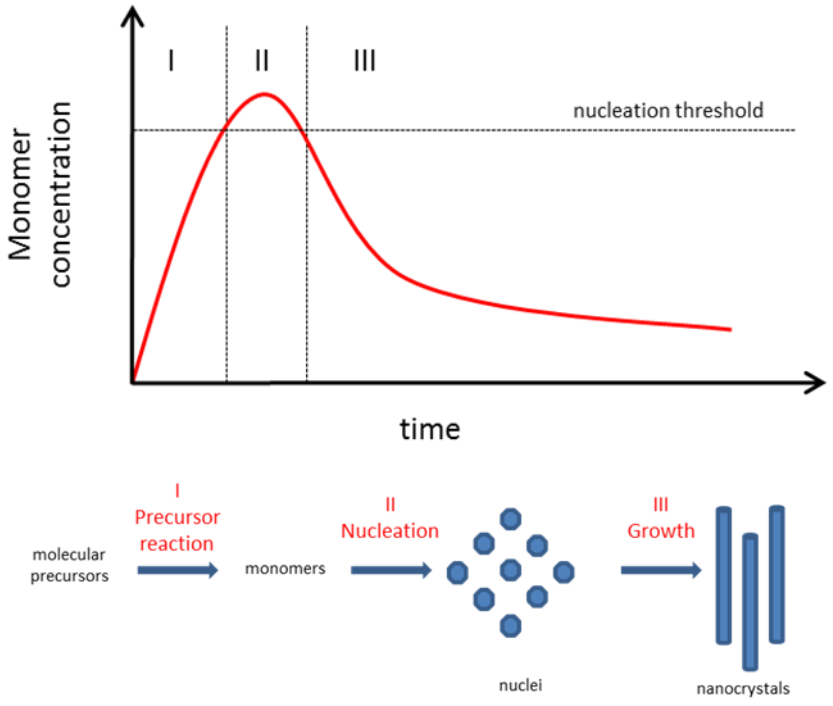

Figure 2.3. Schematic illustrating the solution synthesis of nanocrystals as a function of the concentration of the monomers over time. Bottom panel shows the state of the solution after each stage.

The growth of colloidal crystals is based on the nucleation process whereby nuclei act as seed catalysts around which crystalline monomers condensate[30]. Monomers are nanocrystals building blocks obtained from the reaction precursors. In classical nucleation theory, the nucleation rate is best expressed as: $\frac{dN}{dt} = A\exp\left(-\frac{\Delta G^N}{k_B T}\right)$, where $\Delta G^N = 16\pi\gamma^3 V_m^2/3(k_B T \ln(S))^2$ is the critical free energy, or the energy required to obtain stable particle in the solution, γ is the surface free energy, V_m is the

molar volume, and S is the supersaturation ratio. The supersaturation ratio is defined as the ratio of the concentration of monomers over the solubility of the bulk material. The critical free energy is related to the critical radius by the relation:$\Delta G^N = \frac{4}{3}\pi\gamma r_{crit}^2$. To achieve fast nucleation, a high concentration of monomer must be obtained over a short period of time (LaMer mechanism[21]), necessitating highly reactive precursors. This is best implemented by using the hot injection technique. in which inorganic precursors are quickly injected into a hot solvent. It can be divided into three different successive reactions (Figure 2.3). First, molecular precursors, usually in solid form, are introduced into a hot solution where they undergo a chemical reaction giving rise to monomers i.e. molecules or atoms that are the building blocks of the nanocrystal growth. Once the monomer concentration has reached a nucleation threshold, the monomers nucleate and start aggregating (reaction II). Nucleation subsequently decreases the monomer concentration below the nucleation threshold and no new nuclei can then be formed. A continuous influx of monomers onto the nuclei surfaces promotes the growth of the nanocrystals (reaction III). As time increases, further growth can occur through Ostwald ripening[31], which is driven by the Laplace pressure $p = \frac{2\gamma}{r}$. Smaller particles, with a higher Laplace pressure, will dissolve into monomers and in turn promote the growth of already existing larger nanoparticles. The growth process is quenched by cooling the reaction temperature. All these steps are affected by the presence of the organic ligands, which adhere to the nanocrystal surface during nucleation and growth and are necessary to ensure the stability of the colloids in the solution. Nanocrystals are then dispersed into post-synthesis solvents (toluene, chloroform…) and be used for device fabrication.

2.3 Lead Sulphide nanocrystals

2.3.1 Bulk Lead sulphide

Bulk lead sulphide (PbS) is aIV-VI semiconductor belonging to the lead chalcogenide family PbX (where X= S, Se, Te). PbS has a highly symmetrical rock-salt structure, which consists of two inter-locked face-centred cubic lattices of lead (Pb) and sulphur (S) with a lattice parameter of $a = 5.936$ Å (Figure 2.4a). it is a narrow gap semiconductor with a bandgap of 0.41eV and a photosensitivity covering the near infrared (NIR), the short wavelength infrared (SWIR), and the mid-wavelength infrared (MWIR) range (Figure 2.4d). As such, it was initially used in the first generations of infrared photodetectors[32]–[34]. PbS has similar electron and effective masses, $m_e^* \approx m_h^* \approx 0.08\, m_0$, that are low in value. This in turns means that the exciton Bohr radius is rather large, $a_b = 18$nm (Table 2-1). Confinement can therefore be achieved for crystals with a critical dimension of ≈ 9nm, as it is generally accepted that strong confinement begins at dimensions that are half of the Bohr radius. An advantage of the early onset of confinement in PbS is that it offers greater size tunability and therefore wavelength tunability than other II-VI and III-V nanocrystals as those usually tend to have large hole effective masses. Coupled with the bulk initial narrow bandgap, PbS nanocrystals can cover a wide spectral range showing tunability throughout the entire near-infrared spectrum (Figure 2.4d)[35].

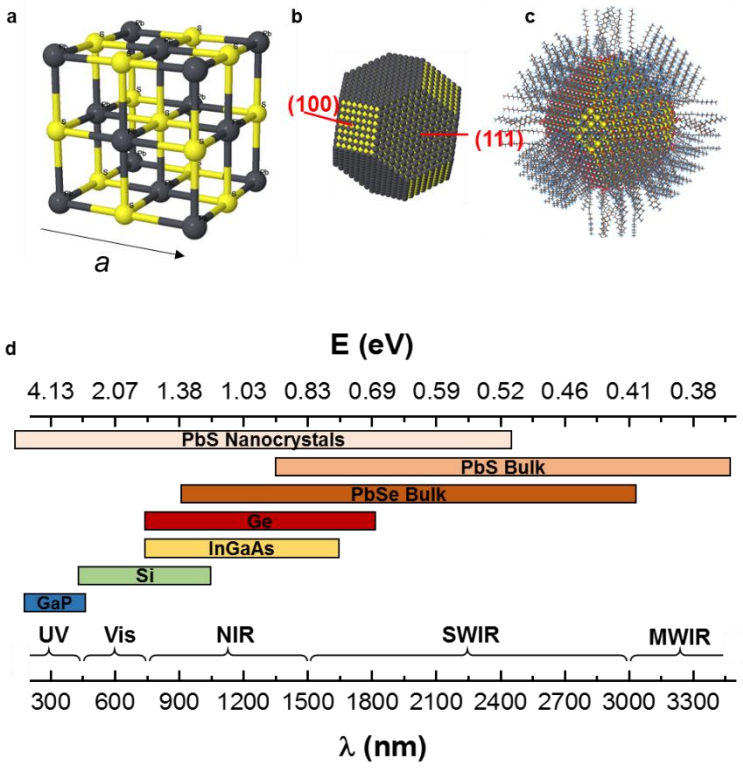

Figure 2.4. a) Rock-salt crystal structure of PbS made of two cubic face-centered lattices of Pb (black) and Sulphur (yellow). b) Crystal structure of a bare 5 nm PbS QD, presenting the (100) and (111) facets plotted with the MPInterfaces code[216] c) Atomic structure of a PbS QD encapsulated with oleic acid ligands. Reproduced from [217] under the license CC BY-SA 3.0. d) Spectral range of common semiconductor used in semiconductors. Adapted from Saran *et al*[11].

2.3.2 PbS Quantum dots

The first colloidal synthesis of PbS quantum dots (PbS QDs) was reported in 2003 by Hines *et al* following the report of the hot-injection process described in Section 2.2.2[36]. In their work, they used lead oxide PbO and bis(trimethylsilyl)sulfide (TMS sulfide) as Pb and S precursors. Oleic acid (OA) played the role of the capping agent, which was necessary to ensure the stability of the colloids. PbO and OA were heated for one hour in an inert environment into which a solution of TMS and octadecene (OE) was rapidly injected to provoke the nucleation stage. Subsequent growth was controlled by time and temperature adjustments before quenching the reaction by cooling the solution. They obtained remarkably narrow size dispersions of 10-15%. The size tunability was achieved by tuning the PbO:OA ratio, which in turn controlled the reactivity of the Pb precursors. The higher the

ratio, the less reactive the Pb monomers, and subsequently the bigger the QD size. Hines suggested adding n-trioctylphosphine (TOP) to the ODE-TMS mixture which was later shown to increase the size distribution and stability of the QDs[37]. Another common method for synthesizing PbS QDs was established by Cademartiri *et al* and involves lead chloride ($PbCl_2$) and elemental sulfur S as the precursors in a solution of oleylamine (OLA)[38]. The size of the PbS QDs ranges from 2-10 nm and the energy size dependence has been modelled and experimentally fitted by the function [39]

$$E_g = 0.41 + \frac{1}{0.0252d^2 + 0.283d}. \tag{2.6}$$

2.3.3 Oriented attachment and growth of PbS nanowires

Just like their bulk counterparts, colloidal nanostructures exhibit clearly defined crystallographic facets. The crystal structure of a PbS QD follows that of a truncated octahedron (Figure 2.4b) with 8 {111} faces and 6 {100} faces[40]. The {111} faces are terminated by either lead or sulphur atoms whereas, the {100} include both. The difference in surface energy causes the ligands to adhere selectively on the crystal faces[41] and can be used to control the nanocrystals growth kinetics and tailor the structures of anything from highly spherical quantum dots, arrows, nanorods, cubes, star shapes to long anisotropic nanowires. For instance, Weller's group reported that the assembly of packed ligands on the {100} PbS surfaces drove the attachment of PbS along their {110} faces[42]. This process, known as oriented attachment[43], is one of the main mechanisms that allows the growth of colloidal nanowires. For instance, Patla et al used oriented attachment to synthesize ultra-narrow PbS nanowires (d≈2nm)[44], [45]. The nanowires were formed through the spontaneous attachment of PbS nanoclusters using a trioctylamine (TOA) solvent that enables the 1D growth. Similarly, Murray and co-workers showed that the oriented attachment of the crystalline equivalent lead selenide (PbSe) QDs leads to the formation of various nanostructures (nanowires, -rings)[46], [47]. Their growth method was directly inspired from the synthesis of quantum dots which they tweaked by changing the

concentration of oleic acid and the reaction temperature. They suggested that oriented attachment during the nanowire synthesis might not only be due to favourable energetic rearrangements along the crystal surfaces but also to dipole-dipole interactions between the nanocrystals.

A 10μm long nanowire would require the assembly of more than 10^3 nanocrystals along the same growth axis, which might seem counterintuitive considering that the nanocrystal has several energy-equivalent facets. The difference in electronegativity between the Pb cations and the S anions make the Pb-terminated and S-terminated {111} surfaces polar whereas the faces terminated by both S and Pb ({100} and {110}) are non-polar[48]. The easiest way to maintain stoichiometric balance in the crystal is to have 4 of the {111} surfaces that are Pb terminated and the 4 other facets S-terminated. According to the different arrangements of the surfaces, the nanocrystals can have central symmetry and therefore a net dipole moment of zero or lack of symmetry and a dipole moment along the <100>, <110> and <111> axis. Assuming a random distribution of the {111} faces, the crystals have a probability of 89% to have a dipole moment with the strongest probability along the <100> and <110> axis[46]. Nanocrystals with a dipole moment aligned along these directions have the highest probability of assembling and merging, which in turns induces an avalanche effect that increases the dipole moment along the growth direction and triggers nanowire growth. As a consequence, the nanowire possesses a strong dipole moment, which can be used during device fabrication for deposition and alignment via electrophoresis[47].

Other techniques have been reported to control the growth of nanowires in solution. Among them, is the solution-liquid-solid growth (SLS), which is an analogue to the common vapour-liquid-solid (VLS) growth process, but carried out in the liquid phase[49], [50]. SLS uses metallic nanoparticles as seed catalysts but the growth precursors are brought to the seeds in solution phase rather than in the gas phase[51]. The prime advantage of this method is that the nanowire diameter can be controlled by

the size of the starting catalyst nanoparticle. PbSe and PbS nanowires have thus been made using gold and gold bismuth nanoparticles as the growth seeds[52], [53]

2.4 Device applications of colloidal nanostructures

2.4.1 Field Effect Transistors

2.4.1.1 Basics of Field-effect Transistors

Transistors are voltage-controlled devices whose conductance can be modulated upon the application of a gate voltage. From a logic point of view, they are electrical switches that can be turned ON or OFF depending on the value of the gate voltage.

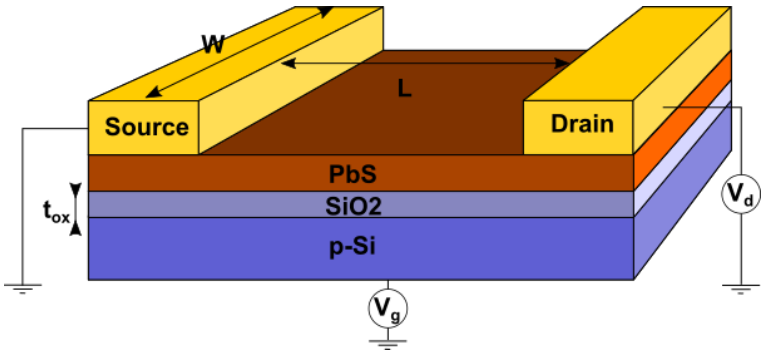

Figure 2.5. The architecture of a generic backgated PbS FET. The heavily doped p-type polycrystalline silicon is separated from the semiconducting PbS by a SiO_2 layer of thickness t_{ox}, forming a MOS capacitor

The most common FET architecture is the metal-oxide-semiconductor (MOS) configuration, where an applied voltage on the metal contact modulates the carrier concentration at the oxide-semiconductor interface. Different regimes exist depending on the nature of the charge carrier at the interface. When the concentration of majority carrier increases (decreases) the transistor is said to be in accumulation (depletion), when the minority carrier concentration becomes dominant the transistor switches to inversion regime. In typical MOSFETs, the source and drain contacts are heavily doped regions that are electrically connected in inversion regime, where a minority carrier conducting channel

links the electrical contacts. The nature of the carriers injected into the channel depend on the nature of the doping in the source and drain regions. However, this configuration is somewhat difficult to achieve in thin-film electronics because of the technical challenge of creating heavily doped source and drain regions on thin substrates.

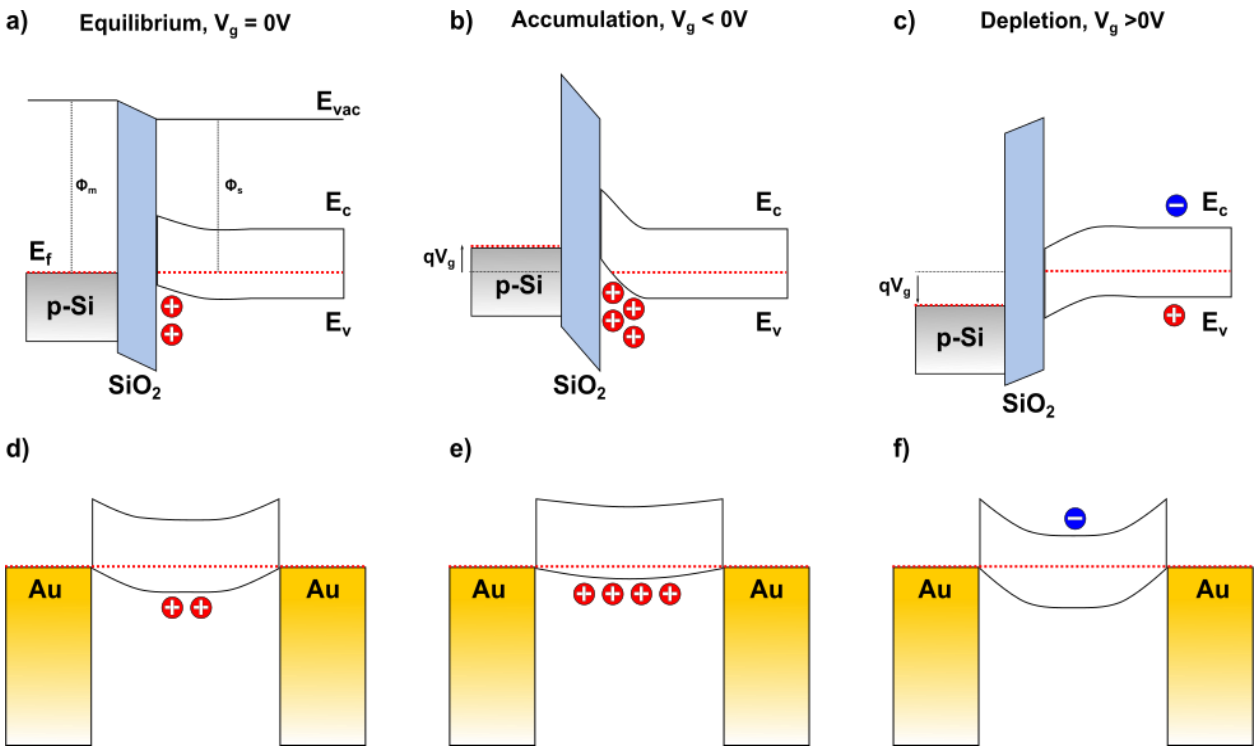

Figure 2.6. Working principle of a back-gated p-type FET.

Back-gated FETs or Schottky barrier FETs with metallic source and drains contacts have been heavily developed since the advent of carbon nanotubes FETs[54] and have established themselves as the most common way to investigate the transport properties of emerging materials. The three-terminal architecture (Figure 2.5) consists of a heavily p-doped Silicon region, which plays the role of the gate over which a thin layer of silicon dioxide (SiO_2) has been thermally evaporated. Next, either the metal contacts or the active material are deposited, depending upon the configuration (bottom contacts or top contacts). This design is much simpler than that of MOSFETs and, as a result, back-gated FETs are easier and faster to fabricate. The working principle differs slightly from their

MOSFET counterparts because the metallic nature of the source-drain contacts allows both type of carrier to be injected into the channel. Back-gated transistors do not require an inversion of the carrier concentration to start conduction, but instead function by increasing the majority carrier concentration and therefore the channel conductivity.

Figure 2.6 shows the different modes of operation of a p-type back-gated FET. In equilibrium, no voltage is applied on the gate and the Fermi levels of the metallic gate (heavily doped p-Si) and the semiconductor are aligned. In a non-ideal case, the difference in the metal workfunction ϕ_M and the semiconductor workfunction ϕ_S creates a built-in potential at the oxide-semiconductor interface, which induces a slight upward (downward) bending of the bands if $\phi_M > \phi_S$ ($\phi_M < \phi_S$) (Figure 2.6a). For a p-type semiconductor, holes are intrinsically present in the channel, and the transistor is conducting when a voltage is applied between the metal contacts (normally ON, Figure 2.6d). When a negative voltage is applied to the gate (Figure 2.6b), the Fermi level in the metal moves up and the bands at the oxide-semiconductor interface are shifted further upwards. Holes are attracted to the surface and the majority carrier concentration increases. The transistor is in accumulation mode and the conductivity in the channel increases (Figure 2.6e). When a positive voltage is applied (Figure 2.6c), the bands shifts downwards and the majority carriers move away from the surface; the transistor is in the depletion mode and the majority carrier concentration decreases. Consequently, the conductivity decreases, and the transistor is turned off (Figure 2.6f). When applying a larger positive voltage, the conduction band bends down to the quasi-Fermi level and the minority carriers are attracted to the channel. The transistor is in inversion mode and n-type conductivity is observed. However, the inversion mode is difficult to achieve in back-gated transistors because the minority carriers tend to be trapped at surface sites and defects, which inhibits the minority current.

2.4.1.2 Figures of merit

At the research level, back-gated FETs are the perfect tool to probe the transport characteristics of new materials and several useful figures-of-merits can be extracted. The three observable parameters in FET characterisation are: the drain current I_{ds}, measured between the source and drain electrodes, the drain bias, V_{ds}, and the applied gate bias, V_g. Therefore, relevant figures-of-merits should be expressed as a function of these parameters. In practice, a complete DC characterization of an FET comes down to the measurement of the transfer characteristic $I_{ds}(V_g)\big|_{V_{ds}}$ and the output characteristic $I_{ds}(V_{ds})|_{V_g}$.

Field Effect Mobility

The field effect mobility of a semiconductor describes the ability of the charge carriers to move under an electric field. The higher the mobility, the faster the carriers migrate into the channel and therefore the faster the devices can operate. In the linear regime, i.e. for a small V_{ds}, the ON current in the transistor can be expressed as

$$g_m = \frac{\partial I_{ds}}{\partial V_g} = \mu \frac{C V_{ds}}{L^2}, \tag{2.7}$$

where, g_m is the transconductance of the device, C is the oxide capacitance and L is the channel length (Figure 2.5). According to Equation 2.7 the linear mobility can be directly retrieved from the linear part of the slope of the transfer characteristics.

Current modulation

Current modulation simply relates the ratio between the current level in the transistor ON state to the current level in the OFF state. A high ON-OFF ratio is necessary in logical circuits and display applications since it allows to clearly separate the ON and OFF states of the devices and achieve a high signal to noise ratio. Furthermore, a low OFF current diminishes the current leakage when the device

is turned off which in turn minimises the power consumption and degradation due to aging. Typically, digital electronics require an ON-OFF ratio of at least 10^3[55].

Threshold voltage

The threshold voltage is the voltage at which the transistor switches on. It is directly related to the intrinsic doping of the semiconductor and thus is a perfect tool to probe the carrier concentration. An expression of the threshold voltage is given by[56]

$$V_{th} = \pm \frac{qn_o d}{C_{ox}} + V_{fb}, \tag{2.8}$$

where n_0 is the concentration of free carriers, C_{ox} the oxide capacitance, d the semiconductor thickness, and $V_{fb} = q(\phi_m - \phi_S)$ the flat band potential (assuming no fixed charges in the oxide). The flat band potential is the potential required to achieve flat band conditions across the metal-oxide-semiconductor junction with no bending of the bands at the interfaces. In this work, V_{th} was experimentally obtained as the intersection of the linear part of the transfer curve and the *x*-axis.

Subthreshold swing

The subthreshold swing, S, corresponds to the change in gate voltage required to induce a tenfold increase in the drain current[20]. It is directly obtained from the inverse of the subthreshold slope, i.e. the linear slope of the log of the transfer curve. This is expressed as

$$S = \ln(10)\frac{dV_G}{d\ln(I_{ds})} = \ln(10)\frac{k_B T}{q}\left(\frac{C_{ox} + C_S + C_T}{C_{ox}}\right), \tag{2.9}$$

where C_S and C_T are, respectively, the capacitance of the channel and the capacitance induced by trapped charges at the oxide-semiconductor interface. The lower the subthreshold swing, the sharper the transition from the ON to OFF state will be and the more efficient the device will be.

2.4.1.3 Charge transport in PbS QDs

Ligand Exchange

During QD synthesis, ligands are introduced to hold the QD together and to prevent them from aggregating, ensuring solution processability[57]. These ligands are typically long organic molecules (8-18 carbon chains) that coat the surfaces of the QDs (Figure 2.4c). However, this comes as a disadvantage for devices as QDs encapsulated with such ligands present no electrical conductivity; the long ligands prevent the charge from tunnelling from one QD to another (hopping). Moreover, the high energy barriers surrounding the QDs, while being good for quantum confinement, generally mean that the charges inside the QDs have little probability of exiting the nanoparticle, thus impeding electrical transport.

Strategies have been sought to replace these ligands with shorter, more energetically favourable ones. These new ligands serve the dual purpose of bringing the QDs closer together by reducing the inter-particle distance and modifying the electronic structure of the nanoparticles. A main requirement of the replacement ligands is that, while being short enough to ensure the transit of electrons via tunnelling, they must prevent the sintering of the QDs leading to the loss of quantum confinement.

Chemical exchange methods have been used with both organic (thiols, acids and amines)[58]–[60] and inorganic (thiocyanates[61], metal chalcogenide complexes[62], halides [63]) ligands, providing several strategies for optimizing the transport of charges through the QD films.

Ligand exchange is the key step to ensure conductivity in the QD films. It can occur in two forms: solid-state ligand exchange, where the ligands are exchanged after deposition of the QD film on a substrate[28] and liquid-state ligand exchange, where the ligands are exchanged in solution, prior to deposition[27]. While easier to implement, solid-state ligand exchange usually is accompanied by cracking of the QD film, because of the loss of volume occurring when the QDs confined to a small volume. These cracks can, in turn, impede the conductivity of the films.

Doping and passivation

Unlike bulk semiconductors, QDs and nanowires have a high surface-to-volume ratio and alterations at their surface can significantly affect the overall electronic structure of the particle. Since the ligands bind directly at the QD surface, they can modify their properties thus opening the way to QD functionalization via surface chemistry. Both the chemistry of the binding group and the ligand dipole moment affect the strength of the QD-ligand surface dipole and result in a shift of the vacuum energy level, which in turn shifts the valence and conduction band levels. In the case of, Brown *et al* have shown that using various ligands ranging from halides to thiols the energy shift could span as much as 0.9eV due to various dipole interactions[29]. Ligands based on halides groups [tetrabutylammonium iodide (TBAI), bromide (TBABr), chloride (TBACl), and fluoride (TBAF)] showed a deep shift downwards of the energy levels resulting in n-type doping, whereas the thiols and amine-based ligands [1,2-ethanedithiol (EDT), 3-mercaptopropionic acid (MPA), 1,2-ethylenediamine (EDA) ammonium thiocyanate (SCN)…] had shallower band shifts resulting in intrinsic or p-type doping. These collective findings show that, on top of the tunability of the bandgap via size modification, post synthesis chemistry adds another degree of tunability paves the way to band alignment engineering, a particularly effective strategy for improving the efficiency of PbS QDs solar cells[13].

Surface changes such as modification of the Pb:S stoichiometry, structural defects at the surface or dangling bonds or incomplete ligand exchange often induce the formation of trap states[64], i.e. localized energy states in the bandgap that trap the free charges and promotes recombination, both effects are detrimental to device performance. However, ligands can also act as passivation materials to reduce the density of traps within the QDs by selectively passivating the trap states[10]. For instance, several studies have shown that inorganic ligands based on halides can help to passivate surface defects and improve electronic transport[13], [65].

In a similar way, unwanted atoms or molecules that adsorb at the QD surface will also impact the electronic structure. For instance, oxygen easily adsorbs at the surface of lead chalcogenide QD and behaves as an acceptor resulting in p-doping of the QDs and oxidation of the QDs as well as degradation of device performance with time. This has motivated research to steer away from air sensitive organic ligands and Sargent's group has shown that halides that attach to the QD surface can effectively act as an oxygen blocking layer, resulting in air-stable QDs[65], [66].

PbS QD FETs

The progress in ligand exchange strategies has led to a dramatic improvement in charge transport in QDs films and has enabled mobility-based devices such as FETs. Traditionally, cadmium-based QDs have shown better performances, achieving high mobilities of 10-30 $cm^2.V^{-1}.s^{-1}$[67]–[71] with champion devices reaching near-crystalline mobilities[72]. However, the best performing devices often relied on annealing temperatures above 200ºC, resulting in a loss of quantum confinement due to sintering, a disadvantage for light-related applications (phototransistors, light emitting transistors…). As for lead chalcogenides, PbSe QDs FETs have been widely studied and mobilities have been found to be in the range of 0.1-1 $cm^2.V^{-1}.s^{-1}$ range[59], [73]–[75] with the best devices reaching values as high as 10 $cm^2.V^{-1}.s^{-1}$ using stoichiometric control and thiocyanate ligands[76]. Interestingly, progress in the formation of QD superlattices via controlled solvent evaporation and a better understanding of the oriented attachment process, have led to a novel approach in the fabrication of QD devices, parting from the conventional layer by layer spin deposition method. For example, a recent study by Balazs *et al* has reported high field effect mobilities in superlattice PbSe devices of 24 $cm^2.V^{-1}.s^{-1}$[77].

FETs consisting of PbS QDs have somewhat lagged behind in terms of development, but the breakthroughs in PbS QDs solar cell research[13], [78] still provide a strong motivation for the investigation of PbS nanomaterial FETs, with the hope that an improved understanding of the charge transport will lead to better solar cell efficiencies. Towards this end, Kagan's group have applied their

findings for PbSe QDs to PbS QDs and have shown that careful control of the stoichiometry via the ligand exchange process (sodium sulphide Na_2S) and liquid phase lead chloride ($PbCl_2$) treatment has resulted in mobilities of 0.5 $cm^2.V^{-1}.s^{-1}$[79]. The 10-fold increase in performance of PbSe over PbS is attributed to the stronger electronic coupling of the PbSe QDs and the lower density of traps[58]. FETs were initially made using organic thiol ligands (mobility 10^{-3} $cm^2.V^{-1}.s^{-1}$[58], [80], [81]) but air-stability issues limited their potential in FETs application. Halides (ligands terminated with halogen ions: iodide I^-, chloride Cl^-, bromide Br^- …) were also used with the purpose of achieving air stability and enhanced trap passivation (ex: tetrabutylammonium iodide, TBAI, mobility 0.1 $cm^2.V^{-1}.s^{-1}$[82]).

Halide ligand exchange promotes n-type doping, thus halides are the ligand of choice when it comes to the use of n-type PbS QDs in devices[83]. Besides optimizing carrier mobility and ambient stability, research has also focused on controlling the polarity of the majority carriers in the channel, i.e. using ligands and encapsulation techniques to achieve p-type, ambipolar and n-type transport in QD films. Thiocyanate (SCN) ligand exchange was reported to produce ambipolar QD films with both hole and electron mobilities approaching 0.5 $cm^2.V^{-1}.s^{-1}$[84], [85]. Alternatively, Bisri *et al* used ion-gel gating to improve the filling of the carrier traps which, combined with organic ligand (3-mercaptoprepionic acid, MPA), produced ambipolar FETs with high electrons and hole mobilities (1.9 $cm^2.V^{-1}.s^{-1}$ for electrons and 0.15 $cm^2.V^{-1}.s^{-1}$ for holes, measured in air-free conditions)[81]. Air exposure is a major contributor in doping as oxygen behaves as an electron acceptor, suppressing electron current and effectively p-doping the channel[86], [87]. No reliable ligand exchange strategy has been reported to selectively p-dope the QDs as the p-doping often reported with organic ligands relies on air exposure and partial oxidation of the QDs. The lack of true, well passivated p-type PbS QDs limits their integration in more complex designs such as CMOS inverters. Therefore, hybrid devices with well-known p-type nanomaterials such as carbon nanotubes have also been investigated[88].

2.4.1.4 Lead chalcogenide NW FETs

Due to the similarity in the synthesis procedure (see section 2.3.3), colloidal nanowires FETs have also been developed in parallel with the development of QD FETs. The main advantage of colloidal nanowires over their QD counterparts lies in the fact that improved transport performances can be expected because of their highly crystalline nature. Furthermore, since NW FETs are made of NWs (multiple or single) bridging over two contact electrodes, ligand exchange is not required to achieve electrical conductivity. Therefore, colloidal NW FETs are the perfect tool to probe the various interface interactions in colloidal FETs (channel/dielectric; channel metal contacts; channel/air…) without being hindered by low device performances/sensitive fabrication techniques[89]. During the nanowire growth, a trade-off must be established between nanowire length and diameter as longer reaction times will tend to yield longer but thicker nanowires. To achieve sufficiently long nanowires for device fabrication (length $\geq$ 10μm), the nanowire diameter needs to be 20-50nm. It should be mentioned that at such diameters, low to weak quantum confinement is expected in PbS and PbSe despite their large bohr radii (18nm and 46nm for PbS and PbSe, respectively). In the end, the nanowire approach is similar to that of sintered CdSe QDs, which has so far produced the best performance FETs[68], [69].

The first lead chalcogenide colloidal NWs were reported in 2007 with the synthesis of PbSe NWs by Murray *et al*[46], [47]. Extensive studies on PbSe nanowires were made by the Kagan's group, which most notably showed the ability to tune the nanowire polarity from n-type to p-type using hydrazine (N_2H_4) and controlled oxygen exposure[89]. They also studied the influence of the dielectric and reported that a gate dielectric stack made of self-assembled monolayer (octadecylphosphonic acid (ODPA)) on aluminium oxide (Al_2O_3) resulted in low hysteresis on flexible substrates[90]. In the same study, they introduced polymer encapsulation of the nanowire using poly(methyl methacrylate) (PMMA), which effectively acts as an oxygen blocking layer allowing for the nanowire to maintain its

n-type conduction in air. This ultimately led to the realization of nanowire p-n junction with the n-side of the junction covered in PMMA and the p-side exposed to air[91]. Throughout these studies, field effect mobilities remained in the 10-50 $cm^2.V^{-1}.s^{-1}$ range, confirming the better transport performance of nanowires over PbSe QDs. (see Section 2.4.1.3).

Several groups have demonstrated the synthesis of PbS nanowires following a similar oriented attachment method but the analysis of their electrical properties somehow falls behind [92]–[94]. Jang *et al* led an interesting study where they compare the electrical performance of PbS NWs grown via three different synthesis methods, namely oriented attachment, chemical vapour deposition (CVD) and gas phase substitution[92]. They reported that the PbS nanowires exhibited p-type condcutivity and that CVD nanowires had the highest hole mobility of about 10 $cm^2.V^{-1}.s^{-1}$, whereas that of oriented attachment grown was only of 0.1$cm^2.V^{-1}.s^{-1}$. In our work, we extensively studied the electrical response of p-type PbS nanowires grown via oriented attachment and obtained high hole mobilities averaging over 30$cm^2.V^{-1}.s^{-1}$[95]. These performances are in-line with that obtained by the Kagan's group with PbSe NWs.

2.4.2 Photodetectors

2.4.2.1 Fundamentals of photodetectors

Photoconductors

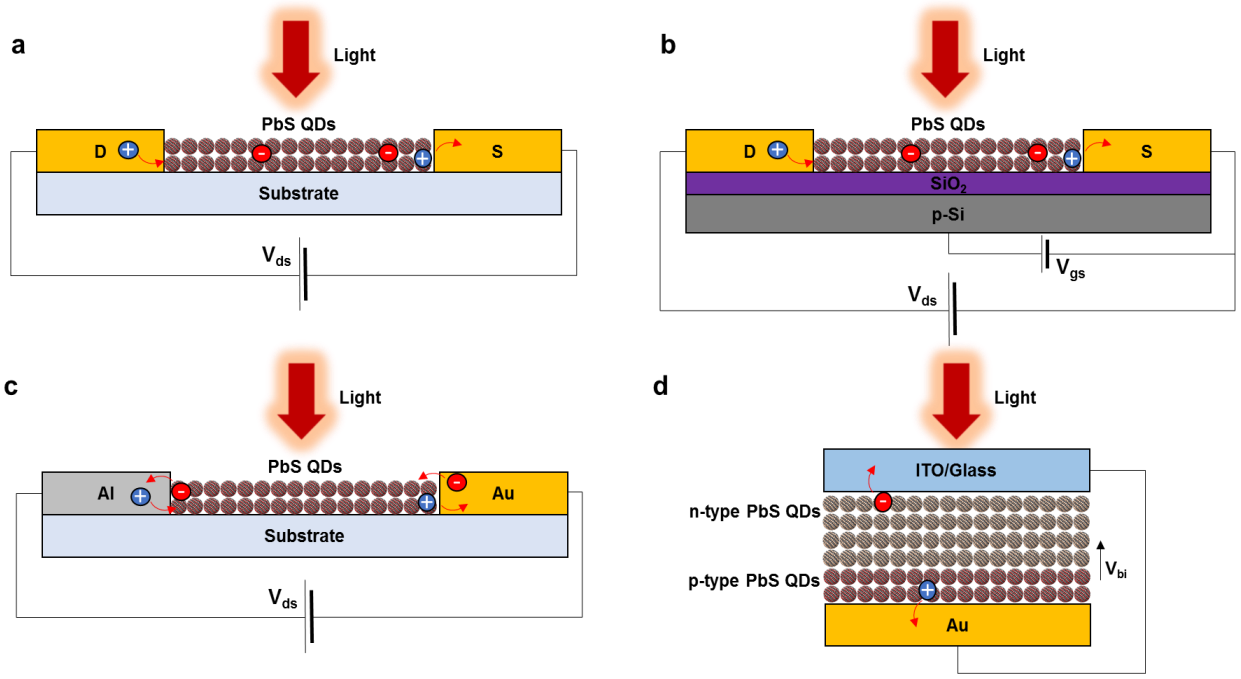

Figure 2.7. Device types of PbS photodetectors. a) Basic two terminal photoconductor. b) bottom-gated phototransistor. c) Schottky photodiode with aluminium and gold contacts. d) Vertical p-n junction photodiode (solar cell).

Photoconductors are two terminal devices made of a photoactive semiconductor material connected to two metal electrodes via ohmic contacts as shown in Figure 2.7a. Photoconductors rely on a change of conductivity when illuminated. Upon light excitation, photons are absorbed by the semiconductor and generate electron-pairs which modify the carrier density and increase the electrical conductivity[96]. A basic expression of the semiconductor conductivity is $\sigma = q(n\mu_n + p\mu_p)$ and any increase in the carrier concentration will increase the conductivity[20]. If the absorption of a single photon can recirculate charges several times into the circuit before recombination, then photoconductive gain is created. In the schematic shown in Figure 2.7a, electron-hole pairs are created upon photon absorption. Under the action of a bias voltage, positive charges (holes) are extracted into

the circuit via the cathode (S) and reinjected via the anode (D) creating one cycle. To achieve high gain G, carriers with long lifetimes (long recombination time) τ_{lt} and fast transit times τ_{tt} are required. Whenever $\tau_{lt} > \tau_{tt}$, $G > 1$ is achieved. The presence of charge trapping states, called recombination or sensitizing centres, inside the material will help to achieve high gain, since as long a charge is trapped in the channel it does not recombine with the opposite charge, which can circulate in the circuit many times. For instance, in Figure 2.7a, as long as the trapped electrons do not recombine with the circulating holes, gain is created.

Phototransistors

Phototransistors are effectively three terminal photoconductors with the addition of a gate terminal (Figure 2.7b). The purpose of the gate voltage is to modulate the channel carrier concentration via an electric field effect. This changes the concentration of majority and minority carriers in the channel, which can help optimize the photoconductor performance. For instance, for a p-type semiconductor applying a negative gate voltage will induce supplementary holes into the channel and increase the photoconductivity and gain. The gate voltage also controls the position of the Fermi level and can be used to populate or depopulate the trap states. States close to the valence (conduction) band will be filled on the application of a negative (positive) gate bias. Artificial filling of the sensitizing centres can therefore be used to increase the lifetime of the carriers τ_{tt}. It is important to note that in such scenarios, the long lifetime trapping of the carriers will screen out the applied gate electric field, which results in a shift of the Fermi level within the semiconductor. Experimentally this is observed by a shift of the threshold voltage upon light illumination[97].

Photodiodes

Unlike photoconductors, photodiodes rely on the presence on an internal built-in electric field across the semiconductor to extract the photogenerated charges (photovoltaic effect). There are two major types of photodiodes differing by how the built-in potential is created. Schottky photodiodes

(Figure 2.7c) are metal 1-semiconductor -metal 2 (M1-SC-M2) architectures where the difference in the work function of the two metals $\Phi_{M1} - \Phi_{M2}$ creates a bending of the energy vacuum level across the semiconductor thus creating a built-in electric field. Careful choice of the metal/semiconductor interface should aim to establish ohmic contact on one side of the junction and Schottky contact on the other side. The Schottky barrier at the semiconductor/metal Schottky contact results in rectifying characteristics when the diode is biased. Note that unlike the device presented in Figure 2.7c, Schottky diodes typically have a vertical architecture to maximise the electric field across the junction, however the presented design is similar to what will be discussed in Chapter 6.

Junction photodiodes and particularly p-n junction photo diode use the potential that builds up when a p-type and n-type semiconductor are brought in contact[20]. The device presented in Figure 2.7d shows a classic vertical p-n architecture commonly found in QD solar cell technologies. The p-n interface creates a depletion region in which photogenerated charges are broken away by the built-in potential and separated electrons (holes) are drawn towards the cathode (anode). There are usually hole and electron buffer layers inserted in between the semiconductor and the electrodes to facilitate charge extraction[13]. In photodiodes, since both electrons and holes are extracted on the circuit, one absorbed photon can only contribute to the circulation of one carrier and the gain cannot exceed unity. On the other hand, since the response time of the photodiodes rely only on the carrier transit time instead of recombination time, they tend to have a faster response than photoconductors.

2.4.2.2 Figures of merit

The large variety of photodetectors, as well as the many sensing applications they are used in, has rendered it necessary to use figure-of-merit to evaluate their performances. The consensus, however, is that photoconductors will be used whenever high gain is needed (optical amplifiers) and photodiodes when fast response times are required.

Quantum efficiency, Responsivity and Gain

The external quantum efficiency η is the most intuitive figure-of-merit which describes how many carriers are converted into current per incident photon

$$\eta = \frac{I_{phot}}{q\phi} = \frac{I_{phot}}{q}\left(\frac{h\nu}{P_{in}}\right), \tag{2.10}$$

where I_{phot} is the photocurrent generated in the photodetector, $\phi = P_{in}/(h\nu)$ is the photon flux, ν is the frequency of the incident light, q the electron charge and P_{in} is the incident power. The responsivity of a photodetector, R (in A/W), is simply the ratio of I_{phot} to the optical power

$$R = \frac{I_{phot}}{P_{in}} = \eta\,\frac{q}{h\nu}. \tag{2.11}$$

Both η and R are dependent on the wavelength of the incident light, since the absorption of light by a semiconductor is not uniform across the spectrum. At a fixed wavelength and incident power, they are however, straightforward to measure experimentally since only the photocurrent is needed. The photoconductive gain G is related to the responsivity and the quantum efficiency by

$$G = \frac{R}{\eta}\frac{h\nu}{q} = \frac{\tau_{lt}}{\tau_{tt}}. \tag{2.12}$$

Noise and Detectivity

The signal-to-noise ratio (SNR) is given by

$$SNR = \frac{RP_{in}}{i_n} = \frac{I_{phot}}{i_n}, \tag{2.13}$$

where i_n is the noise current. The noise current can arise from different parameters such as thermal noise i_{th}, shot noise i_{sh}, 1/f noise [11], [98]. The root mean square values of the shot noise and thermal noise are defined, respectively, by $i_{sh} = \sqrt{2qBI_d}$, and $i_{th} = \sqrt{4kBT/R}$, where B is the noise

bandwidth, I_d is the dark current, k the Boltzmann constant and T the temperature. The noise equivalent power (NEP) is defined as the power at which the SNR is unity and defines the minimum detectable power by the photodetector (in $W.Hz^{-1/2}$)

$$NEP = \frac{i_n}{R}. \tag{2.14}$$

However, the NEP is specific to the surface area of the detector and researchers tend to use the normalized detectivity D^*, which is independent of the device area. D^* describes the SNR with a detection bandwidth of 1Hz, a device area of 1 cm^2 for an incident power of 1W and is expressed in $cm.Hz^{1/2}W^{-1}$ or Jones[99]

$$D^* = \frac{R}{i_n}\sqrt{AB}, \tag{2.15}$$

where A is the surface area of the detector. The shot noise is often considered to dominate the noise current and leads to an expression of D^* that is independent of the electrical bandwidth, B ($D^* = R\sqrt{A/(2qI_d)}$)[100], [101]. However, other noise sources have been reported to dominate in colloidal photodetectors[102] and in this case the shot noise approximation then leads to an overestimation of the detectivity.

Temporal Response

For a photodetector excited with a modulated light source of frequency, f, the photocurrent decreases when the time required to recover from the current under light I_{light} to I_{dark} is longer than the time $1/(2f)$. The cut-off frequency, f_c, is defined as the frequency at which the DC photocurrent value decreases by a factor of $\sqrt{2}$ [11]. For systems with an exponential temporal response, the time constant of the device, τ, is related to the cutoff frequency f_c via the relation $\tau = \frac{1}{2\pi f_c}$. However, τ only describes the time at which I_{light} has reached ≈63% of its final value and therefore the rising

time τ_r and falling time τ_f offer a better representation of the detector speed. They correspond to the time necessary for the light current to either rise from 10% to 90% (τ_r) or to fall from 90% to 10% (τ_f) of its final steady-state value. The rising and falling times might be different, notably when traps states interfere with carrier recombination, in which case the response time of the longest edge (rising or falling) determines the bandwidth. The response time is linked to the rising (falling) time by the relation $\tau_i = 2.2\tau$ (where $i \in [r, f]$ represents the longest edge). Therefore, one can obtain the band-width of the photodetector from the rising and falling times using

$$f_c = \frac{1}{2\pi\tau} \approx \frac{0.35}{\tau_i}. \tag{2.16}$$

2.4.2.3 Recent advances in PbS photodetectors

Based on the figures-of-merits that have been introduced, we can now present a brief review of the progress made in colloidal PbS photodetectors technologies. The performances of the devices presented are summarized in Table 2-2

Photoconductors

High photoconductive gain in photoconductors requires both long carrier lifetimes τ_{lt} and short transit times τ_{tt} (Equation 2.12). As discussed in Section 2.4.2.1, increasing the carrier lifetime, or photosensitization, is directly linked with the presence of states within the bandgap that traps one type of carrier whilst allowing the other type of carrier to circulate. However, long carrier lifetimes limit the response time of the device leading to a fundamental gain-bandwidth trade-off in photoconductors: for example, high gain devices tend to have cut-off frequencies below 100 Hz.

The carrier transit time is related to the carrier mobility via the relation $\tau_{tt} = \frac{L^2}{\mu V}$, where μ is the mobility of the circulating carriers, L the electrode spacing and V is the applied bias. Therefore, the

faster the mobility, the shorter the transit time. Since ligand exchange impacts both the density of trap states and the mobility of the QDs, exchange strategies discussed in Section 2.4.1.3 are the main way to improve the performances of PbS QDs photodetectors. Early PbS QDs photoconductors were based on butylamine ligands, which showed high gain and detectivity in both the SWIR[103] and visible range[104] that outperformed the state-of the art epitaxially grown devices. To increase the photodetector bandwidth, the same group carried out an extensive trap analysis to increase the detector bandwidth and showed that EDT treatment of the QDs lead to the creation of a single shallow trap with a short recombination time of 30 ms, ideal for imaging applications[105], [106]. These excellent device performances were, however, achieved in air-free conditions, which are impractical for real commercial applications. Later studies showed that inorganic passivation using arsenic sulfide (As_2S_3) [107] or sulfide (with an alumina passivation layer)[108] resulted in high performing devices in ambient conditions. Recently, a study using an halide passivating ion (cetyltrimethylammonium bromide (CTAB)) produced a device with high gain, 100kHz bandwidth and air stability[109].

To overcome the gain-bandwidth trade off, hybrid structures based on fullerene/PbS have also been investigated. The principal idea in this case is to sacrifice some of the gain by extracting the trapped charges (electrons) into the polymer as a result of favourable band alignment. In turn, this reduces the carrier lifetime allowing bandwidths as high as 330 kHz to be obtained [110], [111]. Silver nanoparticles were also blended with QD films, which donate electrons to the system by filling the trap states near the valence band. This n-type doping resulted in lower dark currents and faster response times enhancing both the gain and time response of the photoconductor[112]. Following this hybrid approach, Ren *et al* reported the use of bilayer devices made of EDT and TBAI-treated PbS layers[113]. The energy difference between the layers promoted the extraction of electrons into the TBAI layer and holes into the EDT layer, which resulted in enhanced response time without compromising the gain.

Phototransistors

In parallel to two terminal photoconductors, gate dependant photoconductivity was also investigated. The primary advantage of this configuration is to use the gate modulation to investigate the nature of the states within the bandgap. Nagpal and Klimov showed, for instance, the existence of mid-gap states that form a conductive band contributing to dark current when partially filled[114].

However, in term of device performances, the most striking results were obtained with hybrid PbS QDs/2D materials (graphene, molybdenum disulphide (MoS_2)) phototransistors. In this case, the underlying idea is to use the high mobility of the 2D materials[115] to achieve fast transit times for the circulating charges. Under the action of a built-in potential appearing at the PbS/2D interface, photo-charges (holes) from the QD layer are transferred to the 2D material, while opposite charges (electrons) remain trapped in the QD layer. The first hybrid phototransistor was introduced by Konstantatos and used EDT-treated PbS QDs and graphene as a transport layer and demonstrated outstanding gain and detectivity[15]. Instead of graphene, Kufer *et al* resorted to the 2D semiconductor, MoS_2, to bypass the high dark conductivity of graphene and to benefit from the p-n junction occurring at the MoS_2/PbS interface[14]. This approach was recently further investigated by our group using bi-layer TBAI/EDT QDs to enhance the built-in electric field necessary to extract electrons in to the MoS_2 layer [116].

The strategy of increasing transit time to obtain high gain is, however, limited by the fact that high mobility materials also exhibit large dark currents, which means low SNR. A novel device design was presented recently by Adinolfi called photojunction FET, which used a rectifying molybdenum oxide (MoO_3)/PbS junction to fully deplete the channel in dark conditions, so that only photogenerated charges contributed to the current, resulting in high gain and low dark current[117].

Photodiodes

Contrary to photoconductors, photodiodes exhibit high speeds at the price of low gain. Both photogenerated charges are extracted thanks to the built-in electric field and fast transit times can be

achieved provided that the distance travelled by the extracted charges before collection is shorter than their diffusion lengths. PbS QD photodiodes (and solar cells) benefit from the long diffusion length of PbS QDs (80nm[118]) meaning that reasonably thick layers can be used, which increases light absorption without damaging the charge collection efficiency.

In 2009, Clifford *et al* presented a seminal PbS Schottky photodiode using BDT-treated PbS QDs and Al/Indium Tin Oxide (ITO) as electrodes[119]. By decreasing the thickness of the photodiode, they created fully depleted junctions which resorted only on drift current to extract the charges resulting in a large bandwidth (3 MHz, Table 2-1). Other Schottky diodes have since then been reported, using either a different metal/PbS barrier [120], [121] or introducing novel fabrication techniques (doctor blading) [122]. If p-n junction photodiodes based on PbS QDs have extensively been used in solar cell technology [78], [123], [124], these works have not necessarily reported on the classical photodetectors figures-of-merits. Pal fabricated a p-n junction architecture with respectively PbS as the p-type and ZnO as the n-type material[125]. Concurrently, a heterojunction based on ZnO/TBAI PbS/EDT PbS was fabricated by Qiao et al which used lead iodide (PbI2) as an passivation layer between ZnO and the PbS QDs[126]. Finally, Dong et al used a blend of PbS QDs and ZnO QDs dispersed in a polymer matrix in which the QDs were used as photoactive material and the polymer matrix facilitated charge extraction[127]. They showed that ZnO QDs acts as sensitizing centres under illumination which allows to create gain and turned the device into a hybrid photodiode in the dark and photoconductor under illumination.

Device type	Ligand	Responsivity (A/W)	Detectivity (Jones)	Temporal Response	Year	Ref
Photoconductor	Butylamine	2700	1.8×10^{13}	18 Hz	2006	[103]
Photoconductor	Butylamine	113	5×10^{12}	8 Hz	2007	[104]
Photoconductor	EDT	10	1.2×10^{12}	25 ms	2008	[105]
Photoconductor	As_2S_3	200	1.2×10^{13}	-	2014	[107]
Photoconductor	S^{2-}	50	3.4×10^{8}	40 Hz	2014	[108]
Photoconductor	CTAB	7.5×10^{3}	-	40 μs	2015	[109]
Photoconductor	Butylamine	η = 57%	4.4×10^{7}	330 kHz	2010	[111]
Photoconductor	Butanedithiol	5	2.5×10^{11}	200 Hz	2015	[112]
Photoconductor	TBAI/EDT	250	1.7×10^{11}	29 ms	2017	[100]
Phototransistor	EDT	10^{7}	7×10^{13}	10Hz	2012	[15]
Phototransistor	EDT	6.5×10^{5}	5×10^{11}	-	2015	[14]
Phototransistor	TBAI/EDT	5.4×10^{4}	1×10^{11}	950 μs	2018	[116]
Phototransistor	TBAI	5	$\approx 2.5 \times 10^{10}$	100kHz	2015	[117]
Photodiode	BDT	η = 17%	1×10^{12}	3MHz	2009	[119]
Photodiode	MPA	0.26	10^{11}	135 μs	2016	[122]
Photodiode	TBAC	0.2	10^{12}	1 MHz	2017	[121]
Photodiode	EDT	η = 17%	1.45×10^{12}	-	2012	[125]
Photodiode	TBAI/EDT	0.53	1.3×10^{13}	5.3 μs	2017	[126]
Photodiode	Butylamine	1.24	2.2×10^{11}	180 μs	2014	[127]

Table 2-2. Comparison of the performances of PbS photodetectors reported in the literature.

3 EXPERIMENTAL TECHNIQUES

3.1 Introduction

In this work two types of optoelectronic devices were used; phototransistors in Chapter 4 and 5 in which the current can be modulated under the action of both an external electric field and light stimulation, and infrared photodetectors which convert incident IR light into an electrical output (Chapters 6 and 7). The main photoactive materials were PbS nanowires and quantum dots whose synthesis were made by Dr Bo Hou and Dr John Hong and were summarized in Chapter 2. This chapter will introduce the reader to the experimental processes occurring after the QD/NW synthesis in order to achieve successful device fabrication and characterisation.

3.2 Material characterisation

3.2.1 Electron Microscopy

To allow direct imaging of the QD films and nanowires beyond the resolution of conventional optical microscopes a combination of scanning electron microscopy (SEM) and transverse electron microscopy were used throughout this work.

SEM

SEM is a conventional technique used to image the morphology of materials at sub-micrometre resolutions. It works by directing a focused beam of accelerated electrons under a high voltage (typically 2kV to 50kV) on the sample. The beam scans the sample line by line (raster scans) and the excited electrons interact with the surface atoms of the material. Two kinds of electrons are re-emitted and collected by sensors, providing information about the topography of the material. Secondary electrons are emitted by sample surface atoms as they are excited by the electron beam. Secondary electrons typically have low energy (2-5eV) and only come from atoms close to the specimen surface. As such they are sensitive to the surface topography and are the most common source of electrons

used for SEM imaging. Back scattered electrons on the other hand are high energy electrons coming from the electron beam which are reflected from the sample by elastic interactions with the specimen atoms. Elements with a higher atomic number (heavier) scatters more electrons than lighter elements and thus a contrast can be created depending on the chemical composition of the imaged atoms.

In this work we mainly used secondary electrons imaging with two SEMs, a Carl Zeiss Evo SEM for resolutions up to 1μm, and a high vacuum FEI Quanta 600 for resolutions up to 200nm. A great advantage of the SEM is that the characterization is non-invasive and can be done at any stage of the device fabrication process. The NWs and QDs samples did not need any special preparation if the surface was electrically grounded with copper tape to the metallic stage holder to avoid electrostatic charging from the electron beam. When imaging polymers such as PDMS (Chapter 7), a thin layer of gold (2nm) was sputtered on the samples to avoid charging and obtain better resolved images. As for the acceleration voltages, they were kept with 2-15kV as we found that prolonged exposure to higher energy beams damaged the samples.

TEMf

Transverse electron microscopy (TEM) is another common tool used in material science to image and characterise materials. A TEM is composed of an electron source, a set of electromagnetic lenses, and electron detector. An electron gun creates a beam of electrons accelerated at high energy (100-300kV) and thus low wavelength. The beam is then focused on the specimen with the electromagnetic lenses. If the substrate is thin enough (10-100nm) the electrons can transit through the material and the beam shape is modified via inelastic and elastic scattering with the atoms of the imaged material. This imprints an image of the material in the beam which can then be magnified through another set of lenses and detected, usually with a fluorescent screen coupled with a charge coupled device (CCD) camera system. Because of the low wavelength of the incident electrons, very high resolution can be achieved, down to the dimensions of atoms. When imaging crystals the periodic arrangement of the

atoms acts as diffraction gratings which creates constructive and destructive interferences in the transmitted beam. This property can be used with the selected area diffraction method (SAED) to determine the crystalline structure and lattice parameters by imaging the material at different angles, corresponding to different diffraction conditions. By carefully controlling the aperture of the beam, one can image and identify the crystalline arrangements in area as small as a few hundreds of nanometres. In scanning transverse electron microscopy (STEM) the beam is focused to a narrow spot size (0.2nm) and scanned across the specimen in a raster. Coupled with energy dispersive x ray spectroscopy (EDX) , which detects the x-ray radiations (specific to each element) emitted by the atoms when hit by the beam, this allows to perform an element composition mapping of the sample over a selected area (see for instance: Chapter 4, Figure 4.1). The combination of high-resolution imaging, diffraction and elemental analysis makes TEM a very powerful and ubiquitous tool in material characterisation, only limited by the low thickness to which the specimen must abide for effective imaging. In this work all the TEM imaging was performed by Dr Bo Hou. The samples to be imaged (PbS NWs, PbS QDs) were drop casted on TEM grids made of metallic grids covered by ultra-thin carbon films to be correctly imaged.

3.2.2 Atomic Force microscopy

In atomic force microscopy (AFM), imaging is done by scanning an ultra-sharp tip on a cantilever across the sample. When the tip approaches the surface of a sample, the attractive/repulsive forces between the sample the tip induce a deflection of the cantilever. The amplitude of the deflection can be measured by a laser incident on the cantilever and a photodetector. The AFM can be operated in various modes divided into contact modes and tapping modes. In contact mode the tip is scanned across the sample surface and the variation of the topography is measured. Whenever the topography of the sample changes, so does the deflection of the cantilever whose variation in amplitude can be quantified by the change in intensity at the photodiode. However, it is usually not the direct deflection

of the cantilever which is measured, but rather the intensity of the feedback signal required to keep the cantilever at a constant position. Because in contact mode, the tip is directly touching the specimen, this technique can lead to both tip and sample damage. In tapping mode, the cantilever oscillates up and down near its resonant frequency at fixed amplitude, driven by piezoelectric elements. The attractive forces interacting with the cantilever when the tip comes close to the specimen surface disrupt the amplitude of the cantilever oscillation. This change in amplitude is compensated by adjusting the height of the cantilever in order to keep a constant oscillation amplitude. Compared to contact mode, damages done to the tip and the sample are less important due to the short duration of the applied forces and the reduction of the lateral forces between the tip and the sample (drag). Tapping mode also allows to plot a phase map of the sample which shows the dephasing of the cantilever oscillations as it contacts the samples. As different materials have different stiffnesses/surface energies this will induce a contrast in dephasing as the tip scans over and thus give information regarding the sample material composition. Phase profile often offers higher resolutions than amplitude ones, as the phase contrast can be higher than the amplitude which is limited by the radius of curvature of the tip.

In this work AFM characterisation was performed using a Veeco Dimension 3100 AFM in tapping mode with silicon cantilevers and 8nm sharp tips (Brueker TESPA-V2).

3.2.3 Absorption Spectroscopy

Absorption spectroscopy gives information about the energy states of the probed samples. For semiconductors, photons with an energy greater than their bandgap radiated on the sample will be absorbed. On the contrary photons with energy lower than that of the bandgap will be transparent to the material and pass through. Thus, by measuring the photon flux transmitted thorough a sample at different energies, one can determine the absorption spectrum of the material. The onset of absorption corresponds to the lowest favourable energetic transitions from the ground state to an excited state.

For a semiconductor this usually corresponds to transitions from the valence band to the conduction band and allows to recover the bandgap of the material. In QDs a peak is observed to in the absorption spectra which corresponds to the first excitonic peak. As discussed in Chapter 2, the electron-hole pair resulting from the absorption of a photon can be bound to form an exciton. The exciton energy level is located a few meV below the conduction band which leads to below-energy-gap absorption. In bulk semiconductors excitons dissociate quite easily, but as they are tightly bound in quantum confined systems, the excitonic peak can be observed. The shape of the peak also gives an indication regarding the size dispersion of the QDs as the higher the dispersion is, the higher the energy broadening of the exciton level is and thus the broader the absorption peak will be.

In this work the absorption spectrum of PbS QDs were taken with a Cary 5000 UV-Vis spectrometer. Absorption could be measured for both colloidal and solid states samples. Colloidal samples were prepared by diluting the post-synthesis stock solutions in chloroform in transparent cuvettes adapted for UV-Vis measurements. Solid samples were prepared by spin coating or transfer printing the QDs on transparent glass substrates. Unfortunately, no successful absorption spectroscopy of the PbS NWs could be recorded as the presumed absorption onset of the PbS NWs (3μm) was too close to the apparatus limit (3.2μm) and the measured signal was too noisy at high wavelengths. Absorption measurements were carried out by Dr John Hong in the Department of Materials facility at the University of Oxford.

3.3 Device Fabrication

3.3.1 Lithography

To fabricate the FETs and the photodetectors two lithography methods were used, ultraviolet (UV) lithography also known as photolithography and electron beam lithography (EBL). Both methods rely on the sensitization of a resist by an incident beam which alters their solubility in developing solvents.

UV lithography

In UV lithography the resists are crosslinked under exposure to ultraviolet light. Two kinds of resists exist, namely positive photoresist where the areas exposed to the UV light becomes soluble in the developing solvent, and negative photoresist where the exposed areas are 'hardened' and become insoluble in the developer. The choice of a photoresist typically depends on the required resolution and the desired vertical profile of the etched resists. Positive photoresists generally offer higher resolutions but come with a 'positive' edge profile where the base of the developed area is narrower than the area at the top. This can make subsequent process steps such as metal lift off difficult to achieve. In UV lithography as the UV lamp exposes the whole surface of the wafer, the use of photomasks is required to pattern the photoresist. These masks are made of transparent materials with area covered in a dark, UV blocking material (e.g. a thin layer of chromium) corresponding to the areas of the resist to be etched away (positive photoresist) or to be kept on the substrate (negative photoresist). Here, we used a positive photoresist, Microposit S1813. The resist was spin coated on the wafers for 45s at 4000 rpm to obtain a uniform film thickness of 1.5μm. After deposition, the photoresist was soft baked at 115ºC for 1 minute to enable solvent evaporation. UV exposure was made using an EVG 620 mask aligner and a 360nm UV lamp. The optimised dose for 1.5μm SR 1813 was 45 $mJ.cm^{-2}$. After exposure the wafers were immerged for 50s in Microposit MF-319 for development which was stopped in a de-ionized water bath for 1min. For the epoxy masters used in the fabrication of patterned PDMS stamps (Chapter 7), a MicroChem SU8 2002 negative photoresist

was instead used. The viscous resist was spun in two steps, 10s at 500rpm to spread it over the wafer and 45s at 3000rpm to achieve a target thickness of 2μm. The resist was prebaked 95ºC for 60s, exposed at 60 $mJ.cm^{-2}$ and post baked at 95ºC for 180s. The post exposure bake was necessary to activate the crosslinking of the exposed polymer and harden the photoresist. The wafers were then developed in MicroChem proprietary SU8 developer for 60s and washed in isopropanol for 60s too. After development some cracks could be seen around the inside corners of the patterns. This was due to excessive stresses occurring at these points during the development. To solve this a 15 mins hard bake step at 150ºC was added at the end of the process. After the hard bake, the cracks were completely removed.

Electron beam lithography

EBL relies on a high energy electron beam identical to those of scanning electron microscopes to change the solubility of the exposed electron sensitive resist. Compared to conventional photolithography, EBL can comfortably pattern sub-micrometre dimensions with a correctly focused beam. The process does not require masks to create patterns in the resist, as the patterning is done by the relative displacement of the focused beam over the sample. The patterns are instead designed using computer aided design (CAD) software such as AutoCAD from Autodesk. Furthermore, EBL systems come with integrated SEM detectors which, combined with the high displacement accuracy of the stage, makes the alignment of the design to previously exposed patterns extremely easy and tolerant (<1μm alignment error). Here a poly (methyl methacrylate) (PMMA 495K A4, MicroChem) was used as the electron sensitive resist. PMMA was spin coated on the substrates at 4000rpm for 45s and soft baked at 180ºC for 90s. The wafers were then exposed by a Raith e_LINE Plus EBL. A beam current of ≈20nA and a dose of 100 $\mu C.cm^{-2}$ was used for direct writing in the resist. After exposure, the resist was developed for 45s in a 1:3 mixture of Methyl isobutyl ketone (MIBK) and IPA. The development was stopped with a 90s IPA bath.

3.3.2 Metal deposition and lift-off

The fabrication of FETs and photodetectors required the deposition of metals after lithography to create the device electrical contacts. This was done at the Thin film facility of the Department of Physics at the University of Oxford. A thermal evaporator was used to evaporate a metal stack consisting of 5nm of Chromium and 45nm of Gold. After metal deposition, the photoresist was removed using acetone baths, thus lifting off the metals from the unexposed areas of the samples. The lift-off times usually ranged from 45mins to 60mins until the metal layer completely delaminated from the substrate. When required, the samples were gently sonicated to help removing the areas which did not lift off.

3.3.3 Transfer Printing of nanostructures

Transfer printing is a versatile fabrication process used for the assembly of micro and nanomaterials into determined spatial arrangements[128]. Elastomeric polymers are used as stamps to pick up and place the 'ink' on the receiving substrates. The 'ink' consists of a various class of materials ranging from nanoscale materials (QDs[129], NWs[130], graphene[131], [132], DNA[133]…), to fully functional devices (TFTs[134], LEDs[135], photodiodes[136]…). As the process is low cost, scalable, solvent free, efficient at room temperature, and compatible with virtually any substrates, it has become a tool of choice for the development of heterogeneously integrated structures in optoelectronic and photonic devices as well as flexible and stretchable electronics. The various transfer printing approaches can be divided in three categories, depending on the manner with which the stamps are inked: additive transfer, subtractive transfer, and deterministic assembly (Figure 3.1). In additive transfer the stamp is directly inked with the desired material with process such as physical vapor deposition, spin coating, drop casting or even physical transfer. The stamp inked stamp is then brought into contact with the target substrate and slowly peeled back to transfer the ink. In subtractive transfer the material of interest is previously grown on a separate substrate called the donor. The stamp is then

pressed against the donor and quickly picked up, delaminating the material from the source substrate, thus inking the stamp. Printing is then done in an identical manner to that of additive printing. Deterministic assembly is a derivative of the subtractive method where the materials are already pre-patterned on the donor substrate. Peeling the stamp away leads to removal of the selected structures and partial inking of the stamp, which can then be printed on the receiving substrate. All three methods rely on the viscoelastic properties of the stamp to release the ink on the target and/or delaminate the material from the donor.

In terms of kinetics, the printing/peeling process can be explained by the fracture mechanics theory using the energy release rate G which accounts for the energy loss occurring during steady state crack

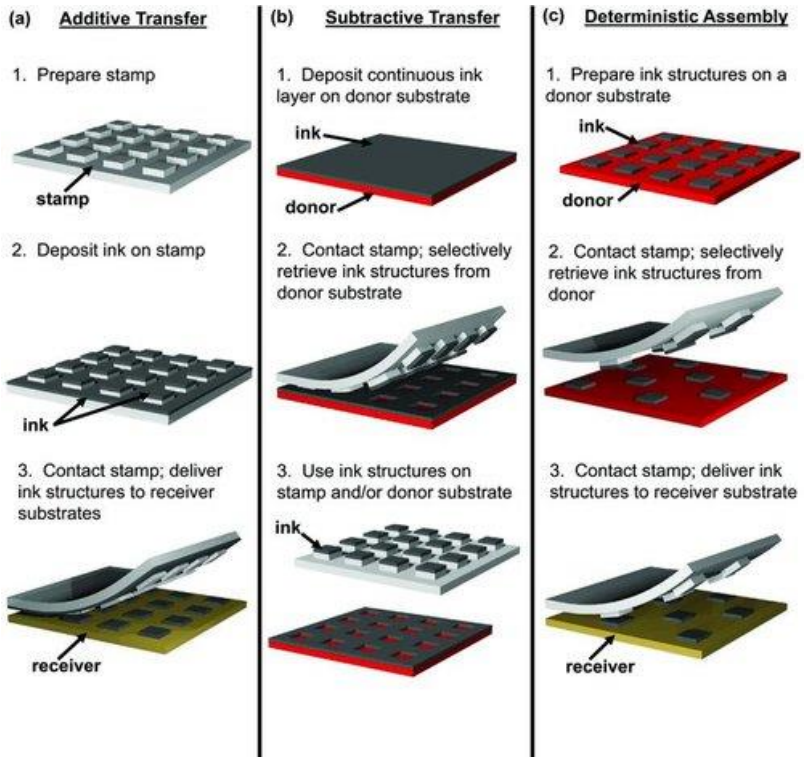

Figure 3.1. The three basic modes of transfer printing. a) Additive printing where the stamps is directly inked with nanomaterials. The stamp is then put in contact and slowly peeled off a target substrate to print the ink. b) In subtractive printing, the inking step is realised by peeling off the nanomaterials from a donor substrate using fast removal of the stamp. c) Deterministic assembly is a derivative of b) where inks are patterned on the donors prior to inking/printing. Reproduced with permission from Reference [128] . Copyright © 2012 WILEY-VCH Verlag GmbH & Co. KGaA, Weinheim

propagation (i.e delamination). In other words, delamination occurs once G reaches a critical release rate. This is related to the peel force by[137]

$$G = \frac{F}{w}, \tag{3.1}$$

where F is the peel force perpendicular to the stamp and w is the stamp width.

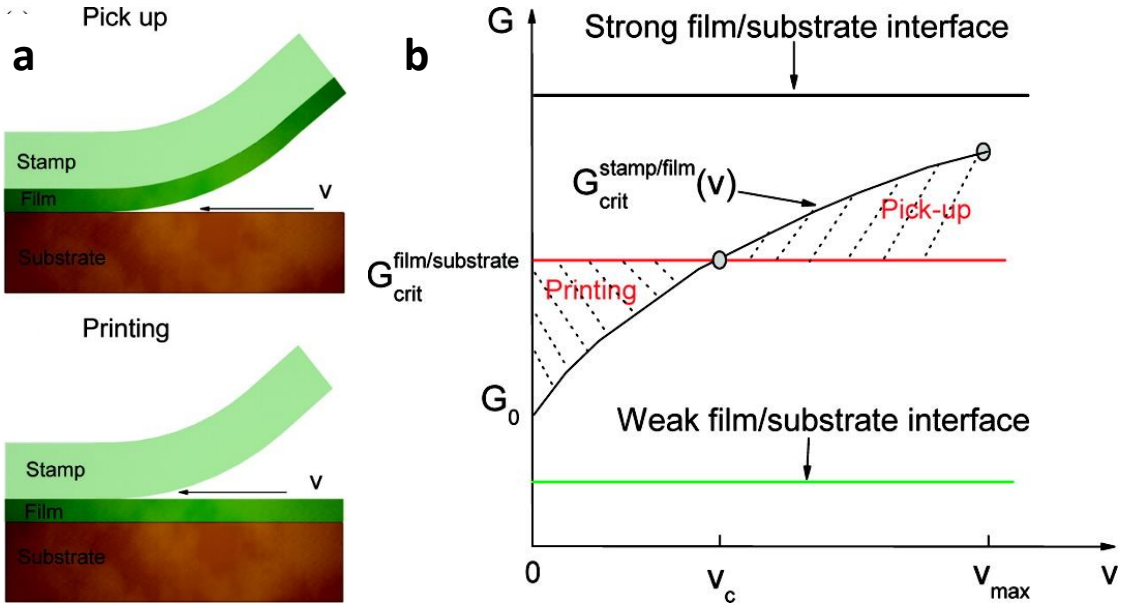

Figure 3.2. The kinetics of transfer printing. a) Schematic diagrams of the pickup (top) and printing (bottom) of a thin film ink, with the two interfaces stamp/film and film substrate depicted. b) Evolution of the film/substrate energy release rate as a function of the stamp peeling velocity. The horizontal red line corresponds to the critical release rate around which the printing/peeling of the thin film can be kinetically controlled. Reproduced with permission from reference [137]. Copyright © 2007 American Chemical Society

As the printing and pick up process involves two interfaces, namely the stamp/ink interface and the ink/receiver interface (Figure 3.2a), two competing fracture pathways occurs with different critical release rates. The energy release rate between the ink and the substrates (donor or receiver) depends on the materials properties which are considered to be elastic. Consequently, the critical energy rate $G_{crit}^{ink/substrate}$ is independent from the peeling velocity v

$$G_{crit}^{ink/substrate} = G_{crit}^{ink/substrate}(v). \quad (3.2)$$

The stamp however is made of viscoelastic polymer (PDMS) and the critical release rate can be modelled as a velocity dependent power law[138], [139]

$$G_{crit}^{stamp/ink}(v) = G_0\left[1 + \left(\frac{v}{v_0}\right)^n\right] \quad (3.3)$$

where G_0 is the release rate at $v = 0$ cm.s^{-1}, v_0 the peeling velocity at which $G_{crit}^{stamp/ink}$ reaches $2G_0$, and the exponent n is a scaling parameter which can determined experimentally. From equations Equation 3.1 and Equation 3.3 the pickup of an ink from a substrate occurs at the peeling force

$$F_{pickup} = wG_{crit}^{ink/substrate} \quad (3.4)$$

and is therefore independent of the peeling velocity. Likewise, the release of the ink from the stamp occurs at a velocity dependent peeling force

$$F_{release} = wG_{crit}^{stamp/ink}(v). \quad (3.5)$$

A criterion can be established for the pickup and printing of the ink based on the peel off velocity of the stamp: pickup occurs when the critical release rate at the ink/substrate interface is reached before the critical release rate at the stamp ink interface or

$$F_{pickup} < F_{release}$$
$$G_{crit}^{ink/donor} < G_{crit}^{stamp/ink}(v) \quad (3.6)$$

and the printing of the ink on the target substrate occurs when the critical release rate at the stamp/ink interface is reached before the critical release rate at the ink target interface or

$$F_{pickup} > F_{release}$$

$$G_{crit}^{ink/target} > G_{crit}^{stamp/ink}(v) \tag{3.7}$$

Therefore, for a specific stamp/ink/substrate combination, peeling from donor substrate and printing on the release substrate can be achieved by tuning a single parameter, the velocity of the stamp. This is illustrated in Figure 3.2b, which plots the critical release rates of Equation. 3.2 and Equation. 3.3. At peeling velocities below that of a critical velocity v_c the energy release rate of the stamp/ink interface is below that of the ink/substrate and printing can be achieved. Conversely, at velocities greater that v_c the energy release rate of the ink/substrate interface is above that of the stamp ink interface and delamination occurs. The critical velocity v_c can be found by equating Equation. 3.2 and Equation. 3.3

$$v_c = v_0 \left(\frac{G_{crit}^{ink/donor} - G_0}{G_0} \right)^{1/n}. \tag{3.8}$$

Note that to ease the pickup, the energy release rate $G_{crit}^{ink/substrate}$ can be lowered by decreasing the surface energy of the donor substrate. This lower $G_{crit}^{ink/substrate}$ and allows to delaminate the ink from the donor at lower velocities (Figure 3.2b).

The pick-up and printing process used in this work are reported in detail in Chapter 7, Section, 7.2. We used a bespoke Nano Imprinter from Seoul Engineering. A schematic of the transfer printing machine is shown in Figure 3.3. The printer consists of an adjustable x-y stage onto which the substrates are positioned for either printing or pickup. The stamps are maintained by a vacuum holder which moves vertically at controllable speeds. Before operation the stamp holder must be aligned with a set of lasers to ensure that the holder is as flat as possible for experiment reproducibility. The stamp holder was transparent so that a set of optics could be focused through and allow manual alignment

of the stamp with respect to the substrates similarly to the alignment of masks and wafers in conventional photolithography.

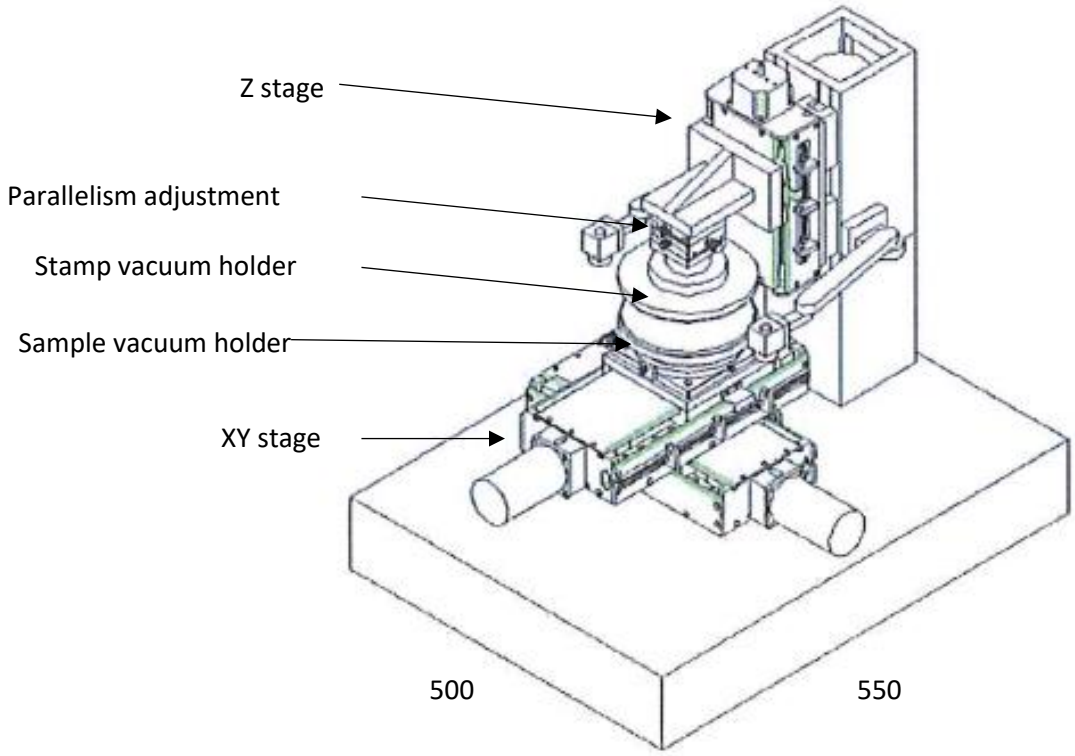

Figure 3.3. Schematic of the transfer printer. Dimensions are given in mm. From the Seoul Engineering manual.

3.4 Measurements

3.4.1 Electrical measurements

To perform time independent measurements such as *I-V* or $I\text{-}V_g$ characteristics, the chips were electrically probed using a Keithley 4200-SCS Parameter analyser connected to a four probes Cascade Microtech probe station (EPS150) located in a shielded enclosure, acting as a physical ground and allowing to perform measurements in dark conditions. For gate field electric measurements, the backgate voltage was created by electrically connecting the doped silicon substrate to a conductive substrate (copper tape) with silver paint. For transient measurements, the probes were disconnected

from the Keithley Analyser and plugged into a low noise current amplifier (Stanford Research Systems SR 570) whose output was wired into a high definition oscilloscope (Lecroy HD4000). When gating was required during transient measurements, the DC gate voltage was applied using a DC external power supply (Kikusui PWR400H).

3.4.2 Photoresponse measurements

Photodetection measurements were made by illuminating the chips from the top with an 850nm laser source (Roithner LaserTechnik LDM850/3LJ) that was externally triggered by a waveform generator (LeCroy WaveStation 2012). The spot size was controlled with an adjustable lens at the end of the laser body. The laser diode was fixed on a vertical mount connected to a manually adjustable x-y stage with a 10μm displacement resolution, which helped with the alignment of the laser spot size on top of the devices. The laser spot size was measured using a CCD camera set up. The accuracy of the CCD measured was double checked with a homemade knife-edge measurement setup, with a laser to detector distance equal to the laser to device distance within the probe station, (millimetre precision) and with the same laser focus, which gave similar spot size values to that observed with the CCD camera.

4 FIELD EFFECT TRANSISTORS AND PHOTOTRANSISTORS BASED UPON P-TYPE SOLUTION-PROCESSED PBS NANOWIRES

4.1 Introduction

For a number of years, semiconductor nanowires (NWs) have been widely investigated for their potential deployment in future electronics and optoelectronics technologies[140]. Their large aspect ratio, typically of the order of a few micrometres in length for diameters of around 100nm, makes them an interesting tool with which to investigate the nanoscale properties of materials. Furthermore, they show outstanding crystalline properties and they enable the fabrication of nanoscale devices without the need for sophisticated patterning processes. As such, a range of promising devices including field effect transistors[141], logic circuits[142], sensors[143], and photodetectors[144] have been demonstrated.

With the advent of bottom-up fabrication methods such as vapour-liquid-solid (VLS) synthesis [145]–[147], there has been a surge in nanowire research because these methods allow for the large-scale synthesis of nanowires with diameters beyond the limits of conventional lithography. However, these vapour-phase synthetic procedures typically require high growth temperatures accompanied by a precise control of the pressure or flow of the reaction gases, which may ultimately impede the large-scale prodcution of nanowires and their potential commercial applications. Therefore, the research focus has shifted towards cheaper and more facile approaches involving the growth of the nanowires from a liquid phase. For such methodologies, nanowires are either grown out of a metallic seed catalyst (e.g. solution-liquid-solid growth (SLS))[148] or out of the oriented attachment of nanoparticles (e.g. colloidal synthesis)[47], [149], [150]. Nanowires can then be readily recovered from the solutions and

deployed into various devices through cost-effective processes such as spin coating/casting[151], spray deposition[152] and doctor blading methods[153].

Solution-processed nanowires are typically grown from inorganic II-VI and IV-VI semiconductors following a synthesis technique that is similar to that employed for the fabrication of colloidal quantum dots (QDs)[46]. Among them, lead chalcogens (PbX, X=S, Se, Te) have shown particular promise for optoelectronics applications due to their extensive band gap tunability[35] and earth-abundant availability. The solution processing of PbS nanomaterials has been used to synthesize complex geometrical structures such as hyperbranched nanowires[44] or star-shaped nanocrystals[154]. However, even though the colloidal processing of PbS nanowires has been reported a number of times[92], [93], a detailed analysis of their optoelectronic performances still remains unexplored.

In this work, we have successfully fabricated single crystalline PbS nanowires using solution processing and have employed them in single nanowire field effect transistor (FET) devices. Even though the device fabrication and measurements were made in ambient conditions, our nanowires are found to exhibit stable hole conduction (p-type semiconductor) with high field effect mobilities that are, on average, larger than 31.6 ± 4.78 $cm^2V^{-1}s^{-1}$, reaching values as high as 166 $cm^2V^{-1}s^{-1}$ for champion devices. To evaluate the potential application of PbS nanowires in infrared-related technologies, nanowire phototransistors were made and their response to an 850nm light source was evaluated. It was found that different photoconductive mechanisms occurred, enabling high photoresponsivity and fast response times by simply tuning the gate voltage.

4.2 Nanowire synthesis and characterization

4.2.1 PbS Nanowire Synthesis

As discussed in Section 2.3.3, the colloidal synthesis of the PbS nanowires is based upon an oriented attachment process [46], [94] where nanowires are grown by first synthesising nanocrystals monomers via a hot-injection process[155], which then combine along energetically favourable crystal faces[42]. By tuning parameters such as the precursor concentration, temperature and reaction time, it is possible to adjust the dimensions of the nanomaterials, making the process extremely versatile[156]. The nanowires synthesis was done by Dr Bo Hou of the NST group. The PbS seed-solution was prepared by mixing lead oleate with trioctylphosphine coordinated sulphur (TOPS). These precursors were swiftly injected into a diphenyl ether solution (ca. T = 250°C) to initialize the oriented attachment growth of PbS NWs. The nanowires were then recovered by centrifuging at 8000 rpm for 10min from an acetone/hexane mixture solution (1:1/V:V). Specifically, 0.3207 g of sulphur was dissolved in 10 mL of trioctylphosphine (TOP) for 2 hours at 50 °C to form the sulphur precursor (TOPS). In parallel, 0.76 g of lead acetate trihydrate and 2 mL of oleic acid were dissolved in 10 mL of diphenyl ether to form the lead precursor. After cooling to 60 °C, the lead oleate solution was mixed with 4 mL of 0.668mol (0.668ml, 1.0M TOPS) TOPS solution in TOP and injected under vigorous stirring into a hot (250°C) solution containing 0.2 g of n-tetradecylphosphonic acid dissolved in 15 mL of diphenyl ether. After 5 minutes of heating, the reaction mixture was quenched to room temperature using a water bath. The nanowires were dispersed in toluene and stored in argon-sealed vials in the dark and at room temperature.

4.2.2 Characterisation

The crystalline structure of the nanowires was characterzed using transmission electron microscopy (TEM) and high-resolution TEM (HRTEM). The nanowires were found to have an average diameter

within the 30-60nm range, and the length could be as long as 10μm. Figure 4.1a shows that the nanowires have rough, zigzag-shaped edges, in line with the observations made by Jang *et al.*[92]. Octahedral shaped nanocrystals (NCs) can also be observed, which are the residues of the PbS seeds that did not take part in the oriented attachment process that formed the resultant nanowires. In the HRTEM image depicted in Figure 4.1b, the {111} crystal planes are clearly observed and reveal a high degree of crystallinity of the as-prepared nanowires. It is shown that the {111} planes are separated by 3.5Å ± 1Å, which is in accordance with that observed for bulk PbS (Power Diffraction File PDF – 78 1057).

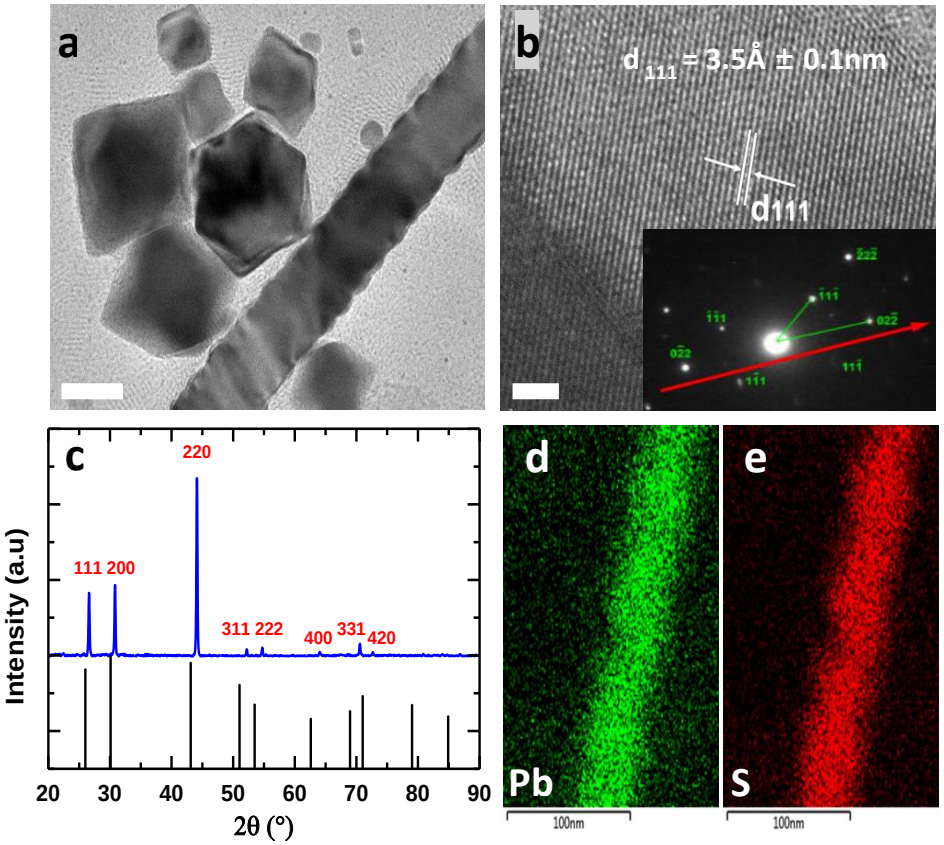

Figure 4.1 Characterization of PbS nanowires. a) TEM image of a 50nm diameter PbS nanowire. Scale bar = 50nm. (b) HRTEM image of the nanowire surface. Scale bar = 2nm. The d111 crystalline planes with 3.5 Å spacing, which matches that of bulk PbS, can be readily observed. SAED pattern (inset, zone axis = [011]) confirms the [110] growth direction. (c) XRD pattern of the PbS nanowires (top, blue) and of bulk PbS (bottom lines, black) from PDF – 78 1057. (d)-(e) HAADFSTEM-EDX element mappings of the as-prepared PbS nanowires to show the presence of Pb and S, respectively. Scale bar is 100nm. Data was acquired by Dr Bo Hou for the NST group.

The x-ray diffraction (XRD) pattern of the as-synthesized nanowires is presented in Figure 4.1c. It is found that the peaks closely match the XRD pattern obtained for bulk PbS (PDF – 78 1057) indicating that the lead and sulfide atoms are arranged in a rock-salt-like cubic structure identical to that of bulk PbS. The slight displacements in the measured XRD peaks compared to the standard bulk PDF values are due to the presence of the glass substrate employed during the measurements. The rock-salt galena cubic configuration can be readily indexed from the selected area electron diffraction (SAED) image (Figure 4.1, inset). The SAED pattern was captured along the [011] zone axis which further confirms the single crystal nature of the nanowires and indicates that growth took place along the [110] direction. To gain insight into the surface composition, we performed high angle annular dark field (HAADF) scanning transmission electron microscopy (STEM) analysis together with element mapping, which confirmed that both lead (Figure 4.1d) and sulphide (Figure 4.1e) were present on the nanowire surface.

4.2.3 Device Fabrication

Photolithography was used to deposit a combination of 5/45nm of chromium/gold electrodes onto a highly p-doped silicon substrate, covered by a thermally grown layer of 3000Å silicon dioxide (SiO_2). The electrode spacing was 5μm. A few drops (~0.2mL) from a diluted solution of PbS nanowires were subsequently spin-cast at 2000 rpm for 30s. Finally, a large amount of methanol was spin-cast onto the devices to ensure removal of the excess of ligands (10 drops, 30s, two times). The devices were subsequently annealed in vacuum at 150ºC to evaporate the solvents and promote electrical conductivity. All the devices that were fabricated were stored in ambient room conditions. Transfer curves and output curves were measured in both dark and ambient conditions (air and room temperature) using a probe station together with a Keithley 4200-SCS parameter analyser. Photodetection measurements were made using an 850nm near-infrared (NIR) laser source (Roithner LaserTechnik LDM850/3LJ) that was externally triggered by a waveform generator (LeCroy

WaveStation 2012). The time response was measured using a digital oscilloscope (Teledyne HDO4104) reading a signal pre-amplified by an I/V converter (Stanford SR570). When required, an external gate bias voltage was applied with the aid of a DC power supply (Kikusui PWR400H).

4.3 Results and discussion

4.3.1 Field Effect measurement

A high-resolution SEM image of a single PbS nanowire bridging over the two Au electrodes after spin coating is shown in Figure 4.2a. Atomic force microscopy imaging (Figure 4.2a, inset) reveals that the nanowire bends at the electrode interface, implying good mechanical flexibility. It also shows that most of the nanowire, and therefore the FET channel, is in contact with the underlying SiO2 dielectric layer. Knowing this, the capacitance of the nanowire can be obtained numerically with the COMSOL Multiphysics software (Figure 4.2b) for a 50nm wide, 5μm long cylindrical nanowire on a 300nm thick SiO_2 substrate and is found to be 3.8×10^{-13} F/cm. This method was favoured over the traditional cylinder on a plate capacitance model, as it has previously been reported that this tends to overestimate the capacitance of back-gated nanowire FETs[157]. With the traditional, analytical model the capacitance is estimated to be

$$\frac{C}{L} = \frac{2\pi\varepsilon_0\varepsilon_r}{\cosh^{-1}\left(\frac{t_{ox}+r}{r}\right)} \tag{4.1}$$

where ε_0 the vacuum permittivity, ε_r the SiO_2 dielectric constant, t_{ox} the dielectric thickness (300nm), L the nanowire length (5μm) and r is the radius of the nanowire(25nm). The analytical capacitance is then found to be C = 6.65×10^{-13} F/cm, which would yield field effect mobilities that are a factor of

two lower than that reported. However, as the order of magnitude remains the same, this does not change the main conclusion.

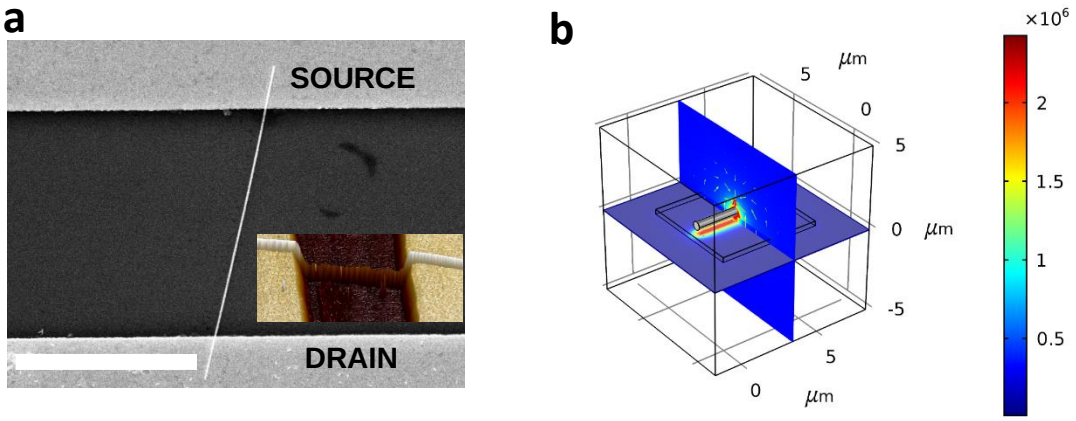

Figure 4.2 a) SEM image of a bottom contact, single nanowire PbS FET. Scale bar = 5μm. The measured diameter of the nanowire is 53nm. The AFM inset shows the mechanical bending of the nanowire at the electrode contacts. b) COMSOL calculation of the back-gated capacitance. A voltage bias of 1V was applied to the bottom surface of the oxide layer and the nanowire was grounded. The colour legend represents the norm of the electric field in V/m. To improve visibility, the diameter of the nanowire shown is in b) is 10 times larger than that used in the actual simulation.

The transistor drain-source current I_{ds} was measured as a function of the bias voltage V_{ds} for different gate voltages, V_g , and the corresponding output curves are presented in Figure 4.3a. The drain current evolves linearly with V_{ds}, showing that ohmic contacts are formed at the PbS/Au interface. It is also shown that I_{ds} decreases with increasing values of V_g, confirming the p-type nature of our PbS nanowires in accordance with previous results reported in the literature[92], [158]–[161]. P-doping of lead chalcogenide structures have been reported to be the result of either a stoichiometric imbalance, where the amount of chalcogen atoms (S, Se) exceeds those of lead[160], or due to oxygen adsorption at the nanowire surface[90], [162], [163]. Scanning transmission electron microscopy (STEM) measurements revealed that the nanowire surface tends to be lead-rich (see Figure 4.9), which leads us

to favour the latter hypothesis, as device fabrication, storage and electrical measurements were performed under ambient conditions, exposing the nanowires to significant amounts of oxygen.

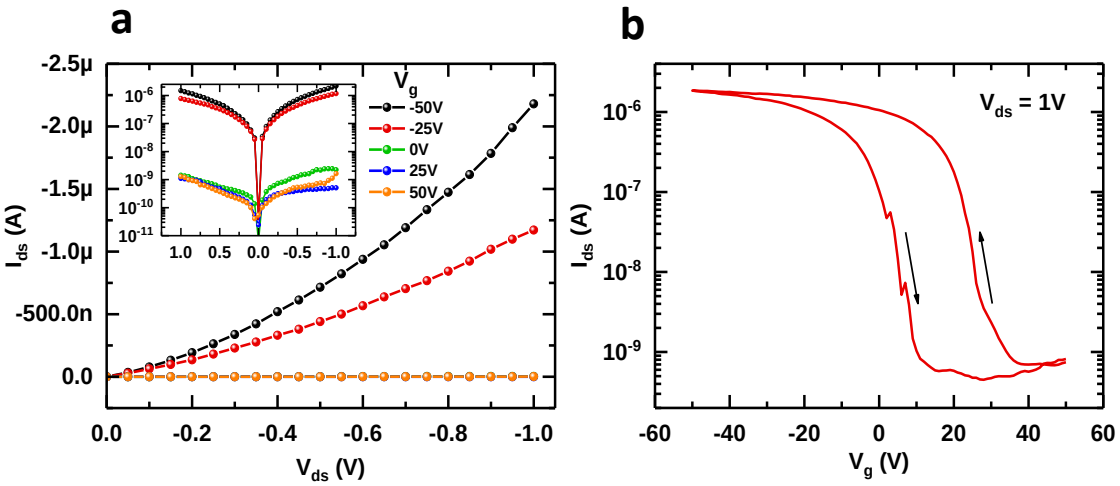

Figure 4.3 a) Output I_{ds} curves of a PbS nanowire for gate voltages ranging from -50V (black) to 50V (orange), in 25V increments. The inset shows the same plot on a log-scale. b) Transfer curve of the same PbS nanowire device; the hysteresis was evaluated by performing a forward sweep with the gate voltage first (i.e. from 50V to -50V for p-type FETs) followed by a reverse sweep in the voltages (-50V to 50V).

The field effect mobility of the nanowires could be deduced from the transconductance relationship, $g_m = \frac{dI_{ds}}{dV_g}$, which was extracted from the transfer curve and plotted in Figure 4.4. To ensure the reproducibility of the device performances, we carried out a statistical analysis of 53 FETs made with nanowires from different batches. The average hole-field effect mobility was found to be 31.6 ± 4.78 $cm^2V^{-1}s^{-1}$ for an ON-OFF current ratio of 1.8×10^3 ± 518. The best performing devices exhibited mobilities as high as 166 $cm^2V^{-1}s^{-1}$ and a 10^4 ON-OFF ratio, suggesting that the device performances could be further improved. These are the highest values reported so far for solution-processed PbS nanowires[92], [93], which compare well with that of solution-based PbSe nanowires[91] and is close to the performance of PbS nanowires grown via chemical vapor deposition (CVD)[160]. The large hole mobility values place PbS nanowires in the upper range in terms of performance of p-type

solution-processed nanowires[164]–[167] (Table 4.1). Furthermore, these results were obtained after one month of storage in ambient conditions, revealing good air stability properties.

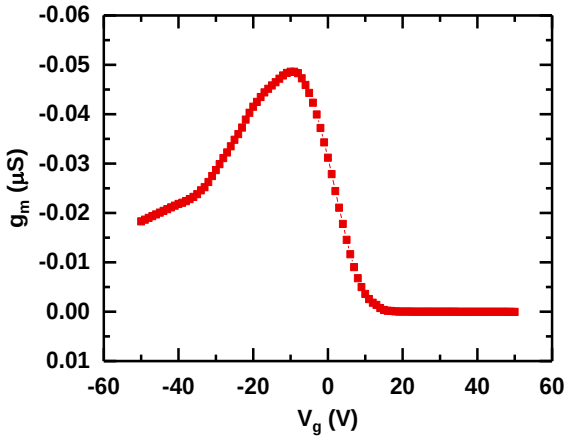

Figure 4.4. Transconductance $g_m = \frac{dI_{ds}}{dV_g}$ of the device plotted in **Figure 4.3**(reverse sweep).

Material	Growth	Mobility ($cm^2\ V^{-1}\ s^{-1}$)	Reference
PbS	solution processed	<10	[92]
PbS	solution processed	0.8 x10-3 @200k	[93]
PbSe	solution processed	15	[91]
PbS	CVD	15-140	[160]
Cu_2O	solution processed	0.15	[164]
ZnO	solution processed	0.8-1.2	[165]
Ge	solution processed	3.0-8.0	[166]
CuP_2	solution processed	147	[167]
PbS	solution processed	31.6	this work

Table 4-1. Summary of mobilities of p-type nanowire field effect transistors quoted in the main text.

In parallel, devices stored in an argon glove box were found to exhibit a hole mobility of 62.3 ± 15.0 $cm^2V^{-1}s^{-1}$ and an ON-OFF current ratio of 2.2×10^3 ± 558.6 (12 devices tested). Both storage

conditions resulted in devices with similar performances and it can therefore be concluded that the ambient storage conditions did not significantly alter the performance of the resultant FETs. Interestingly, an increase in the ON-OFF ratio of the nanowires was observed following aging in both argon and ambient storage conditions and they were found to reach a stable condition after three to four weeks, this phenomenon which we refer to as aging effect will further be investigated in Section 4.4. A gate hysteresis effect can also be observed in Figure 4.3b, which is attributed to the measurement performed under ambient conditions. Indeed, it is known that for one-dimensional FETs, water and oxygen molecules at the semiconductor/dielectric interface can induce charges that screen out the gate electric field, which can, in turn, lead to a hysteresis in the plots [168], [169]. FET parameters such as subthreshold swing (4.4V/dec.), threshold voltage (2.5 V) and free-carrier concentration (3.1×10^{17} cm^{-3}, $n_p = \frac{CV_{th}}{q\pi r^2 L}$) can also be extracted from the transfer characteristics.

4.3.2 Photogating Effect

To demonstrate the potential use of PbS nanowires for optoelectronic applications, the response of the devices to a laser diode was evaluated. Figure 4.5a shows the phototransistor transfer curves measured at various incident illumination powers. A prime advantage of the phototransistor configuration is that the field effect modulation allows for low currents in the transistor OFF state, which enhances the light response while reducing the dark current noise (shot noise). The photocurrent as a function of the laser power P was subsequently extracted and fitted with a power law dependence, $I_{phot} \sim P^{\alpha}$. As can be seen in Figure 4.5b, the photocurrent exhibits different behaviour depending on the gate voltage. Indeed, for positive gate voltages, corresponding to the OFF state of the transistor, the exponent α is found to be close to unity, implying that the photocurrent scales linearly with increasing incident power. However, when going to the ON-state (i.e. negative gate voltages), α

decreases to 0.36 and the photocurrent scales sub-linearly with the power. The different gate-dependent behaviour implies that two different photogeneration mechanisms occur in the nanowire. In the OFF-state, the linear $I_{phot} \sim P$ behaviour is characteristic of the standard photoconductive effect, where photogenerated charges increase the free-carrier concentration in the channel and hence the drain current[170]. On the other hand, in the ON-state the carrier concentration is saturated as indicated by the decrease in the transconductance with negative gate voltage as shown in Figure 4.4. The contribution of photogenerated carriers to the current is therefore limited and a photogating effect appears to dominate.

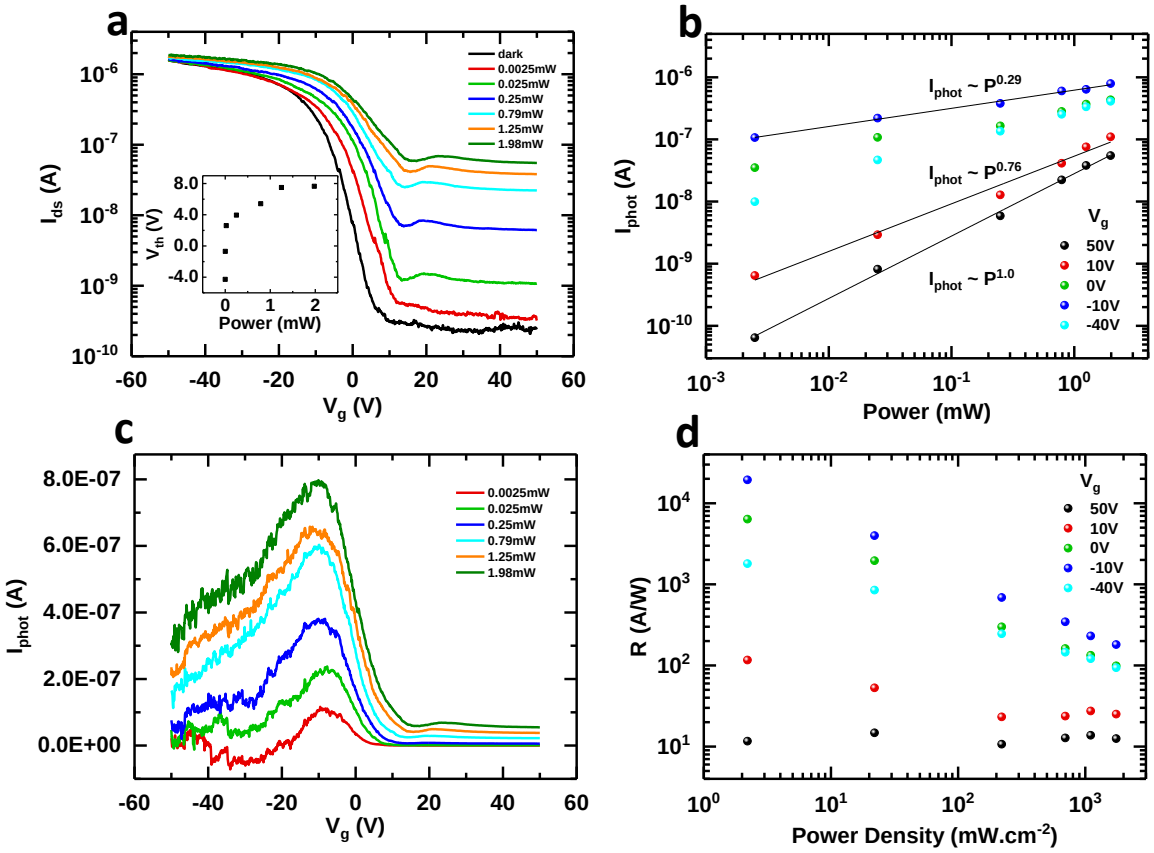

Figure 4.5 a) Transfer curves of a device measured under illumination of an 850nm laser light at different power densities. The inset shows the threshold voltage, V_{th}, as a function of the incident power. (b) Power dependence of the photocurrent, I_{phot} at different gate voltages. (c) Photocurrent $I_{light} - I_{dark}$ as a function of gate-voltage extracted from (a). The negative photocurrent observed at V_g = -30V and P = 0.0025mW is discarded as an uncertainty in the measurement. (d) Photoresponsivity, R, as a function of the power density of the light source for different gate voltages (values were extracted from the data plotted in (b)).

Photogating is an effect that results from the long lifetime trapping of photogenerated carriers in localized states near the band edges, which causes a shift of the Fermi level within the semiconductor[97], [171]. The photocurrent resulting from photogating is proportional to the transconductance g_m (Figure 4.4) and can be expressed as $I_{pg} = g_m \Delta V_{th}$[170], where ΔV_{th} is the variation in the threshold voltage due to a shift in the Fermi level. The shift in V_{th}, plotted in the inset of Figure 4.5a , scales non-linearly with the power of the incident light[170]. The direction of the shift towards positive voltages indicates that electrons become pinned within localised energy states known as trap states, which are believed to be due to interactions between oxygen and the surface of the nanowire as well as interface states that arise from direct contact with the dielectric oxide. Konstantatos *et al.* reported the existence of long lifetime electron trap states in PbS QDs due to the presence of surface lead oxides ($PbSO_4$, $PbSO_3$) and lead carboxylates[105], which could very well be present in our nanowires due to the similarities in the device fabrication and nanomaterial synthesis that have been implemented. Charge trapping effects in PbS NWs will be further investigated in Chapter 5. The proportionality of the photogating current $I_{pg}$with the transconductance is evidenced in Figure 4.5c where the photocurrent measured at different power densities evolves in a similar fashion to the transconductance plotted in Figure 4.4.

4.3.3 Response time

To quantify the response of the nanowire to incident light, we have calculated the photoresponsivity, R, using the relation

$$R = \frac{I_{phot}}{P_d A_{eff}} \tag{4.2}$$

where A_{eff} is the nanowire effective area, approximated to be $2.5 \times 10^{-9} cm^2$ for each device (50nm diameter, 5μm long nanowires), and P_d is the laser power density, which was calculated by dividing

the total power by the laser spot size. From this, the normalized detectivity, D*, of the photodetector $D^* = R(A_{eff}B)^{1/2}/i_n$ could also be determined, where B is the electrical bandwidth and in is the shot noise current, defined as $i_n = (2qI_{dark}B)^{1/2}$, with q representing the electron charge. The power dependent photoresponsivity of the device presented in Figure 4.5a is shown in Figure 4.5c for various gate voltages. In this exemplar device, the responsivity is found to reach a maximum value of 1.9×10^4A/W, which was obtained at the peak of the transconductance (Vg = -10V), a power density of 2mWcm^{-2}, a gate voltage of -10V and a drain bias of -1V. The corresponding value of D* was then calculated to be 1.9×10^{13} Jones. These performance metrics are comparable to that of III-V IR nanowire photodetectors (10^9- 10^{11} Jones)[171]. At positive gate voltages, the transconductance is both constant and minimal (Figure 4.4), resulting in a decrease in the photogating effect as the regular photoconduction mechanism becomes dominant. Therefore, the photocurrent becomes independent of the gate voltage and the measured responsivity was found to be of the order of 10A/W (D* ≈ 10^{11} Jones).

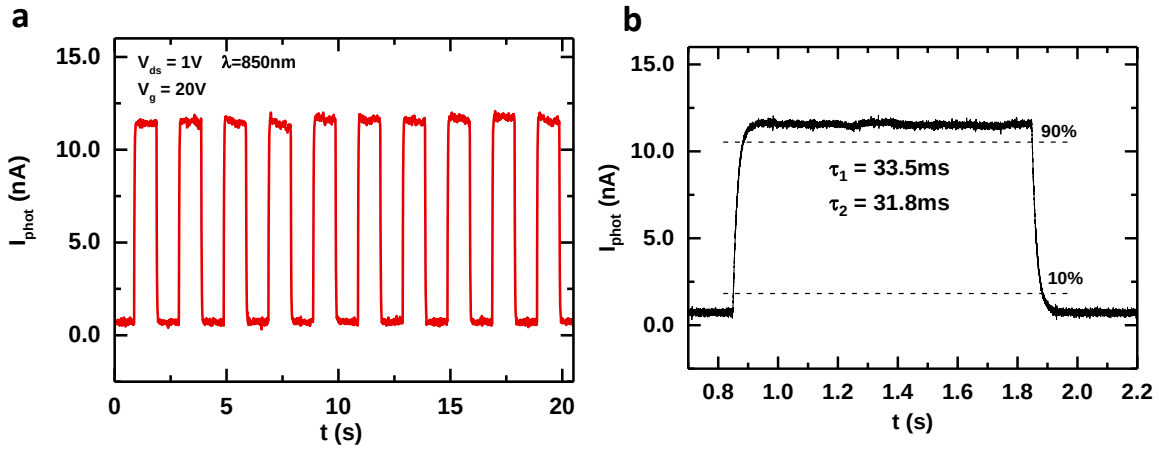

Figure 4.6 a) Dynamic response of a PbS nanowire FET in the OFF state to an 850 nm laser that was pulsed at a frequency of 500 mHz. (b) A magnified plot of one of the crenels shown in (a). The red and blue lines are exponential fits that were used to determine the rise, t_1, and fall times t_2, respectively.

The temporal response of the nanowire FET was also measured, and the photo-switching characteristics are represented in Figure 4.6a (NIR laser pulse 850nm, P = 2.5mW). The time response in the OFF state was measured, where the photoconduction mechanism is dominant, so as to minimize the influence of trap recombination. As gate hysteresis was important, the time response was consistently measured after a short reset to the ON state. The time constants of the photoconductor corresponding to the rise, τ_1, and fall times,τ_2, were extracted with the 10%-90% method (Figure 4.6b). The rise and fall times, which were found to be 33.5ms and 31.8ms, respectively, were obtained at a bias voltage of 1V and are clearly very similar. According to Equation 2.16, this corresponds to a bandwidth of 10.44Hz. It is noted that the switching times of our phototransistors are much faster than that reported for PbSe nanowire-based photoconductors, whose time response has been reported to be of the order of a few seconds [91] and comparable to previously reported CVD-grown PbS nanowires[158], [173]. Beside the fact that in the OFF state the photoconduction is enhanced, we also attribute these good device parameters to the high degree of crystallinity of our nanowires (Figure 4.1), which has previously been shown to enhance the performances of nanostructured photodetectors[174].

4.4 Discussion on the aging effect

It is interesting to note that the nanowires initially exhibited a quasi-metallic behaviour with poor modulation (Figure 4.7a). However, the ON-OFF current ratio increased gradually when the devices were left to age in ambient conditions for several days. Even though a few FETs showed immediate modulation upon deposition, this aging effect was observed in most of the tested devices. To confirm its reproducibility, we performed a statistical analysis over 28 devices exhibiting aging effects on three different Si/SiO2 chips and found that the ON-OFF current ratio consistently increased from below 10 on the day of fabrication to above 10^3 after 30 days of aging (Figure 4.7b). Besides the increase in ON-OFF ratio, other figure of-merits were also found to be affected, as it was observed that the field

effect mobility started at values above 50 $cm^2.V^{-1}.s^{-1}$ and was found to decrease to 20 $cm^2.V^{-1}.s^{-1}$ after 30 days of aging (Figure 4.7c). Passivation of the trap states or surface states can therefore be ruled out for being responsible for the aging effect, since we would expect that trap passivation would have led to an increase in the carrier mobility not a decrease [76], [175], [176]. The voltage threshold, Vth, was also found to decrease with aging and the linear relationship between the majority carrier concentration, n_p, and the threshold voltage[177] $n_p = \frac{V_{th}C}{q\pi\left(\frac{d}{2}\right)^2 L}$, allows us to infer that a significant decrease in the carrier concentration occurs with aging.

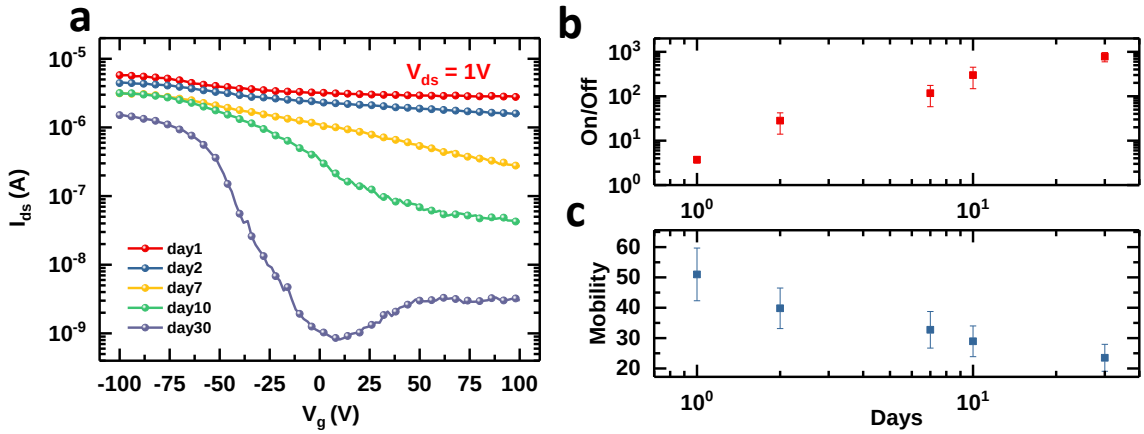

Figure 4.7 a) Effect of aging on the field-effect current modulation of a nanowire FET from deposition (red curve) to 30 days after fabrication while being stored in ambient conditions. b) Plot of the change ON-OFF ratio with aging over 30 days and the corresponding decrease in mobility (in $cm^2.V^{-1}.s^{-1}$).

To shed some light on the origin of the aging effect, the oxidation of the PbS nanowires was studied over time. The p-type conduction originates from the adsorption of oxygen, which acts as an electron acceptor, reducing the electron concentration and increasing the hole concentration[162], [163]. As mentioned earlier, this is the most probable explanation for the p-type nature of the PbS nanowires, since from device fabrication to measurements, they were largely exposed to air. However, prolonged exposure to oxygen could have further oxidized the nanowires resulting in the aging effect. X-ray

photoelectron spectroscopy (XPS) was used to study the evolution of the nanowires Pb oxidation states over time. Initial measurements were made on the day of deposition on SiO_2 substrates, followed by measurements of the aged nanowires a couple of months later. Two different cases were considered, one where the nanowires were left to age naturally in conditions identical to that of the FET devices, and another one where the nanowires were thermally annealed in ambient conditions (45 mins, 90°C) to promote oxidation.

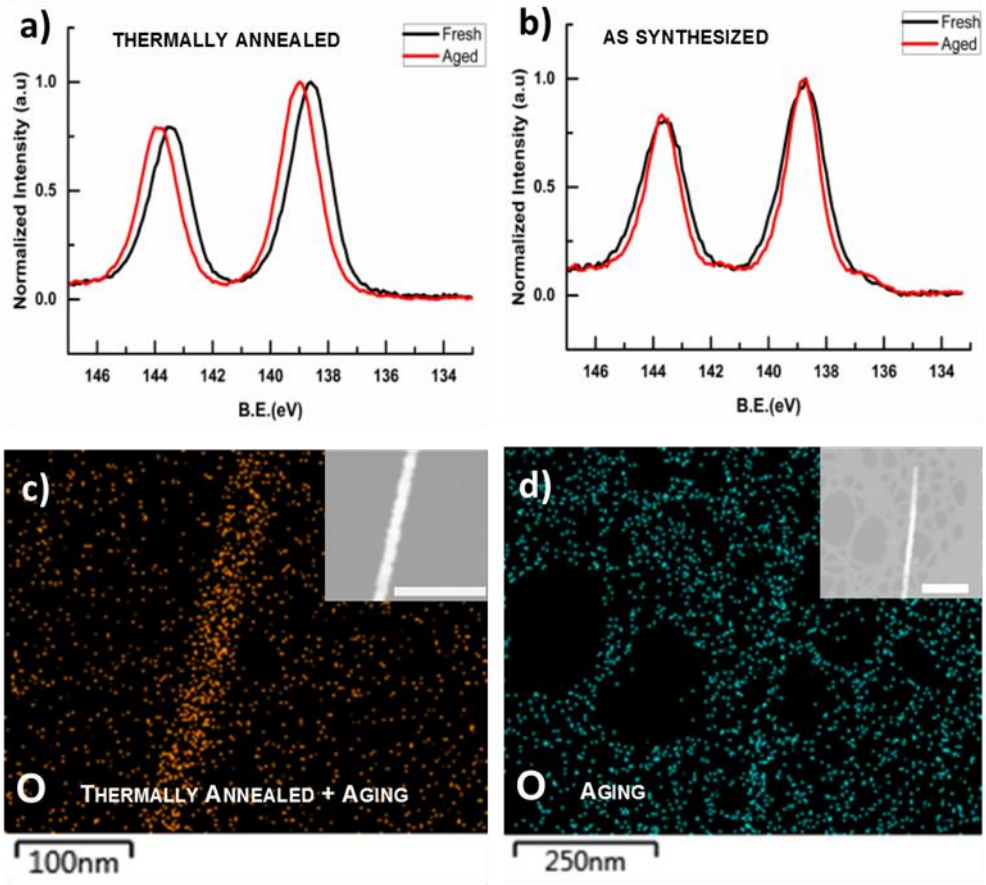

Figure 4.8 a) XPS spectra of PbS nanowires that were thermally annealed in air (90°C, 45mins) and that recorded on the day of deposition (black line). The XPS signal was once again measured after aging in ambient conditions (red line). The shifts towards higher energy suggests further oxidation of the nanowires. b) XPS spectra of PbS nanowires on the day of deposition (black line) and after aging in ambient conditions (red). c)-d) Oxygen STEM mapping after aging (2 months) of nanowires that have been annealed c) and left to age naturally d). Insets are TEM images of the nanowire to show where it is located on the substrate. Scale bars = 250nm

Thermal oxidation under ambient atmospheric conditions of PbS has been reported previously [66], [162], [163] and we aimed at finding out whether thermal annealing could effectively speed up the

aging process. In parallel, STEM mapping of the PbS nanowires was performed under the same conditions (natural aging and aging + thermal annealing). In the thermal annealing case (Figure 4.8a), a clear chemical shift of the Pb4f peaks towards higher binding energies was observed, meaning that the oxidization state of Pb increases with time, in line with the oxidation of the nanowires. Likewise, oxygen mapping using STEM (Figure 4.8c) showed an increase in oxygen concentration at the nanowire surface. The combination of XPS spectrum and STEM mapping allows us to conclude that after thermal annealing and aging, the nanowires are further oxidized. On the other hand, in the natural aging case, no chemical shift of the XPS spectra could be observed (Figure 4.8b). Additionally, the oxygen concentration at the surface is hard to distinguish from background noise levels after 2 months of aging (Figure 4.8d, inset is the corresponding TEM image), suggesting that no significant amount of oxygen is present at the surface of the nanowires. Based on this, we can conclude that thermal annealing under air combined does promote oxidation of the nanowires; however, it is difficult to conclude unequivocally whether further oxidation occurs as a result of a natural aging of the wires, i.e. without thermal annealing. As such, we infer that nanowire oxidation is not responsible for the electrical aging effect observed in Figure 4.7.

The stoichiometry of lead and sulfur at the nanowire surface was also considered. Recent work on PbS QDs FETs showed that sulfur rich nanocrystal films had almost no gate modulation and high p-type conductivity, and presented transfer characteristics similar to that of our devices after deposition [76], [178]. A simple charge orbital framework model allows us to understand the impact of the stoichiometry on the doping of the nanocrystals[179]. In such model, the number of electrons that each atom contributes is closely related to its oxidation state, where atoms with positive oxidation state (i.e. Pb, oxidation number +2) contributes electrons, and those with a negative oxidation state (S, oxidation number -2) contributes holes. Therefore, one can assume that nanocrystals with concentrations of sulfur atoms superior to that of lead atoms will present a high concentration of free

holes and heavily p-type conduction. This was indeed shown in a couple of studies by controlling the concentration of sulfur in PbS QDs with chalcogen salts[76], [178]. TEM and STEM mapping measurements were carried out on nanowires deposited on a TEM imaging grid in conditions that were identical to that of the nanowire FETs.

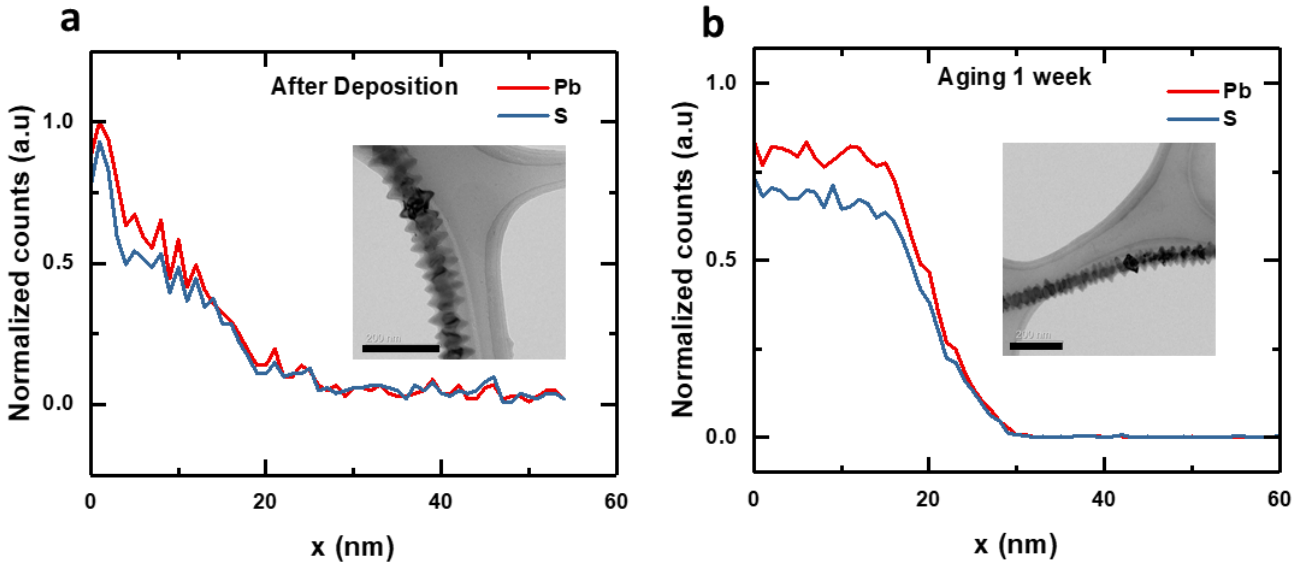

Figure 4.9 a) STEM elemental line scan of a nanowire spin-coated onto a TEM grid (inset) immediately after deposition and annealed in vacuum at 150°C for 30mins to evaporate the solvents and speed up the aging process. Red and blue lines show normalized counts of the Pb and S elements along the scanning axis, respectively. The S:Pb ratios were calculated as the ratio of integrals of the two lines. b) Elemental line scan of a different nanowire on the same grid after a week of aging under ambient conditions. Scale bar 200nm

Figure 4.9 shows the mapping of the nanowire surface before and after one week of aging. It was found that the S:Pb ratio decreased from 0.887 to 0.853 after one week of aging, suggesting a slight reduction in the concentration of sulfur atoms at the nanowire surface. According to the charge orbital framework, the reduction in the sulfur concentration would reduce the concentration of free holes and make the nanowire less p-type in nature, in accordance with the FET measurements. However, the STEM data shows that the surface is predominantly lead-rich regardless of the aging conditions. This implies that the stoichiometry model cannot fully explain the nanowire doping mechanism as this would have meant n-type conduction, which was not observed experimentally. In the light of these

results, it is proposed that the p-type doping comes from the adsorption of oxygen at the nanowire surface which, like sulphur, introduces additional free holes in the nanowire. The hole concentration in the nanowire results from a combination of excess oxygen and sulphur atoms, which results in p-type conduction and no current modulation in the nanowire FETs. As the aging process continues, the concentration of sulphur atoms is reduced and so is the concentration of free hole carriers allowing for current modulation. Further experiments on device fabrication and measurements in rigorous oxygen-free environments would, however, be required to validate this explanation.

4.5 Conclusion

In summary, solution-processed colloidal PbS nanowires that are up to 10μm in length and around 50nm in diameter have been successfully synthesised. XRD and TEM analysis indicated that the colloidal synthesis approach allows for the fabrication of nanowires with a high degree of crystallinity. Single nanowire FETs revealed that the nanowires are predominantly p-type, exhibiting a record hole-mobility of 166 $cm^2.V^{-1}s^{-1}$. The transfer curves exhibited gate-dependent hysteresis, which was attributed to both localized surface states that were formed at the nanowire/dielectric interface and to structural defects. Nonetheless, the devices showed, after an initial period of aging, excellent stability and could be stored in ambient conditions for many weeks without a significant alteration in their performance. Even if not fully explained, the aging effect proved to be consistent and was taken into account in the device fabrication cycle time. Subsequently, the photo-response of the phototransistors was studied, and the devices showed gate-tunable photo-conductivities with a high photoresponsivity in the ON state due to a photogating effect as well as fast response times in the transistor OFF state. The best device in terms of performance was found to have a responsivity and normalized detectivity of 1.9×10^4 A/W and 1.9×10^{13} Jones, respectively, occurring in the linear regime of the field effect modulation. In the transistor OFF mode, where a simple, gate-independent, photoconduction

mechanism is dominant, fast switching times of the order of 30ms were obtained. These high-performance metrics make solution-processed PbS nanowires an exciting material for infrared optoelectronics such as thermal imaging and, more broadly, a functional and economical p-type nanowire.

5 HYBRID 1D/0D LEAD SULPHIDE NANOWIRES AND QUANTUM DOTS PHOTODETECTORS

5.1 Motivations

A major use of quantum dots in optoelectronic devices has been through their integration with other materials such as 2D graphene and molybdenum disulphide (MoS_2) or conducting polymers[14], [15], [111], [180], [181]. The need to combine QDs with highly conductive materials has been driven by the desire to bypass the inherent low electrical mobility of QD films whilst benefiting from the high photosensitivity of the QD layer. Research on these material combinations has resulted in some of the best photoconductors performances reported, with ultra-high gains. Moreover, these findings have initiated research in IR photodetectors based on PbS QDs hybrid structures[14], [15].

Based on the favourable mobility of colloidal PbS p-type nanowires studied in the previous Chapter[95], it was therefore deemed logical to investigate hybrid PbS QD/nanowire structures for the fabrication of photoconducting devices. A schematic of such a structure is presented in Figure 5.1a. In its simplest configuration, the hybrid structure consists of a bottom gated NW FET onto which a layer of PbS QDs is deposited. In this configuration, it is expected that the QD layer acts as a photoactive material and increases the light absorption of the device. Furthermore, Chapter 4 revealed that the devices suffered from remnant hysteresis, which for NW FETs is often attributed to the trapping of charges in the conducting channel or at the dielectric interface. Following on from the findings in the previous chapter, I sought to investigate whether encapsulating the NW devices with a QD layer could help passivate the traps via interfacial charge transfer. Trap states are localized states in the bandgap of a semiconductor which do not contribute to current but induce a shifting of the Fermi level and thus screening of the threshold voltage of a FET which leads to hysteresis. They can be classified as acceptor states which are neutralised when empty but charged when occupied by an

electron, and donor states which are neutral when occupied by an electron but charged when empty[20].

The argument for QD film passivation is as follows: charges could migrate from the QD layer to the nanowire and electrically passivate the trap states by emptying or filling them[182], depending on the nature of the trap. In addition, trap passivation of PbS QDs films has been well studied and it was therefore interesting to see if the strategies used for PbS QDs could be reproduced for PbS NWs[27], [86], [176].

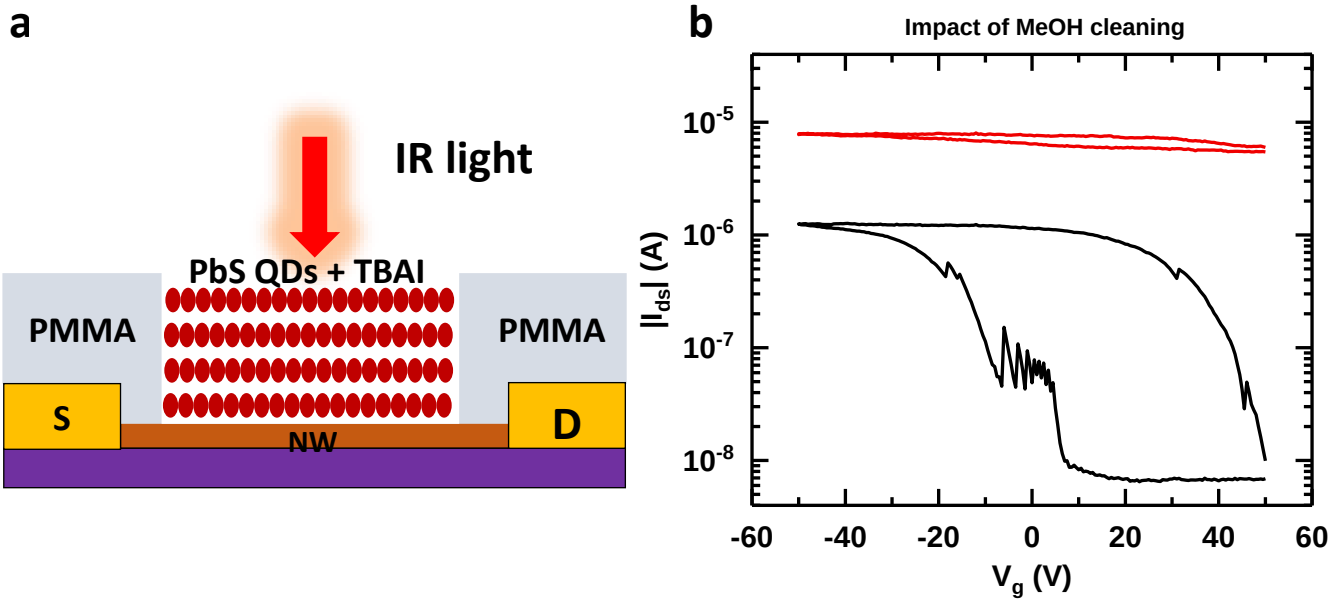

Figure 5.1. a) Schematic cross section of a hybrid NW/QD phototransistor. b) impact of methanol solvent on the transfer curve of bare PbS NWs FETs before (black) and after (red) cleaning in methanol solution.

The deposition of the QD layer proved to be challenging as conventional solvent based spin coating processes can damage the underlying material. Furthermore, spin coating does not allow for the patterning of the QD layer, which can short circuit the transistor drain source current and introduce leakages in the device response. It appeared early in the development process that the methanol solvent used in the ligand exchange step, which was necessary to electrically activate the QD layer, severely damaged the NW FET. Figure 5.1b shows the transfer curves of a NW FET before and after having

been washed with methanol (spin coating of three drops at 3000rpm for 45s). After the methanol wash step, the field effect modulation was dramatically reduced, as observed in the figure. The reason for this degradation in the performance is still unclear but it is believed to relate to the polarity of methanol as other solvents such as toluene and chloroform did not affect the device performances in this way.

A method to circumvent the solvent impact is to anneal the device immediately after exposure allowing for the solvent residues to quickly evaporate. However, this approach was impractical in our case as annealing, even at low temperatures (90-150ºC), resulted in merging (sintering) of the QD layer and loss of quantum confinement, effectively turning the films into amorphous PbS. An alternative approach is to use a dry process based on transfer printing of the QD layer on top of the nanowire devices (Chapter 3, Section 3.3.3).Combined with electron beam lithography, this approach allows for the patterning of the deposited layer, thus avoiding short circuits between the contacts and the QD layer.

The motivations for developing hybrid structures consisting of QDs and NWs were manifold. From a process point of view, developing a fabrication method for the dry transfer and patterning of QDs on top of an electrically active device could be of significant interest for photodetectors based on hybrid QD structures. Additionally, from a device perspective, it would enable us to gain a better understanding of i) the hysteresis occurring in NWs and ii) investigate possible passivation paths using QD film deposition. This Chapter will therefore be divided into three parts. To begin with, the hysteresis nature of QD-free NW FETs will be investigated to bring elements of discussion regarding the possible nanowire passivation with QDs film. For second part, the fabrication process of QD/NW hybrid FETs will be presented together with device characterisation. Finally, these two parts will be brought together and the observed reduction in the hysteresis in the switching of the NWs/QDs structures will be discussed.

5.2 Hysteresis in bare NWs FETs

To better understand the impact of the QD layer on the NW FET hysteresis, we set out to characterize the origin of the gate voltage hysteresis in the NW devices. The gate hysteresis is defined as the difference in threshold voltage measured during the forward scan (OFF to ON, Figure 5.2a A-C) and the backward scan (ON to OFF, Figure 5.2a D-F). The threshold voltage V_{th} is given by[183]

$$V_{th} = \pm \frac{qn_0 d}{C_i} + V_{fb}\,, \tag{5.1}$$

where n_o is the density of free carriers, d is the nanowire diameter, C_i is the dielectric capacitance, and V_{fb} is the flat band voltage which comes from the difference in the workfunction between the gate and the semiconductor. The sign of the first term depends on the sign of the charge carriers (positive for holes, negative for electrons). From this equation, we see that a change in V_{th} can come from either (i) change in the free carrier concentration (doping, trapping), (ii) change in the dielectric capacitance (charge injection, polarization) or (iii) change in V_{fb} (structural changes in the semiconductor).

In our case, a defining feature of the hysteresis is that the backward scan exhibits lower current than the forward scan (Figure 5.2a). Lower backward scan hysteresis has been reported to be due to the trapping of free charges in the channel, which changes the density of free carriers and therefore induces a shift in V_{th}. As the trapping of either minority or majority charges can originate in lower back sweep hysteresis, we employed time domain measurements to identify which type of carrier gets trapped in the NWs FETs. We followed the method proposed for organic field effect transistors reported in references [184], [185] and [186].While continuously measuring the drain current, the devices were initialized by turning them off with an applied gate voltage of 50V for 20s. The transistor switching on was realised in two steps by applying gate voltages of 0V and -50V for 12s to monitor the behaviour

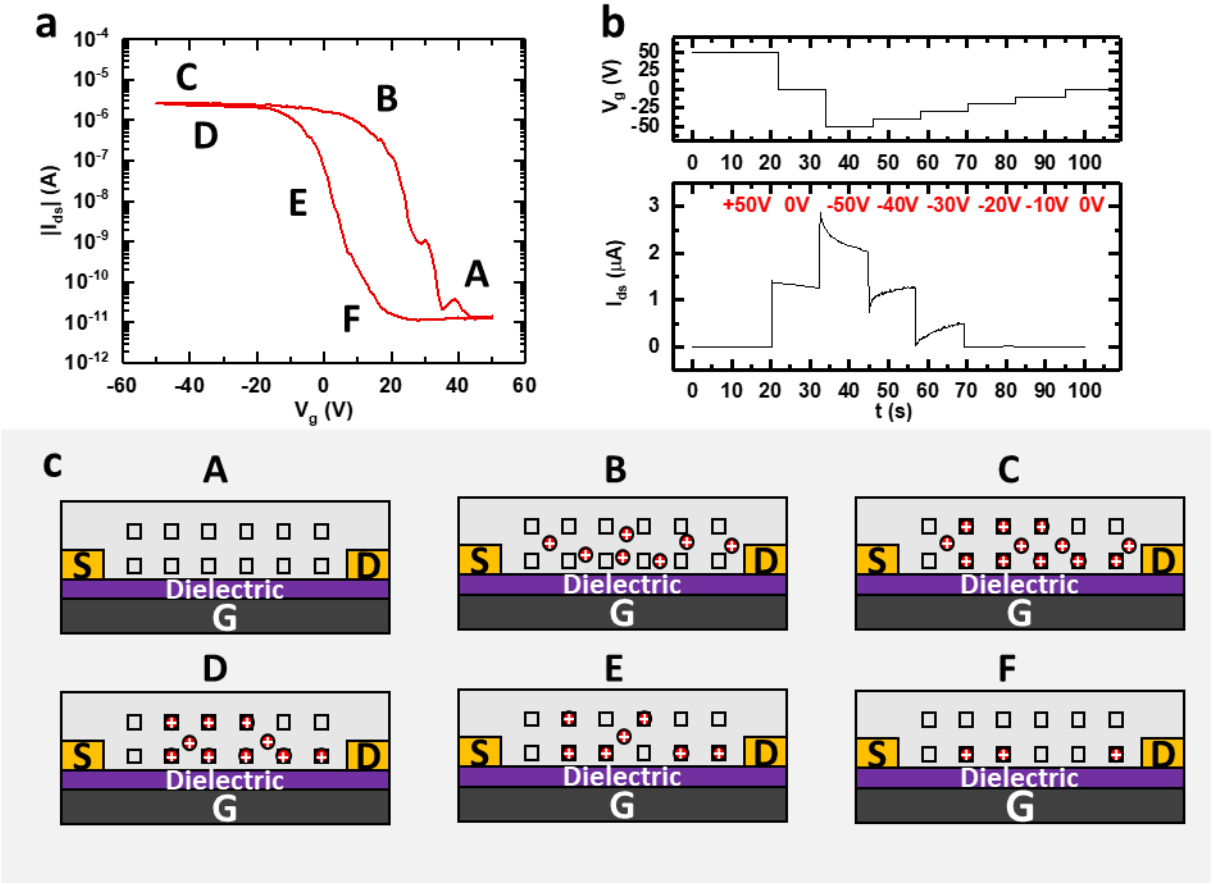

Figure 5.2. a) Hysteresis of a bare NW FET. Forward sweep, or OFF to ON is from points A to C. Backward sweep, or ON to OFF, is from points D to F. b) Transient drain current behaviour of the FET (bottom panel) at various applied gate voltages (top panel). c) Schematic view of the charge trapping occurring in the nanowire at the various voltage points marked in Figure 5.2a. Traps are shown as empty squares and holes are shown as red circles.

of the transistor in respectively the subthreshold state and the turned-on states. The gate voltage was then increased to 0V in 10V steps to slowly turn the transistor OFF again. The transient measured currents (bottom panel) and the applied gate voltage steps (top panel) are depicted in Figure 5.2b. When decreasing voltages are applied, i.e. when the transistor switches from the OFF to ON state, it is observed that, after an initial step-like increase, I_{ds} slowly decays with time. Conversely, when the gate voltage is increased towards positive values, the transistor switches from ON to OFF, and after the initial decrease, the transistor drain current starts increasing again. This transient behaviour is comparable to that of organic pentacene FETs reported by Ucurum *et al* [184] [185], and a hole

trapping induced hysteresis model was proposed to explain the behaviour observed. As positive voltages are applied, the holes are depleted in the channel and the hole traps are therefore empty (A, Figure 5.2c). During the forward scan, once the accumulation condition $V_g < V_{th}$ is achieved, free holes populate the channel and, under the application of a drain voltage, the transistor starts conducting current (B, Figure 5.2c). As $|V_g - V_{threshold}|$ increases, more holes are introduced in into the channel and the I_{ds} further increases until saturation (C, Figure 5.2c).

However as time increases, a growing number of holes become trapped in the hole trap states, which diminishes the free carrier concentration n_0 and causes the current to decay slowly (D, Figure 5.2c). When the transistor is switched back off, the lower hole concentration induces a V_{th} shift towards negative values, as implied by Equation 5.1 and thus gate dependent hysteresis (E, Figure 5.2c). As

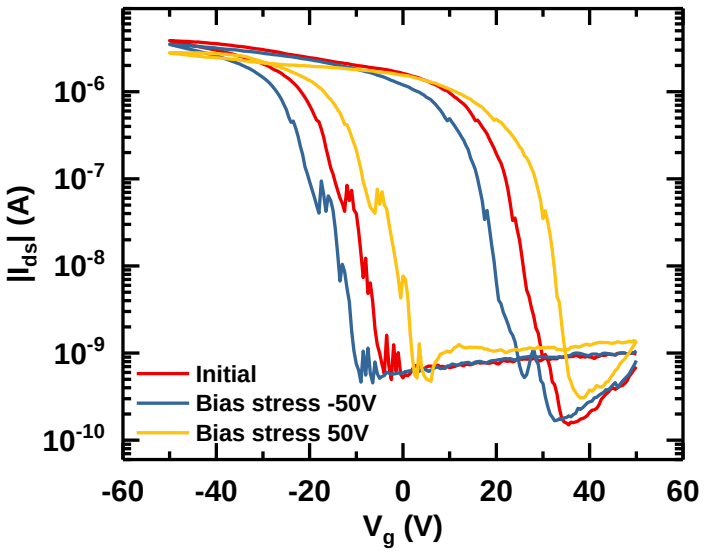

Figure 5.3. Gate bias stress effect in NWs FETs. Observed shift in the transfer curve between an initial measurement (red), a measurement after having applied a gate bias of -50V for 30s (blue), followed by another measurement after a gate bias of +50V for 30s (yellow)

positive voltages are applied, the holes are slowly released from the trap states (de-trapped) and the drain current increases with time after the initial drop. Note that this current recovery cannot be due to the trapping of electrons, as this effect occurs at $|V_g - V_{threshold}| < 0$ where the electrons are still

depleted in the channel. Therefore, in line with the studies of Ucurum *et al*, we conclude that hole trapping mechanism governs the hysteresis in bare NWs FETs.

To illustrate the hole trapping and de-trapping occurring at negative and positive gate voltages, respectively, gate bias stress measurements were also conducted and reported in Figure 5.3. After an initial $I_{ds}(V_g)$ measurement (red line), a gate voltage of -50V was applied for 30s in order to charge the hole traps, which was followed by an immediate second measurement (blue line). The stress time was chosen to be 30s to ensure that the current decay due to trapping reached its steady state value. The decay response time was of the order of a few seconds but varied from device to device so a long enough stress time was chosen to ensure consistency. A shift in the curve to negative values was observed compared to the initial measurement, which we explain by the trapping of free holes, leading to a lower n_0 and , in accordance with Equation 5.1, lower V_{th} values. After this measurement, a positive voltage was applied for 30s to empty the hole traps. As can be expected, this led to a shift of the transfer curve to more positive values, suggesting hole de-trapping and recovery mechanisms. Importantly, bias stress measurements did not lead to quantitative changes in the hysteresis, which suggests that it did not result in irreversible damage to the nanowire.

5.3 Device Fabrication and characterisation

5.3.1 Process

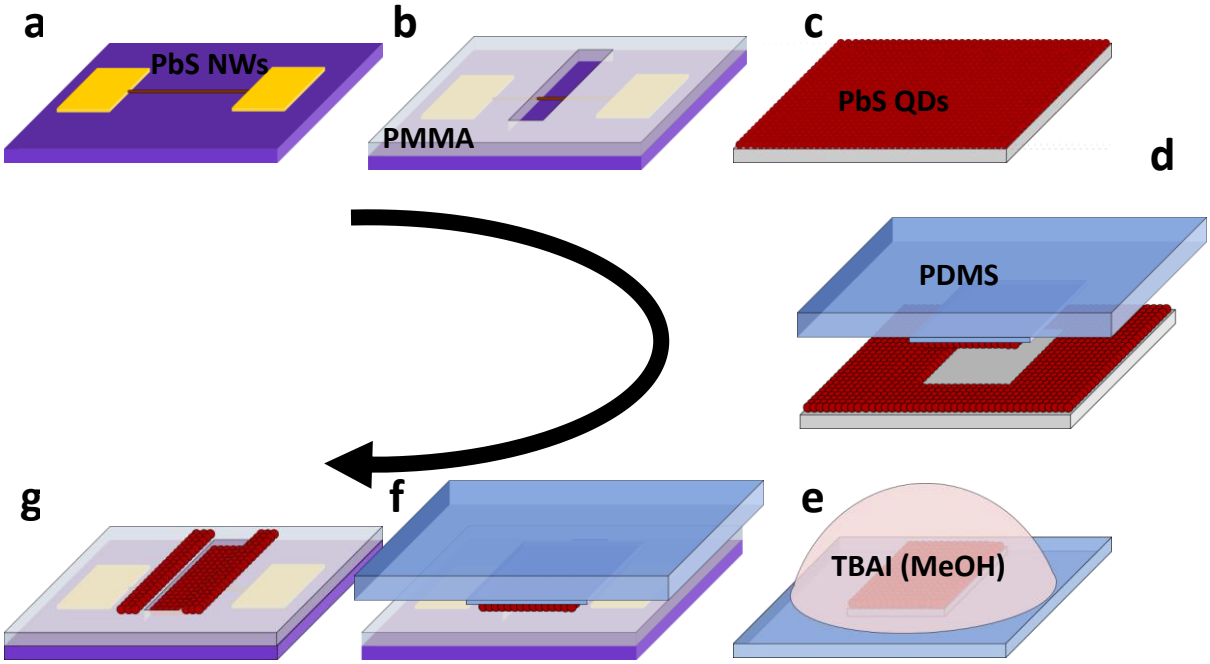

Figure 5.4 . Fabrication process of the Hybrid QD/NWs FETs. a) PbS NW deposition. b) encapsulation in PMMA and the formation of a trench via electron beam lithography. c) spin coating of PbS QDs ononto a silicon source substrate. d) Fast pick of the QD layer on a PDMS stamp. e) TBAI ligand exchange on the stamp. f-g) slow printing and release of the QD layer on the nanowire.

The fabrication process employed a combination of electron beam lithography and nanoimprint lithography and is schematically shown in Figure 5.4. Colloidal NWs are first spin coated from a chloroform solution onto lithographically patterned gold electrodes Figure 5.4a). As NWs FETs tend to exhibit better performances with aging (Chapter 4), the NWs were cured at 150ºC for 30 mins in a vacuum oven to speed up the aging process. A thin layer (180 nm) of polymethyl methacrylate (PMMA) was then deposited and baked at 180 ºC for 90s to act as a sensitive resist for the electron beam lithography. Note that the PMMA did not coat well onto aged substrates, presumably due to organic contamination of the silicon substrate and the PMMA had to be coated right after NW deposition to obtain a smooth coverage. A trench was then etched out using electron lithography and development

in a 3:1 IPA:MIBK (isopropanol, methyl isobutyl ketone) solution (Figure 5.4b). The dimension of the trench was 4 μm × 60 μm and was centred on the 5 μm spacing between the two gold electrodes. The exposure to the developer solvent was the only wet process step used in the device fabrication, but was discarded in the further analysis as after the EBL step the nanowires were annealed and left to age in ambient conditions for two weeks in order to recover the possible loss in the modulation induced by wet processes. On a separate substrate, a self-assembled monolayer (SAM) of octadecyl trichlorosilane (ODTS) was grown onto which a single layer of PbS QDs was subsequently spin coated (Figure 5.4c). The inorganic SAM modifies the surface energy of the silicon substrate and help in the delamination of the QD layer during the transfer printing[135]. A PDMS stamp was made by mixing and stirring 10:1 PDMS and silicone curing agent and left to cure for 2h at 60ºC. The stamp was then used to pick up the QD layer from the source substrate after having been pressed onto it for 30s at an applied load of 0.5kg and then pulled up at a fast speed of 0.5cm.s-1 (Figure 5.4d). The oleic acid ligands surrounding the QDs were subsequently exchanged by shorter TBAI ones to improve the conductivity of the QD film[63]. As it proved difficult to pick up the ligand exchanged QDs from the source substrate and since the TBAI solvent (methanol) was not compatible with the PMMA layer encapsulating the NWs, the ligand exchange step was performed after the inking of the QDs layer on the stamp but before printing. This also allowed for the process to be kept completely dry. A few drops of TBAI were put on the QDs and left still for 30s before spin coating and cleaning in methanol (Figure 5.4e). The stamp was then flipped and aligned onto the trench for printing. Printing was done at an applied load of 1kg for 2mins and then slowly removed (0.1mm.s-1) to release the QD layer using the elastomeric properties of the stamp[187](Figure 5.4f-g).

5.3.2 Characterisation

Hybrid 1D/0D device

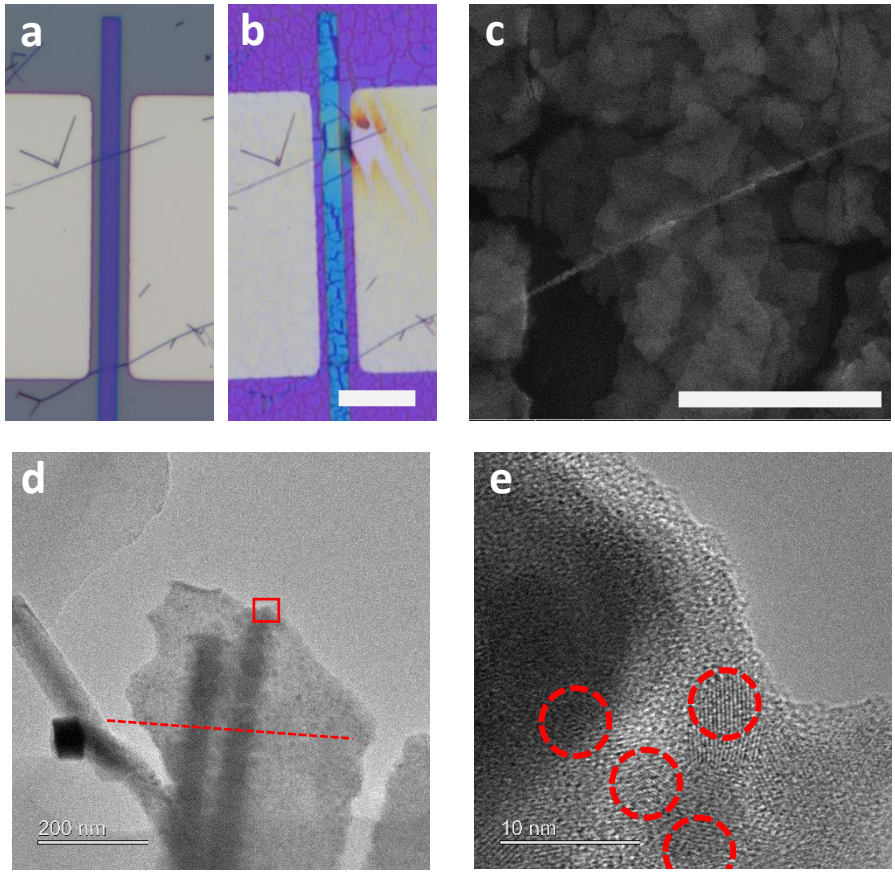

Figure 5.5 Hybrid NW/QD characterisation. a) optical image of the NW FET after PMMA encapsulation and trench opening and b) after transfer printing of one QD layer. Scale bar 5µm. c) SEM images of the hybrid NW/QD layers. SEM scale bar 2µm. d-e) TEM image of a layer of QD printed on a nanowire. The dark areas correspond to the edges of the nanowire. Dashed circles have been added as a guide to the eye.

Optical images of a nanowire device encapsulated in PMMA with an EBL etched trench is shown before QD deposition in Figure 5.5a, and after printing of a single QD layer in Figure 5.5b. A magnified SEM image reveals that after ligand exchange the QD flakes cover the nanowires inside the trench (Figure 5.5c). However, film shrinkage lead to apparition of cracks in the QD film during the ligand exchange process[188], which in turn results in an uneven coverage on the nanowires. The devices were then covered by three QD layers to mitigate this effect. Nanowires were also deposited onto a

TEM grid onto which one layer of exchanged QDs was printed using the steps depicted in Figure 5.4c-f. The ensuing TEM characterisation shows that in the areas where the QD film and the nanowire overlap, the QD film effectively wraps up the nanowire (Figure 5.5d) and that the QDs within the film arrange on top of the nanowires in a disorderly manner (Figure 5.5e).

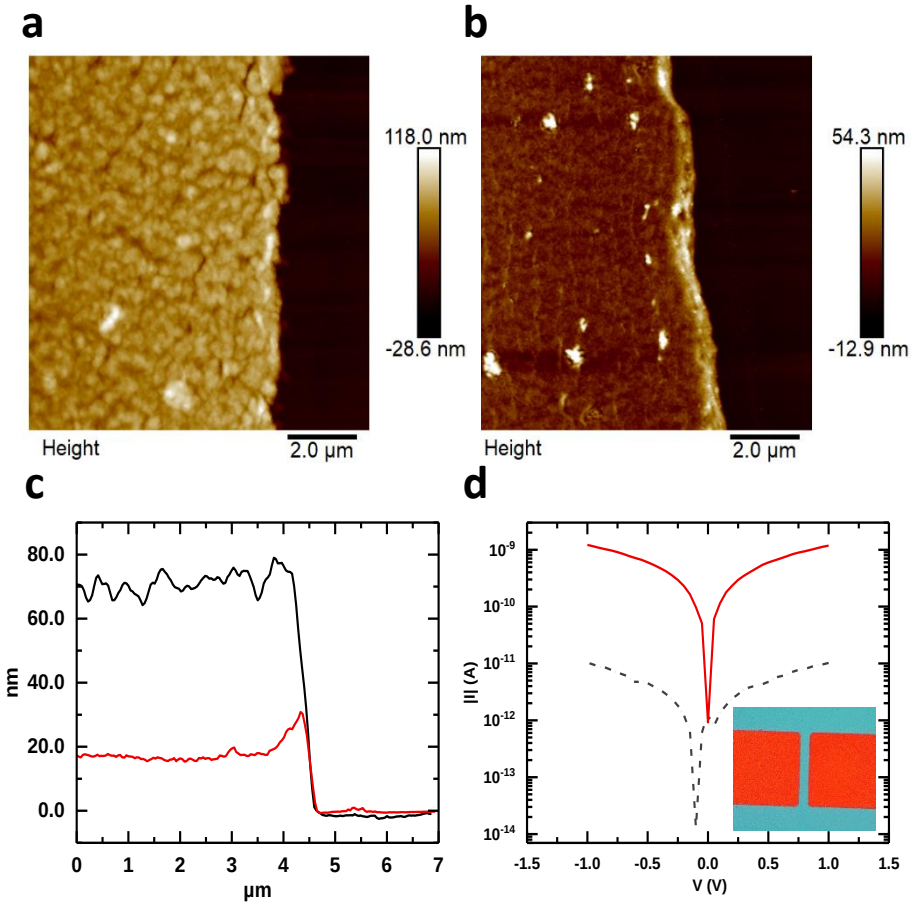

Figure 5.6. Analysis of transfer printed PbS QDs monolayers. a) AFM imaging of the QD film before and b) after TBAI ligand exchange. c) Step profile of the QD film before (black) and after (red) ligand exchange. d) dark current (black) and current under illumination (red) of a simple, monolayer transfer printed photodetector. Inset shows an optical image of the device. Orange areas correspond to the gold electrodes, blue area to the QD film.

QD film characterisation

To evaluate the effects of the transfer printing process on the QD layer, AFM analysis was carried out on printed monolayers. A QD film was transfer printed onto a dummy device with neither NWs nor PMMA and was measured before and after ligand exchange. AFM images show that upon

exchange with TBAI the device thickness reduces from 73 nm to 16nm (Figure 5.6a-c). Furthermore, when biasing the device and illuminating it, a measurable photocurrent was observed, confirming that the QDs still retained their light absorption properties after transfer printing and TBAI ligand exchange (Figure 5.6d). A more detailed analysis of transfer printed QD layers is discussed in Chapter 7, Section 7.3.2 where UV-Vis absorption spectra of printed films is presented. After ligand exchange the first exciton peak was still visible, implying that quantum confinement was not lost (Figure 7.6c) during the printing process.

5.4 Results and discussion

The drain current as a function of the applied gate voltage is plotted for forward and backward sweeps of the gate voltage on the transfer curves of Figure 5.7 in the dark (Figure 5.7a) and under IR light (Figure 5.7b). After printing of the QD layer, a noticeable reduction in the transistor gate hysteresis from 44V to 25.5V is seen. This effect was routinely observed: out of the 15 devices from two fabrication batches, 11 showed hysteresis reduction after QD deposition. Further, a higher ON current was measured at negative gate voltages whenever hysteresis reduction was observed (Figure 5.7a). When IR light was shone onto the devices, the phototransistor light response was nearly unchanged before and after QD deposition. No consistent and reliable increase (or decrease) of the photocurrent could be measured after printing of the QD layers (Figure 5.7b).

Before discussing the possible impact of QD deposition on the NW FET performances, a series of control experiments were carried out to ascertain that the observed behaviours were indeed triggered by the printed QD film. To this end, NW FETs were encapsulated in PMMA in an identical manner to that carried out during **step b** of Figure 5.4. On a separate batch, QD layers were printed on the NW FETs without having undergone the TBAI ligand exchange occurring at step **5.4e**. Finally, pristine

PDMS stamps (i.e. deprived of any QD film) were pressed on some NWs devices using the printing conditions of step **5.4f** to evaluate the possible impact of printing related stress on the NWs.

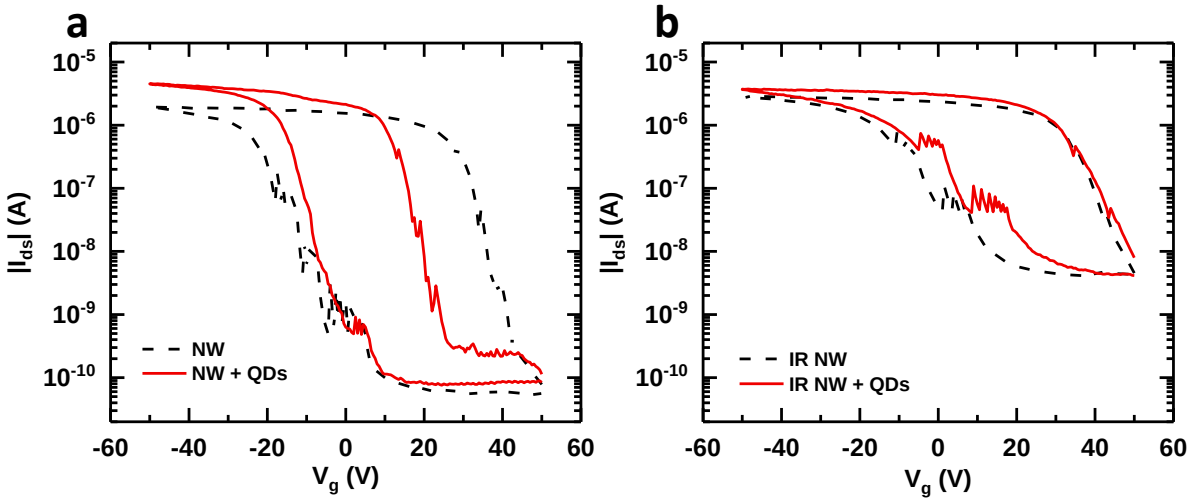

Figure 5.7. a) Transfer curve of NW FET measured before (dashed, black) and after (solid, red) printing of the QD layer. b) Transfer curve of the device shown in a) measured under IR light.

As summarised in Figure 5.8a-c, none of the control devices showed the effects present in Figure 5.7, i.e. a reduction in the gate hysteresis and an increase in the ON current. PMMA encapsulation has often been used to reduce hysteresis in nanowires FETs, due to the polymer hydrophobicity and low oxygen permeability, which prevents oxygen and water adsorption at the nanowire-dielectric interface, a well-known cause of hysteresis in NWs and carbon nanotube FETs[90], [91], [168], [169], [175], [189] This however did not appear to be the case in this experiment, as no hysteresis reduction was observed after PMMA encapsulation (Figure 5.8b). This could be explained by the fact that the NWs FETs underwent several process steps in ambient conditions before PMMA encapsulation and were thus exposed to a significant amount of water and oxygen. To truly state on the impact of PMMA, it would therefore be necessary to perform the NWs deposition, PMMA encapsulation, and electrical measurement in an air controlled environment (such as an argon or nitrogen glovebox).

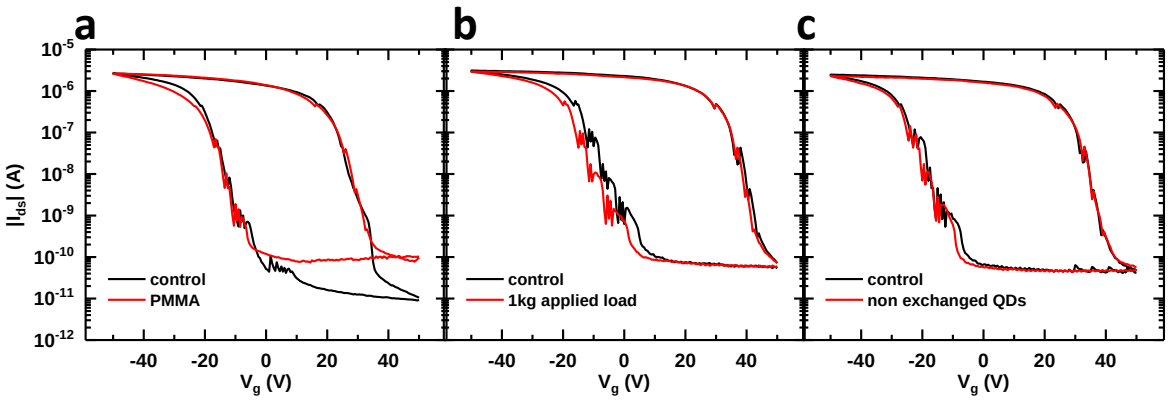

Figure 5.8. Control devices. a) Transfer curves of a device before (black) and after (red) PMMA encapsulation. b) Transfer curve of a device before (black) and after (red) applying a load of 1 kg for 30s onto it with a PDMS stamp. c) Transfer curve of a device before (black) and after (red) printing a layer of QDs without ligand exchange.

In the absence of ligand exchange, the QD films are electrically inert as the large inter QD spacing does not allow for the charge carriers to hop from one QD to another and generate current flow[70], [86]. This reasoning could be applied to NWs/QDs interactions as in the absence of ligand exchange, no impact on the FET hysteresis can be observed (Figure 5.8c). This implies that the QD layer must be electrically activated to interact with the nanowire and that the hysteresis reduction therefore must come from charge interactions between the nanowire and the QD layer. Note that after nanowire deposition (Figure 5.4**a**), the devices were cleaned with EDT to make sure that no insulating ligands were present at the nanowire surface. The intended effect was two-fold since EDT is known to promote oxidation of PbS nanostructures[80] and thus speed up the aging process described in Chapter 4. Apart from faster aging, EDT treated devices did not show sensible difference in performance compared to untreated ones, which suggests that this step might not be critical.

To gain a better understanding of the hysteresis reduction observed after printing of the QD layer, we performed transient measurements of the drain current at different gate voltages before and after QD deposition on the nanowire FETs, following the same method described in Section 5.2. The gate voltage dependent transient current of a NW FET before (black) and after (red) deposition is plotted

on Figure 5.9a. Before deposition, the observed behavior was identical to Figure 5.2b (different device) with decreasing drain current in the ON state due to hole trapping and increasing currents when the transistor is incrementally turned OFF because of hole de-trapping. However, after QD deposition, the transient drain current in the ON state (V_g=-50V) no longer decreases with time but increases (Figure 5.9a, red plot, t=32s to t=44s). From this we hypothesise that hole trapping no longer occurs at negative voltages after QD printing. The reasons for this are considered to be: i) electrical passivation due to transfer of charges between the QDs and the NW channel, and ii) structural passivation of the trap states caused by the TBAI ligands.

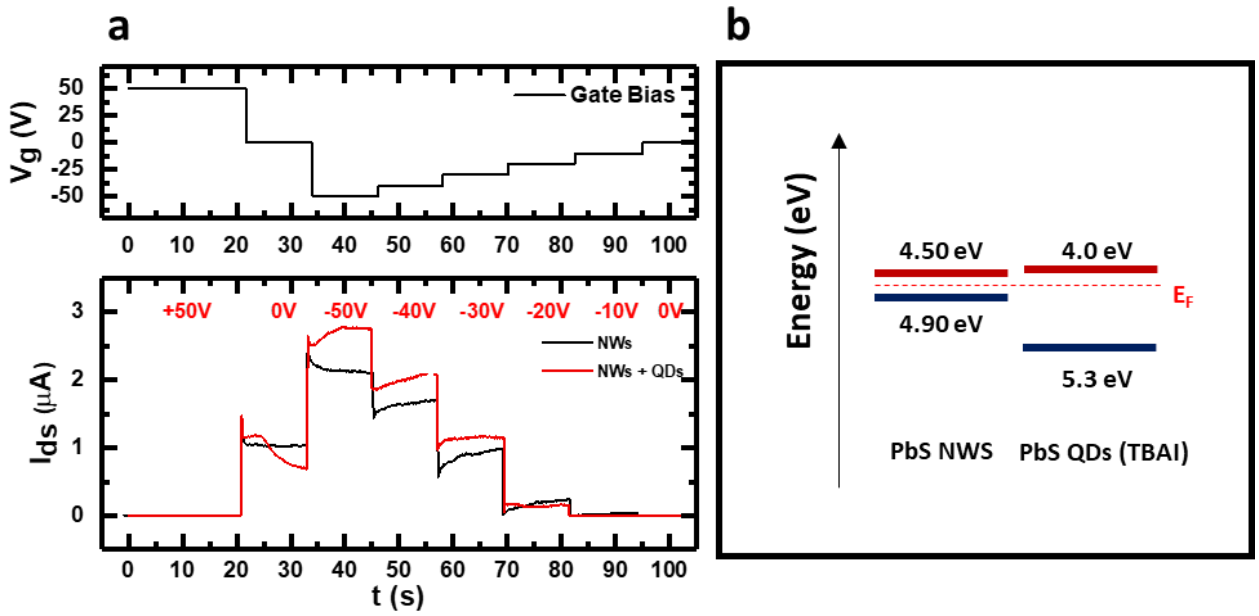

Figure 5.9. a) Transient drain current behaviour of the FET (bottom panel) before (black) and after (red) QD deposition at various applied gate voltages (top panel). b) Energy band diagram of the PbS NWs and PbS QDs treated with TBAI at equilibrium. Energy levels of the nanowires were taken from reference [190] and energy levels of PbS QDs (TBAI) were measured in Chapter 6

QD-NW charge transfer

A schematic energy band diagram of the hybrid QD-NW structure is proposed in Figure 5.9b. As the measured diameter of the nanowires (30 to 60nm) is larger than the PbS exciton Bohr radius (18nm), little to weak confinements effects are expected and the energy levels of the NWs were taken to be those of bulk PbS[190]. The energy levels of PbS QDs are, however, size and ligand dependent

and were consequently measured by UPS spectroscopy and will be further detailed in Chapter 6. Because of the difference in electron affinity and the larger bandgap of PbS QDs compared to NWs, a type II heterojunction is formed were both electrons and holes can be injected from the QD layer into the nanowire. When measuring the transistor current modulation under gate voltages it is therefore expected that different charges will be injected following the direction of the voltage scans (OFF to ON vs ON to OFF). During the OFF to ON scan, a measurable shift in the threshold voltage is observed towards negative voltages, which we attribute to the passivation of holes traps in the channel. Hole traps, also known as donor states, act as fixed positive charges when empty (i.e. occupied with a hole) and as neutral states when occupied by an electron. At positive voltages mobile electrons transfer from the QD layer to the NW and occupy those states, thereby neutralizing, or passivating, them. This results in a shift of the NW Fermi level towards the conduction band. More free holes must therefore be injected to activate the channel which translates as a threshold voltage shift to negative values. In the ON state, these excess holes result in a higher drain current, which is also observed in the transfer plot in Figure 5.7a.

At $V_g = 0$V, electrons stop transferring from the QD layer and the hole trap states are quickly charged. This can be observed in Figure 5.9a at t=20s where the drain current remains constant as long as the hole states are neutralised with electrons and starts decreasing when these short-lived electrons recombine. At negative gate voltages, the donor states are positively charged with holes. However, as holes transfer from the QD layer to the NW and help increasing the free hole concentration thus overcoming the current decrease due to hole trapping. A hole de-trapping mechanism is still evidenced in the backward sweep by the slowly increasing drain current due to de-trapping or recovery.

TBAI Passivation

Another possible explanation for the hysteresis reduction could be attributed to the presence of TBAI to which the NW have been exposed during the printing of the QD layers. As mentioned, trap states are often a consequence of the adsorption of oxygen at the surface of low dimension semiconductors. Therefore, strategies aimed at reducing oxygen adsorption have been investigated in nanowires and carbon nanotubes, most notably using low oxygen permeability polymers such as PMMA[90], [168]. On the other hand, halide compounds such as TBAI have been shown to act as oxygen blockers at the surface of PbS QDs due to the presence of iodine[63], effectively allowing air stable operation of the devices. Along these lines, the presence of iodine at the NW surface could prevent the adsorption of oxygen at the NW surface, thus reducing the density of hole traps and therefore the hysteresis. Figure 5.10a shows the elemental mapping of the nanowire/QD hybrid structure whose TEM image is presented in Figure 5.5. On top of the ubiquitous lead and sulphur elements, a small but non negligible quantity of iodine can be observed throughout the layer. Another control test was performed in which TBAI had been spin coated on a stamp that was subsequently 'printed' on the nanowire, to reproduce the deposition conditions of Figure 5.4 and minimise exposure to solvents.

It is worth mentioning at this point that one of the earliest passivation methods attempted in this work to reduce the hysteresis od PbS nanowires was solid-state ligand exchange using solvent based spin coating, much like that used in the passivation of PbS QDs films. However, no sensible conclusions could be drawn regarding passivation and hysteresis reduction as the methanol treatment damaged the device performances (Figure 5.1b). The plot of the transfer curves before and after the dry deposition of TBAI (Figure 5.10b) shows a small reduction in the nanowire hysteresis. Hysteresis reduction is less important than that of hybrid NW/QD device and was only found in one of the three

treated devices. If the TBAI passivation hypothesis stands, this could be attributed to the poor coverage of the NWs with TBAI using the dry transfer method thereby limiting its efficiency.

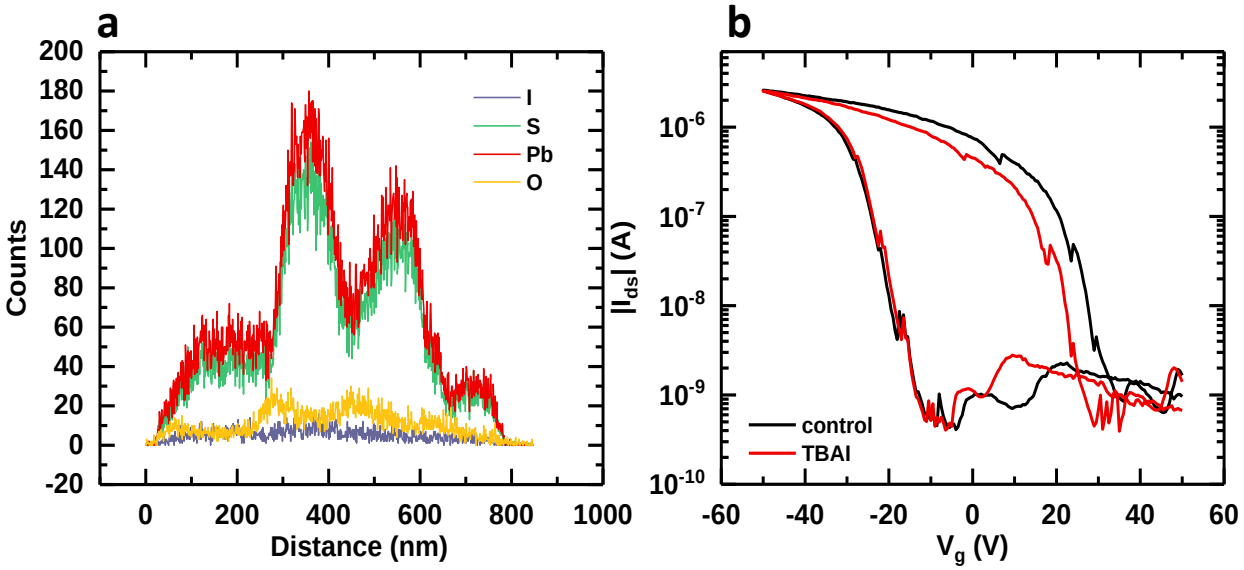

Figure 5.10 a). STEM elemental mapping of the NW/QD hybrid structure shown in Figure 5.5d. On top of lead, sulfur and oxygen, constant traces of Iodine were detected.

We finally looked at the transient response under infrared light for the bare and hybrid devices. To ensure consistency, both devices were measured following the same routines consisting of an initialisation step where a constant positive voltage (50V) is applied for 30s followed by IR measurements at negative gate voltages (Vg = -50V, OFF to ON sweep). After the IR measurements, the devices were kept in the ON state for 30s to stabilize them, then turned OFF by applying a positive gate voltage (Vg = 50V, ON to OFF sweep) and the IR photocurrent was again measured. In the OFF state (Figure 5.11 top panel) the hybrid NWs/QD showed a slightly higher photocurrent of about 5 nA for the presented device, however the devices were quite sensitive to the alignment of the laser spot size, as offsetting the spot size position by a few micrometres could result in lower photocurrent. Therefore, it is sensible to assume that this observed increase of photocurrent falls within the measurement range and cannot be safely interpreted.

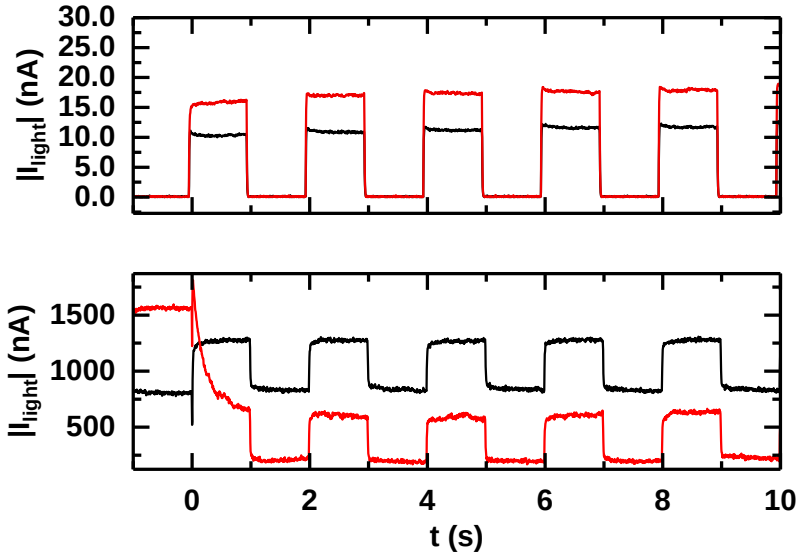

Figure 5.11 (top) Photocurrent time response of a hybrid NW/QD FET in the OFF state (Vg = 50V) before (black) and after (red) QD deposition. (bottom) Photocurrent response of the device in the ON state (Vg = -50V).

In the ON state (Figure 5.11bottom panel) different behaviours were observed between the first on cycle and the following ones for the hybrid structures. On the laser initial rising edge (t=0s) the photocurrent quickly decayed, and the device showed negative photoconductance. During the following laser on periods, normal behaviour was restored, and a positive photocurrent was observed. In the context of the hypothesis of electrical passivation of the trap states with electrons from the QD layer, these results can be explained as follows: under light illumination, the electrons present in the trap states quickly recombine and those are filled with holes resulting in a sharp decrease in the photocurrent. This effectively acts as a reset condition and negates the influence of the QD layer. The ability to reset the charge trapping of the device under light favours the QD/NW charge transfer hypothesis of the device over TBAI passivation as the latter implies permanent passivation whereas the former would be impacted by charge recombination mechanisms.

5.5 Conclusion

In this chapter, hybrid 1D/0D FETs were made based on PbS nanowires and PbS QDs. To bypass device degradation occurring during the deposition of the QD films, resulting from the use of solvents that can damage the underlying nanowires, a novel process was developed using a combination of electron beam lithography (EBL) and transfer printing. PbS nanowires were encapsulated with PMMA into which a window was opened using EBL. PbS QDs, having previously undergone solid-state ligand exchange with TBAI, were subsequently aligned and printed so as to fill up the window and thus form the hybrid device.

As a consistent and measurable decrease of the FET hysteresis was observed upon QD printing, the causes of hysteresis in bare PbS NWs FETs were also investigated. Transient current measurements at different gate voltages revealed that hysteresis occurred due to the trapping of holes in the transistor ON state, decreasing the free carrier concentration and shifting the threshold voltage to more negative values. Two different possible mechanisms were studied to explain the hysteresis reduction, namely electrical passivation of the trap states, which is due to electrons migrating from the QDs so as to neutralize the trap states and the influence of iodine present in the QD layer preventing oxygen adsorption. Since the process was shown to be reversible, the former hypothesis is favoured over the latter as the structural impact of iodine would have been more permanent. Interestingly, no measurable difference in the photocurrent could be measured before and after deposition of the QD layer, despite the increased thickness of the absorption layer. This could be explained by the fact that both types of photogenerated charges could transfer from the QD layer to the nanowire and therefore cancel each other. To counter this, an electron or hole blocking layer could be deposited between the nanowire and the QDs, so as to ensure that only one type of charge can transit from the QD layer to the nanowire. Attempts have been made using a polymer electron blocking layer (TFB), but so far this has

been unsuccessful due to the lack of an optimised method for the dry transfer of the polymer layer onto the NW.

6 SOLUTION PROCESSED PBS QUANTUM DOT PHOTODETECTORS

6.1 Introduction

This chapter presents the photodetection performances of colloidal PbS quantum dots devices made via layer-by-layer deposition. The first part aims at introducing several concepts used throughout this work such as the layer-by-layer deposition technique and the ligand exchange procedure. To that end, photoconductors were made using two commonly used ligands in PbS photovoltaics: tetrabutylammonium iodide (TBAI) and 1,2-Ethanedithiol (EDT) ligands. TBAI is an inorganic n-type ligand, whereas EDT is an organic ligand thought to promote p-type doping of the QDs upon air exposure. These two ligands then cover a wide range of parameters useful for performance optimisation. In the second part, we focus our attention on lateral junction Schottky photodiodes made with an innovative lithography technique, which allowed us to fabricate ultrashort conductive channels between coplanar electrodes. In this work, I have sought to investigate whether the use of channels shorter than the diffusion length of PbS QDs, coupled with the high electric field created across the junction by the Schottky contact, enhanced the performance of a PbS photodiode.

6.2 TBAI and EDT-treated PbS QDs photoconductors

6.2.1 Formation of QD Films

Synthesis of PbS QDs

The synthesis and characterisation of PbS QDs was carried out by John Hong and Dr Bo Hou of the Nanoscience and Technology group at Oxford. The synthesis concept was explained in Chapter 2 and the process has been reported in detail elsewhere[156], [191]. To briefly summarise here, the Pb precursor was prepared by mixing lead oxide (PbO) with oleic acid (OA) and 1-octadecene (ODE) in a 50mL two-neck flask. The solution was heated in two steps: 100 ºC for 3 hours in a vacuum and 130 ºC for 1hour in an argon environment for further precursor treatment. The sulphur precursor was

made by mixing and stirring hexamethyldisilathiane (TMS) and ODE for 4 hours at room temperature under argon. The QD synthesis was triggered by the rapid injection of the sulphur precursor into the Pb precursor solution. Parameters such as reaction time and temperature, which usually govern the growth of the QDs[36], were fixed to 20s and 130 ºC, respectively. Instead, the growth was controlled by the Pb precursor concentration by varying the ratio of PbO to OA. This allows us to manipulate the initial monomer concentration and to precisely control the size of the QDs, independently of other reaction parameters. A high concentration of Pb monomer (e.g PbO:OA = 1:2) results in small diameter QDs whereas a lower concentration (e.g PbO:OA = 1:17) yielded larger QDs. Using this technique, we were able to precisely tune the bandgap of the QDs from 0.84 eV to 1.37 eV thereby covering a large band of the IR spectrum. Figure 6.1a shows the TEM images of as-prepared QDs with different sizes and their corresponding optical bandgap is revealed through absorption measurements as shown in Figure 6.1b. The absorption peak represents the lowest available energy transition level (optical band gap) that corresponds to the first excitonic peak and provides evidence of quantum confinement[21]. As the size of the QD decreases, the optical bandgap increases which translates as a blue shift of the absorption peak in Figure 6.1b In this work, unless otherwise specified, the diameter of the QDs was 3nm, which corresponds to a 1.3eV bandgap. After synthesis, the PbS QDs were dispersed in toluene at a concentration of 50mg.mL^{-1} and stored in dark conditions until device fabrication.

Ligand Solution Preparation

TBAI solutions were prepared using the following procedure. 0.4 g of TBAI powder was mixed using a vortex mixer with 40 ml of methanol (10 mg.ml^{-1}) in a glass vial. Similarly, 1,2-Ethanedithiol (EDT) solution was prepared by mixing 8 μl of EDT and 40 ml of acetonitrile (0.02 v/v%). These ratios were optimized for our group's solar cell work[156], [191]–[193] and kept constant throughout this work.

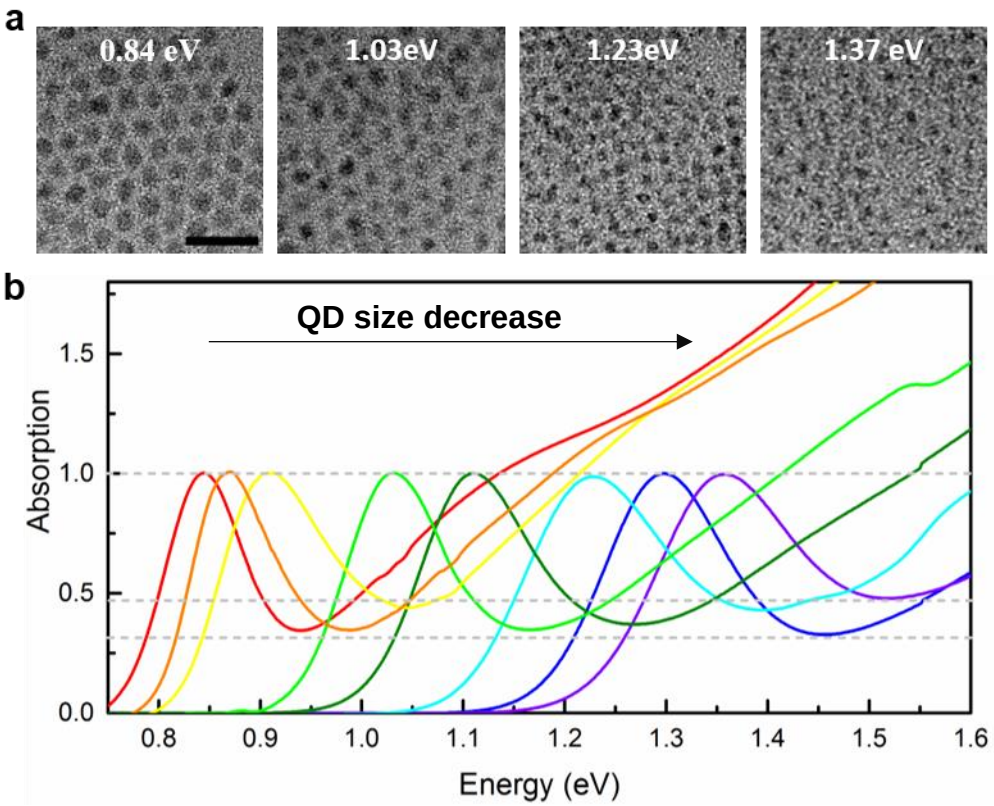

Figure 6.1. a) TEM images of the as-prepared PbS QDs with different diameters and optical bandgaps. Scale bar is 20nm. b) Optical absorption spectra of different diameter PbS QDs. TEM imaging was performed by Dr Bo Hou. QD synthesis and UV-Vis spectroscopy were performed by Dr John Hong from the NST group.

QD Film Deposition

The deposition of one QD layer was carried out as follows: the substrates (SiO_2, Si, Glass, ITO, PET) were first cleaned by an acetone/IPA/DI water wash and then in an O_2 plasma oven for 5 mins. One drop of 50 $mg.mL^{-1}$ of PbS QDs dispersed in toluene was spin cast at 3000rpm for 30s. A significant amount of the ligand solution (usually 10 drops, depending on the dimension of the substrates) was then deposited and left for 30s before spinning again at 3000rpm for 30s to remove the solvent and the exchanged ligands. Finally, the substrates were thoroughly washed in methanol or acetonitrile depending upon the type of ligands used by depositing 10 drops of solvent and spin casting at 3000rpm for 30s. This process was repeated as many times as the number of layers required for device fabrication. When EDT was used, only the first layer was exchanged for 30s, the subsequent

layers were immediately spun after ligand deposition since prolonged exposure to the EDT solution tended to delaminate the bottom layers.

6.2.2 Ligand Exchange characterization

Fourier Transform Infrared (FT-IR) spectroscopy performed on the films before and after ligand exchange provides direct evidence of the successful removal of the OA from the surface of the PbS QDs. Oleic acid is an organic molecule that contains several carbon-hydrogen groups along its carbon backbone and is terminated by a carboxyl group COOH. These bonds can be readily observed using FTIR and the black line in Figure 6.2 shows that the C-H bonds produce vibrations at 3000cm^{-1} while the COOH vibrates at 1300cm^{-1} in a PbS layer encapsulated with OA. After treatment with either EDT or TBAI, these vibrations are reduced which indicates the successful removal of the OA attached to the QDs surface.

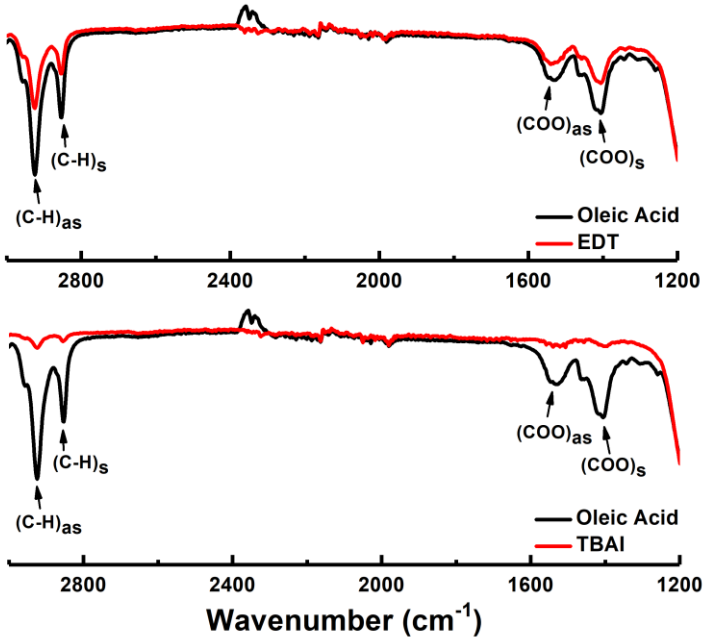

Figure 6.2 Surface analysis of PbS QDs film encapsulated in oleic acid (black), EDT (top, red), and TBAI (bottom, red). FTIR measurement were performed by Dr Yuljae Cho in the NST group

The UV-Vis absorption spectra of PbS QDs with oleic acid and after exchange with either TBAI or EDT are shown in Figure 6.3. As the first excitonic peak is still visible after ligand exchange, one can

conclude that the QDs have not lost their quantum confined nature throughout the process, and that the ligand exchange did not induce sintering of the QDs into bigger particles. For the TBAI case (yellow line) a small shift towards higher energies can be observed, which could be a consequence of the enhanced coupling between the QDs or the changes in the polarization of the dielectric environment[194].

Besides FTIR and UV-Vis spectroscopy, we also investigated the QD films before and after the ligand exchange process using tapping mode atomic force microscopy (AFM). AFM scans along a clean edge of a PbS film passivated with OA, EDT and TBAI are shown in **Figure 6.4**a, b, and c, respectively. The bright areas correspond to the QD layers whereas the dark areas correspond to the silicon substrate onto which the layers were spin coated. The surface roughness of the OA-PbS QDs was measured to be 8.47 ± 1.15 nm, which decreased to 3.65 ± 0.24 nm and 3.14 ± 0.20 nm when treated with either EDT or TBAI, respectively.

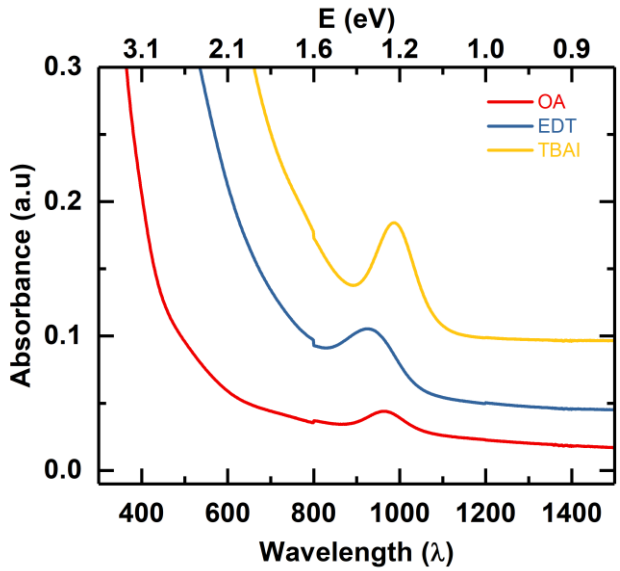

Figure 6.3 UV-Vis absorption spectra of PbQs QDs capped with oleic acid (red), EDT (blue), and TBAI.

The reduction in surface roughness corresponds to a shrinking of the QD layer upon ligand treatment, which decreases the interparticle distance. Interestingly, the surface roughness of the ligand-

exchanged layers closely matches the diameter of the deposited QDs (3nm); however, as the target radius of the AFM tip is reported to be 8 nm in the manufacturer specification, it is difficult to state that one single layer of QD was directly imaged. Likewise, the surface roughness of EDT and TBAI treated films fall within the device measurement limit and should not be interpreted as absolute values. The step profile was extracted from the AFM data and is reported in Figure 6.4d. The average thickness of one QD layer deposited after one cycle of the deposition process described earlier was measured to be 70 nm. After ligand exchange this was reduced to 30 nm and 22.5 nm for the EDT and TBAI cases, respectively. This result, coupled with the lower roughness average for the TBAI-treated layers, suggests that TBAI ligand exchanged films have a higher packing density than the EDT-treated ones.

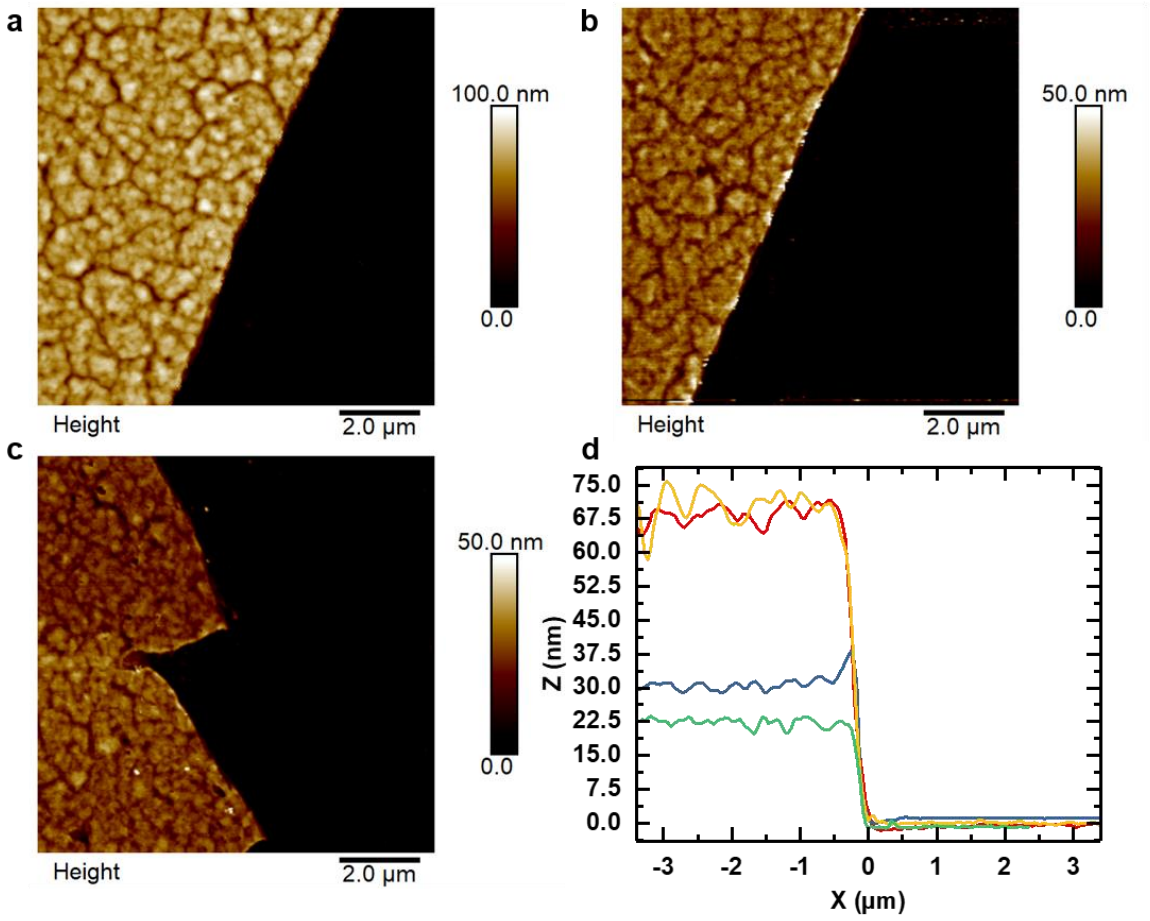

Figure 6.4. AFM height profiles of QD layers encapsulated in a) oleic acid, b) exchanged with EDT, and c) exchanged with TBAI. d) Step measurements of a QD layer before (red) and after (blue) EDT ligand exchange, and before (yellow) and after (green) TBAI ligand exchange.

6.2.3 Photoconductor fabrication and characterisation

Photoconductors were fabricated by depositing layers of QDs onto SiO_2 substrates that were prepatterned with electrodes using photolithography. To enhance the current levels of the devices, an interdigitated pattern was used to increase the width-to-length ratio of the device, which is directly proportional to the current density. The channel length was 10 μm and the total channel area of the device was $A = 3.09$ cm^2. The I-V characteristics of the devices consisting of 1 and 5 layers of ligand exchanged QDs with both EDT and TBAI are presented in Figure 6.5a and Figure 6.5b, respectively. The symmetry of the plots at positive and negative voltage bias indicate that good ohmic contacts are achieved and thus demonstrates that the ligand exchange procedure renders the films conductive even at low applied voltages. The 2-point conductivity of each device was derived from the slope of the I-V curve and is reported in Figure 6.5c. EDT-treated devices consistently showed higher conductivities than the TBAI-treated ones at either one or 5 deposited layers. The conductivity in a semiconductor can be expressed as $\sigma = q\mu_i N_i$, where μ_i and N_i are, respectively, the majority carrier mobility and concentration. Our group has recently calculated the mobilities for EDT and TBAI-treated PbS QDs films using space charge limited current method[191] (SCLC) and found that the EDT-films have a mobility of $\mu_p = 4.4 \times 10^{-2}$cm^2.V^{-1}.s^{-1} while the TBAI-treated films have a mobility of $\mu_n = 3.5 \times 10^{-2}$ cm^2.V^{-1}.s^{-1}. While comparable, these values suggest a slightly better charge transport in EDT-treated film, in accordance with our conductivity measurements.

An increase in the dark current I_{dark} with the number layers is seen in Figure 6.5d. The current in photoconductors follows the ohmic law as $I = \sigma V \frac{WD}{L}$, where $W, D,$ and L are the channel width, thickness and length. Therefore, the current through the device will scale with the device cross-section, WD, as is the case when the number of layers is increased. However, the different linearities of 0.15 nA/layer and 2.9 nA/layer suggest that other factors contribute to the current increase. The first

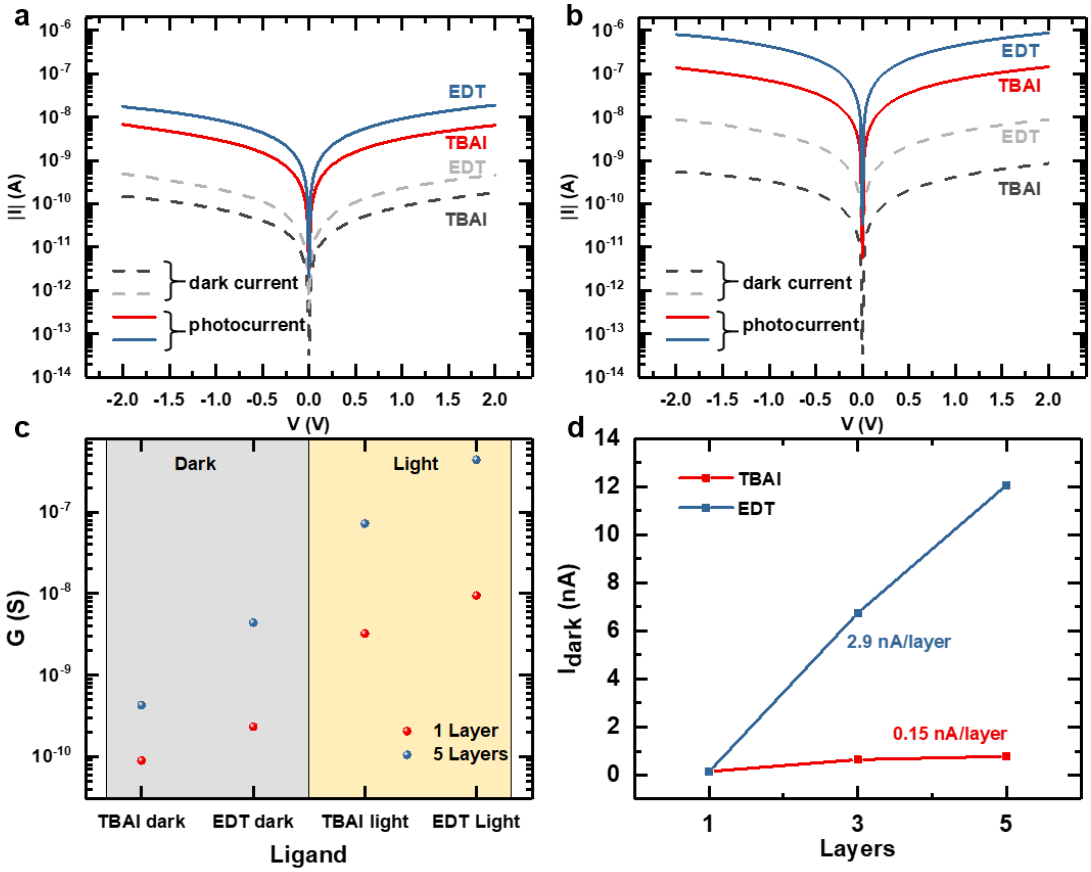

Figure 6.5. Log scale I-V characteristics of PbS QDs photoconductors made from a) single and b) five deposited layers. Dashed lines correspond to dark current I_{dark} and solid lines to current under IR light I_{light}. c) Two-point conductance of the different devices in the dark and under illumination. d) Evolution of the dark current as a function of the number of deposited layers for EDT and TBAI exchanged devices.

potential contribution may be the filling of the micro and nanoscale cracks that occur after deposition because of solvent drying and the reduction in volume due to the shrinking of the layers that occurs with ligand exchange[195]. Another contribution might be the encapsulation of the bottom layers by the top layers, which passivates the charge trapping states induced by surface defects such as dangling bonds[64]. Halide ligands such as TBAI have been reported to passivate surface defects[65], therefore TBAI-treated devices should be less sensitive to the stacking of layers since they are already well passivated, an effect that can clearly be observed in Figure 6.5d.

The photocurrent, $I_{phot} = I_{light} - I_{dark}$, was measured with both TBAI and EDT ligands for single or five deposited layers at different light intensities and the current-power dependence is reported in Figure 6.6a. As expected, the five layered devices showed the highest photocurrents as a result of the increased channel cross-section and of the thicker films. allowing for the absorption of more photons. EDT devices consistently show higher photocurrents, at the cost of a lower device photosensitivity. The sensitivity $S = \frac{I_{light} - I_{dark}}{I_{dark}}$, which quantifies the ratio of photocurrent to dark current, is the main factor influencing the signal-to-noise ratio (Equation 2.13) and is reported in Table 6-1.

	S	
	1 layer	**5 layers**
TBAI	34.9	167.4
EDT	40.2	99.01

Table 6-1. Sensitivity of single and five layer PbS QD photoconductors treated with either TBAI or EDT ligands. measured at 850nm at a voltage of 2V..

Because of the better conductivity, the sensitivity of the EDT-treated devices is found to be higher when only one layer is deposited. This is, however, inverted when increasing the number of layers due to the enhanced dark current. The dark current enhancement of TBAI treated device was however less important which lead to better sensitivities at 5 layers.

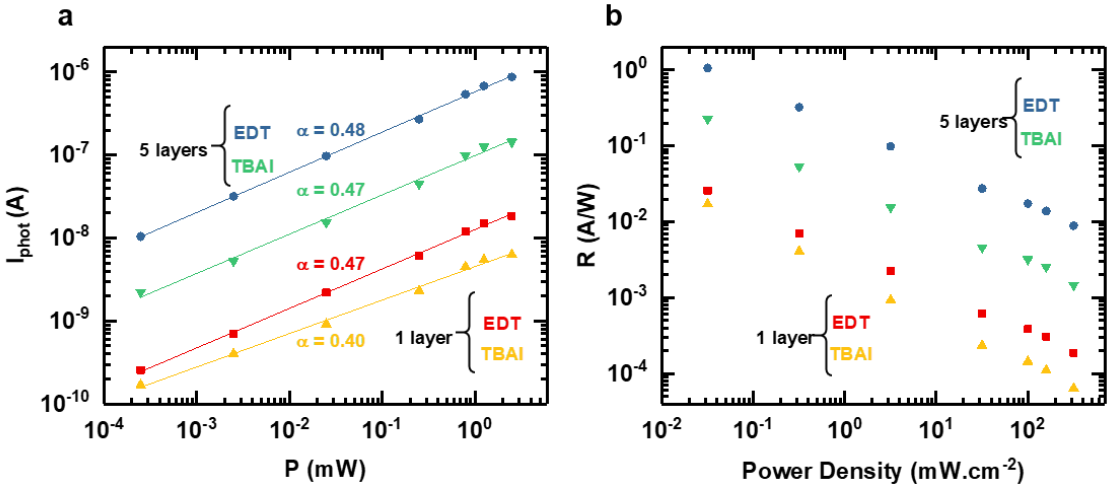

Figure 6.6 a) Photocurrent and b) responsivity as a function of the power and power density for single and five deposited layers devices exchanged with either EDT or TBAI ligands. Bias voltage was 2V.

The dependence of the photocurrent on the light power was fitted with a power-law function $I_{phot} = P^{\alpha}$, with α as the fitting parameter. The fitted values obtained for α range between $0.47 < \alpha < 0.48$, indicating that the photocurrent scales roughly with the square root of the incident light intensity over the range of measured powers. This effect has been observed in other PbS QDs photodetectors[111] and was attributed to losses due to bimolecular recombination, i.e. recombination between photogenerated electrons and holes. The square root dependency indicates that the density of photogenerated charges is much higher than that of trap sites since the photocurrent in devices in which losses are governed by trap recombination mechanisms typically scale linearly with the light intensity[196], [197]. This result could imply either a low density of traps in the QDs layers or that the incident power is too high to reveal losses due to trap recombination. Interestingly, the exponent α for the single TBAI exchanged layers was found to be around 0.4, suggesting that different photoconduction mechanisms occur in this case. We attribute this result to the thinner layer of the QD film, which makes it more sensitive to cracks and defects since transport occurs mostly through percolation pathways through the film, thus affecting the conductivity[198]. Figure 6.6b shows the device responsivity that was derived from I_{phot} using Equation 2.11. The highest measured

responsivity $R = 1.1$ was obtained for 5 layers of deposited PbS QDs treated with the EDT ligand, at an irradiance of 32 μW.cm^{-2} and a wavelength of 850nm The associated normalized detectivity was then calculated to be $D^* = 3.5 \times 10^{11}$ Jones. These values are in range with those reported at 850 nm by Konstantatos *et al.* for EDT-treated devices[105] even though our devices are thinner and higher powers are used. Overall, responsivity is found to decrease with the light power.

To fully characterize the photodetectors, we also measured the transient response of the photodetectors using a laser diode switching at 500 mHz. Figure 6.7a shows the normalized time response of a single layer EDT-treated device measured at different light intensities. The photocurrent consistently showed an initial overshoot followed by a rapid decay upon light excitation. In Figure 6.7b the decay observed between $t = 0$s to $t = 1$s was fitted with a double decaying exponential of the form $y = y_0 + A_1 e^{-\frac{t-t_0}{\tau_1}} + A_2 e^{-\frac{t-t_0}{\tau_2}}$. The fitting time constants τ_1 and τ_2 plotted against the light power (Figure 6.7c) show that the decay speed increases with light power. We interpret this decay as follows: when the laser is turned on for the first time at $t = 0$s the photocurrent quickly rises due to the carriers being efficiently swept by the electrodes. Then the traps are slowly filled resulting in carriers that can no longer contribute to the current[100]. As the light intensity increases, the density of photogenerated carriers increases and the traps are filled proportionally. Simultaneously, the increase in density of the carriers boosts the electron-hole (bimolecular) recombination which also contributes to the light-induced current decay[199], [200]. This result is consistent with the dependence of the photocurrent on the light power shown in Figure 6.6a, which implies that bimolecular recombination is predominant over trap-assisted recombination in the device.

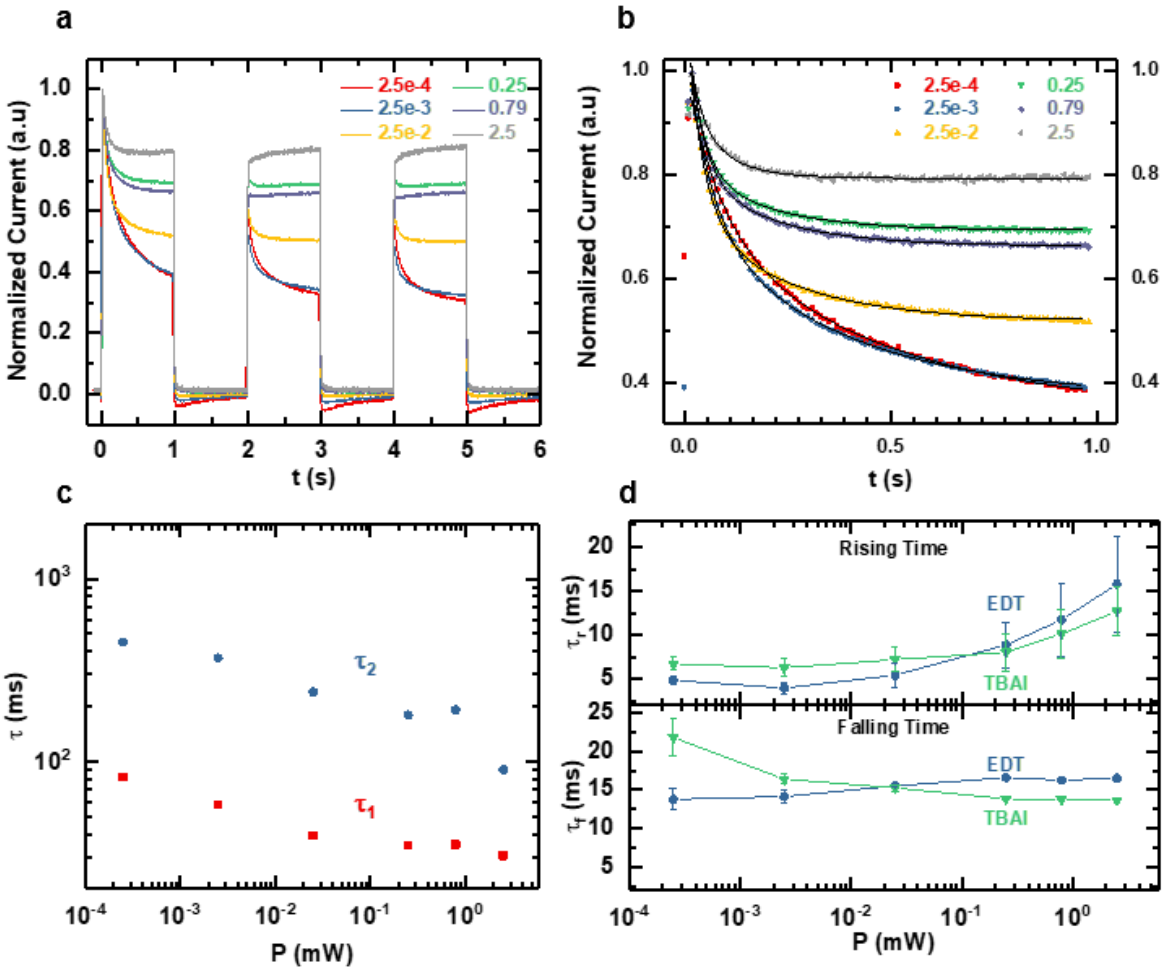

Figure 6.7. a) Normalized time response of a single layer EDT-treated photodetector at various light intensities (in mW). b) Transient decay occurring on the initial turn on of the laser fitted by double decaying exponentials (black lines). c) Time constants extracted from the fitting of b). d) Evolution of the rise and fall times of the TBAI and EDT-treated devices as a function of the optical power.

It is interesting to note that at higher light intensities, the overshoot only occurs when the laser is turned on for the first time but not the subsequent times. The current decay is fast enough to reach its steady-state value during illumination and is not reset during the laser off time. However, turning off the device for a long enough time will reinitialize the overshoot behavior. This suggests a saturation effect at high light power where the traps are inhibited, and the light current is only limited by electron-hole recombination. After the device is switched off the traps are emptied, and the behavior reinitializes. This effect impacts the photodetector rising dynamics as the rise time was observed to

increase with light power (Figure 6.7d, top) due to the vanishing of the overshoot. The fall times remain largely power independent (Figure 6.7d, bottom), which implies that the light power does not affect the de-trapping rate of the device. EDT and TBAI-treated devices showed similar rise and fall times were found to range from 4 to 16ms and from 22 to 13ms, respectively, with a bandwidth of 15Hz.

6.3 PbS Quantum Dot Photodiodes based on asymmetric coplanar nanogap electrodes

6.3.1 Motivations

As discussed in Chapter 2 Section 2.4.2, PbS QDs have been widely investigated as a photoactive material for energy harvesting and infrared photodetection. Because of their tunable bandgap, PbS QDs can cover a wide part of the near-infrared (NIR) spectrum which, combined with the scalability of the solution processed synthesis, makes them a strong candidate for the next generation of flexible and transparent electronics. While photoconductors such as the ones studied in Section 6.2 traditionally exhibit high photoresponsivity, the gain mechanism relies on the trapping of charges in long-lived sensitizing centres, which impedes a fast response time. Photodiodes on the other hand, favour high speed operation with fast transit times of the photogenerated carriers under the action of a built-in potential across the depletion region formed at the diode junction. Numerous PbS photodiodes have been realized so far, with an emphasis on p-n and Schottky junctions commonly found in solar cell technology[102], [119]–[121], [127], [201].

Conventional photodiode fabrication methods rely on vertical structures[119], [125], [201] where the active material is sandwiched between two electrodes. In such structures, the device performance is limited by the active layer thickness with a trade-off between carrier generation and collection efficiency. Thicker layers absorb a large fraction of the incident light, but only the carriers generated in the vicinity of the depletion region can be collected efficiently. Thin films on the other hand have

high collection efficiency but suffer from low photon absorption. Furthermore, the low degree of transparency of the vertical structure makes it impractical for applications in flexible and transparent electronics.

Coplanar diodes using a broad range of materials made via adhesion lithography have been demonstrated by the Anthopoulos group[202]–[205]. Adhesion lithography is a scalable low-cost fabrication technique that allows high throughput fabrication of coplanar asymmetric electrodes separated by a ~15 nm nanogap on a wide range of substrates, including plastics. Nanogap electrodes have several features of interest for PbS QDs photodiodes. The nanometre dimension of the channel means that high electric field can be achieved at low applied voltages and thus fast transit times, which scales as the inverse of the applied electric field ($\tau_{tr} = \frac{L}{\mu\mathcal{E}}$, with μ, L and $\mathcal{E}$ the carrier mobility, channel length and applied electric field, respectively). Furthermore, the electrode width can be arbitrarily long, up to the centimetre scale, allowing for the creation of large device areas as to increase photon absorption. Since PbS QDs have a diffusion length of about 80 nm[118], most carriers generated in the gap can diffuse to the depletion region for extraction, thereby maximising the collection efficiency and thus offering a way to overcome the absorption-collection trade-off.

In this work, we report on the realisation of PbS QDs infrared photodiodes using nanogap electrodes patterned via adhesion lithography. We show that solution processed PbS QDs effectively fill the 20 nm nanogap between asymmetric electrodes to create coplanar Au/PbS QDs/Al Schottky diodes. The unique architecture of the devices resulted in photodiodes with low dark currents and high responsivity, together with a bandwidth of 180 MHz. To the best of our knowledge this is the first experimental report of QD-based infrared photodetectors using nanogap electrodes.

6.3.2 Device design and fabrication

Design Considerations

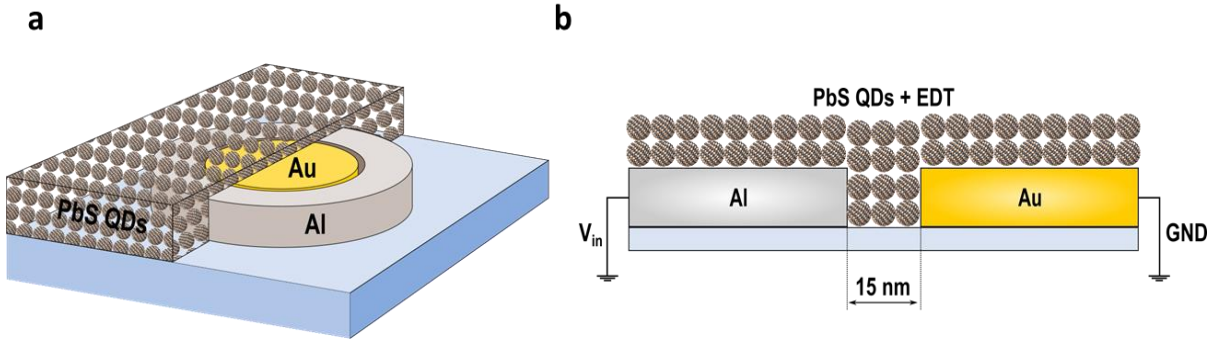

Figure 6.8 a) Schematic of a PbS Schottky nanogap photodiode consisting of coplanar Au and Al electrodes onto which a layer of PbS QDs is deposited. For clarity, only half of the PbS QD layer is pictured. b) Associated nanogap device cross-section depicting the electrical connections used for characterisation.

Schottky diodes were fabricated by depositing a layer of PbS QD films on top of the Au-nanogap-Al device. The Al and Au electrode were patterned as concentric rings separated by a nanogap of length ranging between around 15 nm (Figure 6.8a) via adhesion lithography. Various ring diameters were used from 0.5 mm to 10 mm to scale over different width-over -length ratios. As for the choice of ligand, EDT was preferred over TBAI for several reasons. First, we reported in Section 6.2 that EDT-treated QD films had better photodetection performances in term of responsivity and detectivity due to improved conductivity. The limiting factor was the higher dark current density, which we aim at reducing by using a reverse biased diode. Second, thiols have long been used in self-assembled processes with gold electrodes due to the strong gold-sulphur interaction that facilitates attachment. We posit here that the thiol in EDT will promote the adhesion of QDs to the Au electrode and will help to fill the nanogap and it is likely to induce a directionality that may improve charge transport. Schottky diodes require the formation of an ohmic contact on one side of the junction and a Schottky contact on the other. Our work in Section 6.2 indicates that both TBAI and EDT-treated devices formed ohmic (or near ohmic) contact with gold, meaning that the Schottky contact had to be formed on the aluminium side of the junction. For a p-type semiconductor such as PbS, Schottky contacts are

created if the condition $\Phi_{sc} > \Phi_M$ is met, where Φ_{sc} and Φ_M are the work functions of the semiconductor and metal, respectively. The resulting Schottky barrier ϕ_b can be expressed as[20]

$$\phi_b = E_g + \chi - \Phi_M \tag{6.1}$$

with χ the semiconductor affinity (conduction band edge). In a previous work, we used ultraviolet photoelectron spectroscopy (UPS) to measure the band-edge and fermi levels of 1.25 eV PbS QDs treated with both ligands[191], which are reported in Table 6-2.

Ligand	**E_v (eV)**	**E_c (eV)**	**E_f (eV)**
TBAI	-5.25	-4.00	-4.29
EDT	-4.9	-3.65	-4.36

Table 6-2 Corresponding energy levels of 1.25eV PbS QDs passivated with either EDT or TBAI ligands obtained using UPS spectroscopy. Data was acquired by Dr Yuljae Cho[191].

Considering an aluminium work function of 4.3 eV, Table 6-2 shows that PbS treated with EDT satisfy, theoretically, the condition for the creation of a Schottky contact at the PbS/Al interface. The theoretical energy barrier is then deduced to be 0.6 V. The corresponding energy band diagram is presented in Figure 6.9 where the built-in potential across the junction, due to the work function difference between aluminium and gold, can be observed along with the Schottky barrier.

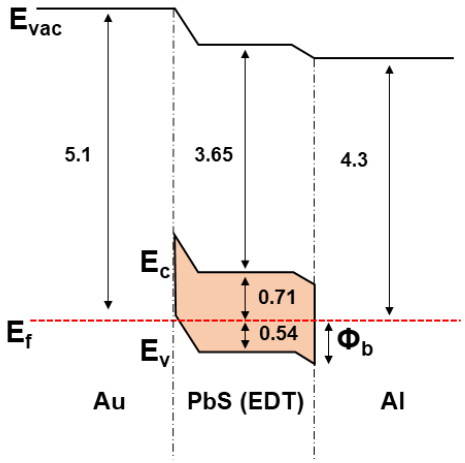

Figure 6.9. Schematic energy band diagram of the EDT-PbS Schottky photodiode drawn with data extracted from Table 6.2

Adhesion Lithography

Adhesion lithography allows the fabrication of nanometre scale gaps (nanogaps) between two different metals over large areas using the selective assembly of self-assembled monolayers over metals. The nanogap formed between the two metals can be used as a channel for coplanar electrodes in two terminal devices such as diodes and photodetectors. Figure 6.10 illustrates the fabrication process of a nanogap between gold and aluminium electrodes, which was optimised and carried out by Dr D. Georgiadou at Imperial College[205], London, and will be briefly summed up here. First, Al electrodes (M1) are patterned on a substrate (Si, Glass, PET…) via conventional UV lithography method (Figure 6.10a) onto which a self-assembled monolayer of octadecylphosphonic acid (ODPA) is grown by immersion in solution. The SAM functionalizes the first aluminium and the gold metal (M2) is deposited on top, so that Al-SAM-Au interfaces are formed (Figure 6.10c). An adhesive tape is then brought into contact with the Au layer and slowly pulled off. The Au areas in contact with the SAM are peeled off during this step due to the low surface adhesivity of the SAM, while the Au areas directly in contact with the substrate are not picked up (Figure 6.10d). After peeling-off, the device consists of lateral Al-SAM-Au structures and the Al and Au areas are then only separated by a short distance, corresponding to the chain length of the ODPA (10-20nm). Subsequent removal of the ODPA by

Acetone-IPA washing and UV-Ozone cleaning leads to the formation of the nanogap between the two metal electrodes (Figure 6.10e). The length of the gap mostly depends on the length of the SAM and can be tuned within the 15-40 nm range[202].

QD deposition

QD deposition and EDT ligand exchange was carried out in our laboratory at Oxford according to the process described in Section 6.2.1. Prior to deposition, the devices were rinsed with acetone and IPA and cleaned in a UV Ozone oven for 10 mins to ensure complete removal of the ODPA SAM.

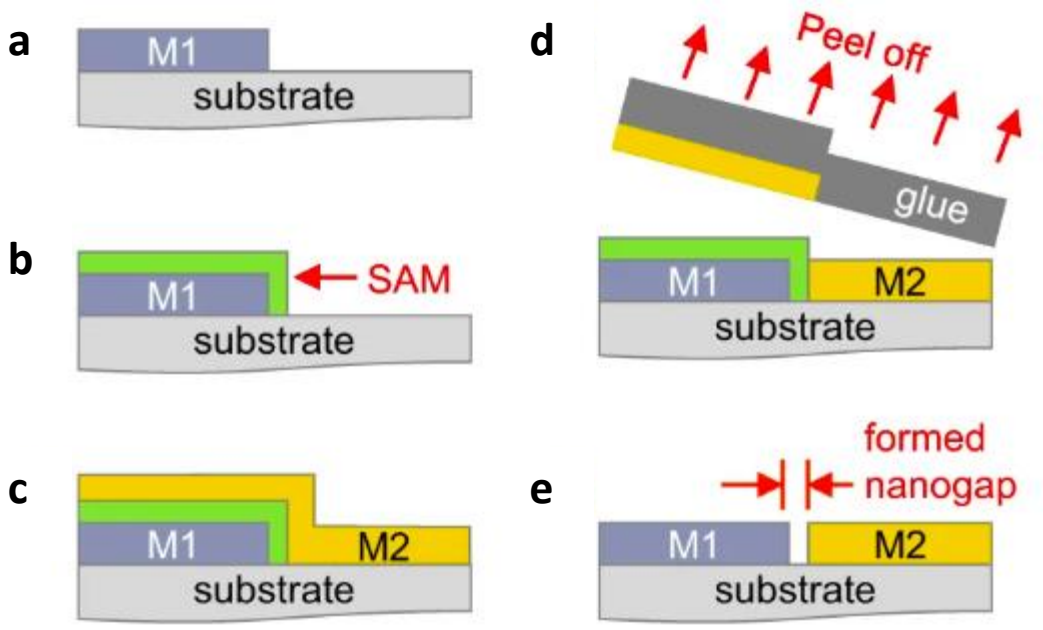

Figure 6.10. Illustration of the adhesion lithography technology. a) deposition and patterning of Aluminium electrodes (M1). b) functionalization of M1 with a self-assembled monolayer (SAM). c) deposition of the Au metal (M2). d) peel off M2 with an adhesive material. e) formation of nanogap after removal of the SAM by oxygen plasma treatment. From Ref [205], Copyright © 2018, Springer Nature.

6.3.3 Schottky diode characterisation

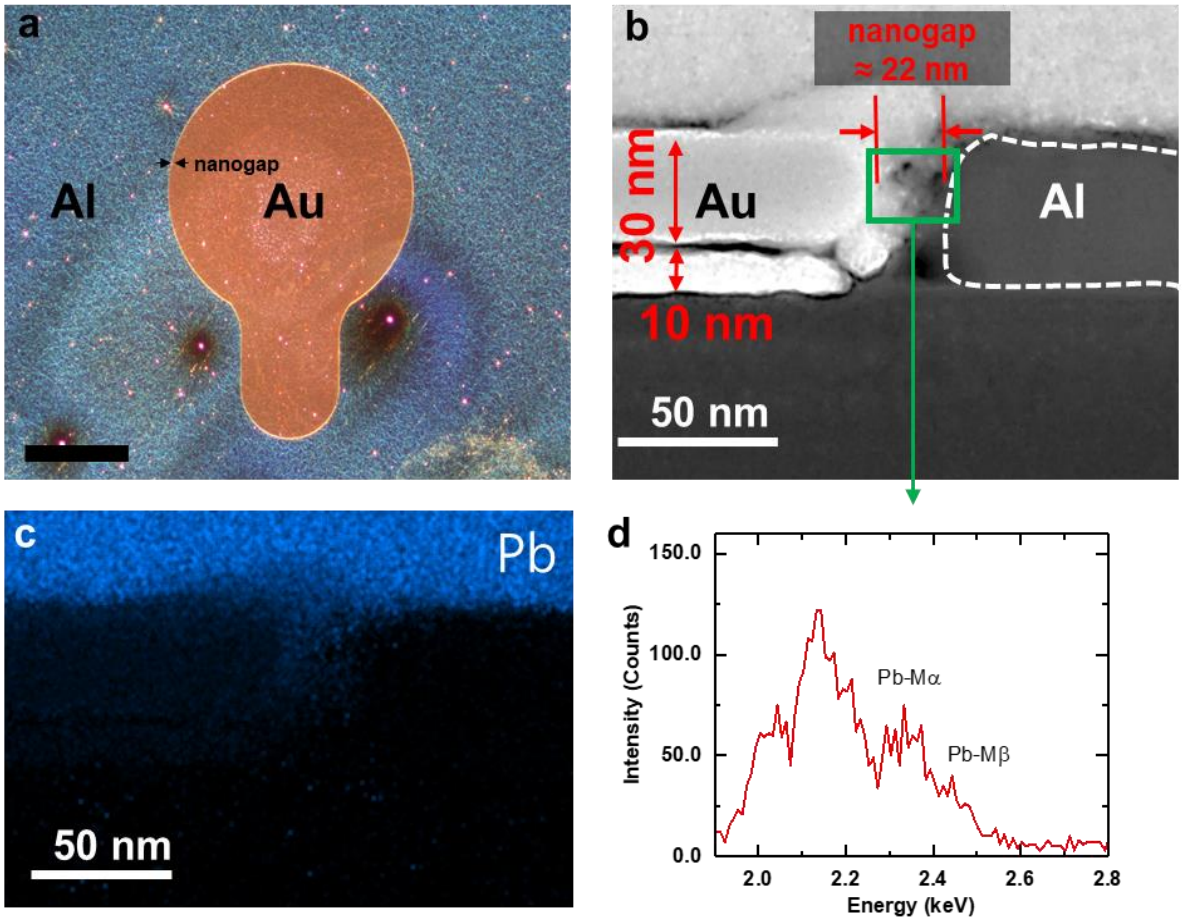

Figure 6.11. a) Dark field optical microscopy image of a device covered with one layer (30nm) of PbS QDs after EDT ligand exchange. Scale bar 100 μm. Device diameter 1 mm. b) Cross-sectional TEM image of a nanogap device covered by a monolayer of PbS QDs. The Au electrode consist of two stacked layers of 10 nm Al serving as adhesion layer and 30 nm-Au. PbS QDs can be seen filling the 22 nm gap. c) EDX mapping of Pb element shows that most of the QDs are located on top of the nanogap and bridge over it, but a few partially fill the gap. d) EDX of the area highlighted in green in (b) to confirm the presence of Pb inside the nanogap. TEM data was acquired by Dr A. Seitkhan at King Abdullah University of Science and Technology.

A dark field optical image of a 1 mm diameter device covered by a layer of PbS exchanged with EDT is shown in Figure 6.11a. The Al and Au areas are clearly separated by a well-defined bright line that is related to the presence of the nanogap. Short circuits could sometime be measured after device fabrication. It is however unclear if they arose from the device fabrication process itself or from surface scratches occurring either during storage or at the device cleaving stage. Cross-sectional TEM image

(Figure 6.11b) reveals a 22 nm long nanogap between an ~40nm high Au and Al electrodes. The Au electrode consists of 30 nm of Au stacked on top of 10 nm of Al. It is also shown that the PbS QD layer bridges over the nanogap and partially fills it. Elemental mapping using Energy Dispersive X-Ray spectroscopy (EDX) (Figure 6.11c) reveals the presence of Pb over the gap and as well as inside the gap. Moreover, the EDX spectral analysis of the area highlighted in Figure 6.11b confirms the presence of Pb inside the nanogap. It can then be inferred that most of the PbS QDs bridge over the nanogap,

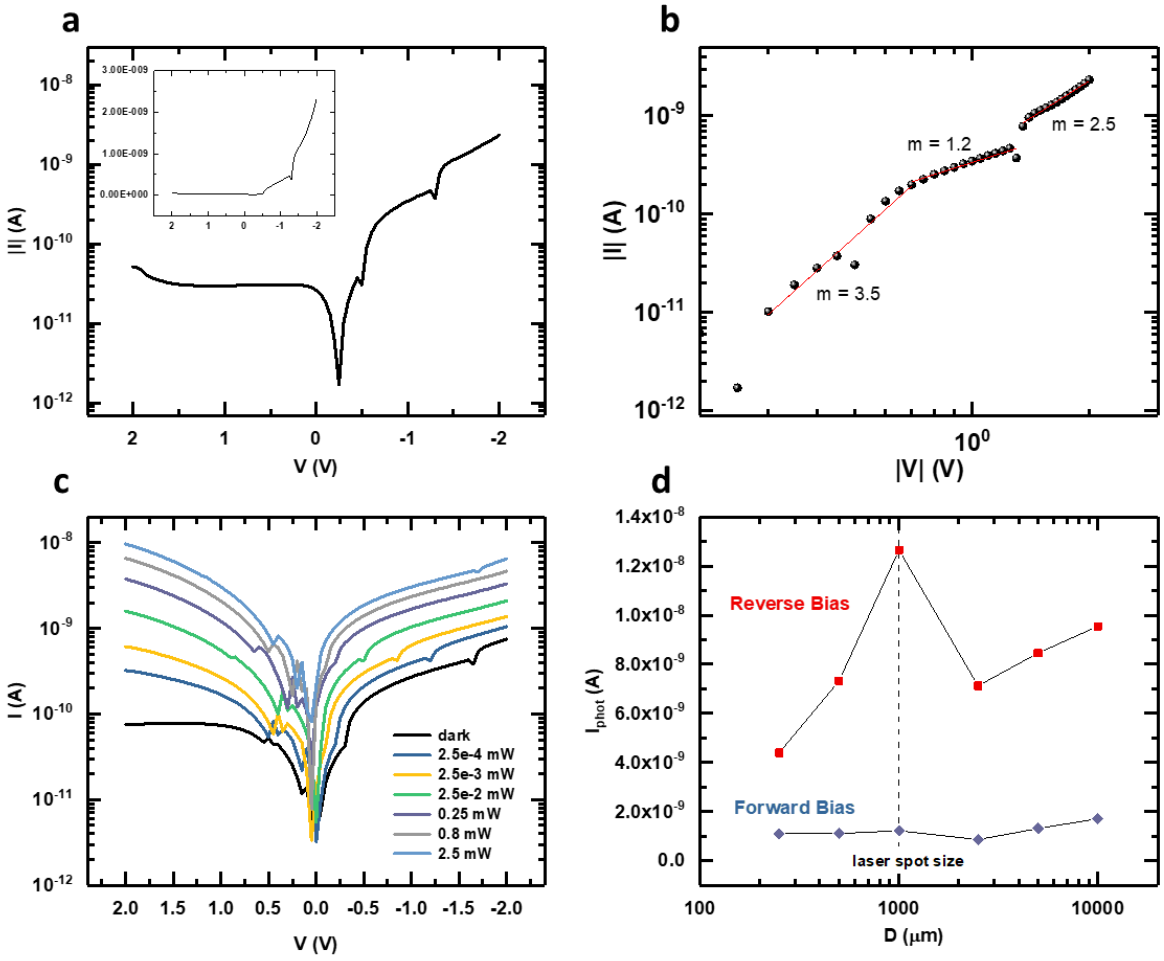

Figure 6.12. a) Semi-log I-V characteristic of a 1 mm diameter single layer PbS-EDT QDs diode obtained in dark conditions. Inset shows the I-V plot on a linear scale. According to the p-type Schottky contact and the electrical wiring shown in Figure 6.7b, a forward bias corresponds to negative voltages applied on the Al contact and reverse bias to positive voltages. b) Log-log plot of the forward current with associated fits of the form $I = V^m$. c) I-V characteristic of the photodiode at various incident light intensities. d) Photocurrent dependence on the device diameter for both forward and reverse bias.

and the presence of Pb in the nanogap suggests than some PbS QDs could be located within the gap as well.

Figure 6.12a shows the I-V characteristic of a 1 mm-long device over which 1 layer of EDT-exchanged PbS QDs were deposited. According to the schematic of Figure 6.8b, the Au electrode was grounded, and the voltage bias was applied to the Al electrode. The dark current exhibits an asymmetric behaviour with a low current (≈25 pA) when the diode is reverse biased (V>0) and a fast-increasing current in the forward bias (V<0), giving a rectification ratio of 10^2 and confirming the presence of a Schottky contact. The forward current was fitted on a log-log scale with a power law $I = V^m$ to identify the conduction mechanisms occurring in the diode (Figure 6.12b). Three different regimes could be decomposed, evolving from trap dominated conduction at low voltages (m=3.5) to a more linear dependence corresponding to thermionic emission (m=1.2) and space charge-limited conduction at higher bias voltages[206]. When illuminated by an 850 nm laser at various powers (Figure 6.12c), the diode showed a photo-response both in the forward and reverse bias configurations. This is an interesting phenomenon as photodiodes only typically show high photoresponse in reverse bias benefiting from the wide depletion region required to extract photo-charges. We offer here a tentative explanation for the observations. The current flowing through the diode under illumination can be expressed by the familiar photo-current formula,

$$I = I_0\left(e^{\frac{qV}{kT}} - 1\right) - I_{phot}, \tag{6.2}$$

where I_0 is the saturation current and V is the applied bias. The photocurrent I_{phot} is determined by[207]

$$I_{phot} = qSG(L_e + W + L_h) \tag{6.3}$$

where L_e and L_h are the diffusion lengths of the electron and holes, respectively, W is the length of the depletion region, G represents the photocharge generation rate and S is the device cross-section

The size of the depletion region, W, changes with the diode bias, increasing in reverse bias and decreasing for forward bias. In conventional diode designs, the size of the depletion region is strongly reduced in forward bias and no measurable photocurrent can be detected. With a nanogap channel, the diode is expected to become fully depleted easily even with a reduced depletion region. Thus, when operating in forward bias, the size of the depletion region is reduced but is still large enough to extract photogenerated charges, especially when considering that the diffusion length of the PbS QDs[118] (80 nm) is much larger than the dimension of the nanogap.

An advantage of the adhesion lithography fabrication technique lies in the fact that it allows the fabrication of devices with large aspect ratios, with nanometre wide channel length but widths ranging up to the centimetre scale. For instance, Figure 6.12d shows the impact on the I-V plot of the scaling

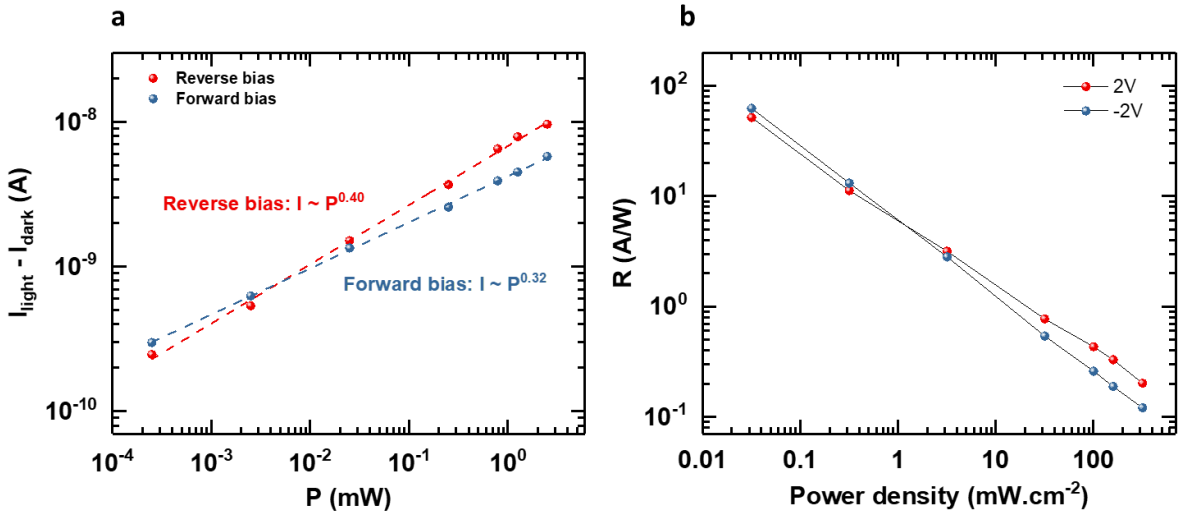

Figure 6.13. a) Photocurrent as a function of the laser output power. Different linearities are measured depending on the bias regime, with the diode exhibiting superior response (higher linearity) in reverse bias. Forward bias was -2V and reverse bias was 2V. b) Responsivity *R* is calculated from a). Spot size was 1 μm.

of the electrode width ranging from 250 μm to 1 cm. The current scales with the width due to a larger device cross-section, defined as the product of the device perimeter and the thickness of the QD layer. The associated photocurrent is plotted in Figure 6.12d for forward and reverse bias modes. The photocurrent increases with the electrode width when the diode is reverse biased but remains constant

for forward bias. A drop in the current is observed when the width reaches 1000 μm, which roughly corresponds to the laser spot size. Beyond that point, the light current saturates but not the dark current, hence the photocurrent decreases.

The I(P) response is plotted on a log-log scale in Figure 6.13a and fitted for both the forward and reverse bias with a power law dependence, $I_{phot} = P^{\alpha}$. In both cases, sublinear behaviour was observed, with $\alpha = 0.32$ and $\alpha = 0.40$ in the forward and reverse biases, respectively. Superior photoresponse, as indicated by the higher α coefficient, was observed in the reverse bias configuration, which is expected for a photodiode. The sublinear response, with the exponent α deviating for the ideal case of $\alpha = 1$ is reminiscent of our work on PbS QDs photodetectors presented in Section 6.2 and is attributed to bimolecular recombination and loss of photo-excited carriers due to trapping[196].

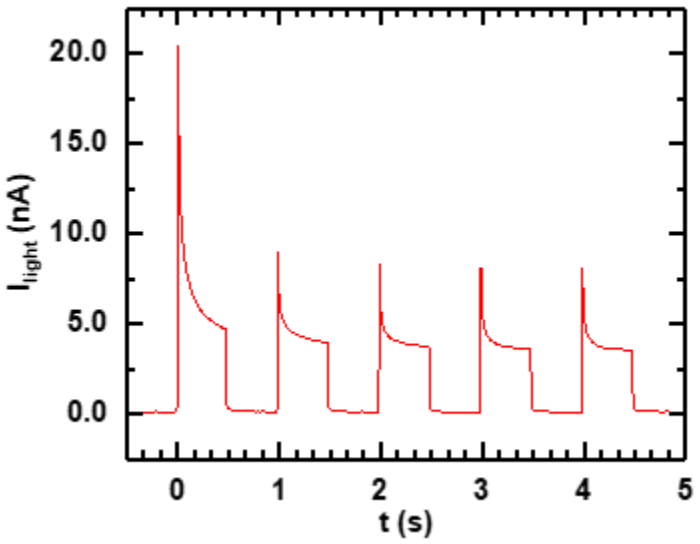

Figure 6.14. Transient response of a 1 mm width Schottky photodiode covered by a monolayer of PbS QDs. Modulation frequency was 1 Hz and bias voltage 1 V (reverse bias).

The responsivity has been calculated at different light intensities according to Equation 2.11. The device active area was calculated by taking the product of the nanogap width, estimated to be 20 nm, by the device perimeter (1 mm). Figure 6.13b shows the responsivity of the device measured in Figure

6.12c, with the best values of 38.7A/W and 46.9A/W obtained for the reverse and forward bias, respectively, along with associated detectivities of 3.5×10^{12} Jones and 1.53×10^{12} Jones. These high values indicates a top-of-the-range performance of the nanogap photodiode (Chapter 2, Table 2.2) which is the consequence of the low dimensional nature of the nanogap device[203] combined with the low dark current of the Schottky diode.

Next, we considered the transient response of the photodiode to an incident laser impulse. Figure 6.14 shows the time evolution of a 1 mm PbS EDT diode reverse biased at 1V and illuminated with an 850nm, 320mW.cm^{-2} laser diode switched at 1 Hz. A spike in the photo-response is observed before returning to a steady-state, which we attribute to charge trapping and bimolecular recombination occurring at high excitation intensities. The high density of photogenerated carriers and the presence of trapping centres promote a high recombination rate which induces a decrease in photocurrent. This effect is intensified by the fast transit time of the photodiode, which competes with the slow filling of the traps, since more photocarriers can be extracted before recombining into traps. The rise and fall times were extracted by measuring the time taken by the device to transit from 10% to 90% of its steady state value and found to be 1.9 ms and 8.5 ms, respectively, which correspond to a bandwidth of 180 Hz. These values are significantly faster than that of the photoconductors studied in Section 6.2.3, thanks to the fast transit time of the carrier trough the nanogap channel. It should, however, be noted that these two experiments were not done simultaneously and used different batches of PbS QDs, which can possibly alter this interpretation. Furthermore, the millisecond order of magnitude suggest that the temporal response is not only limited by the transit time but also by the longer photogenerated carrier recombination time. This is in line with the presence of trap sates in the QD films as discussed in Section 6.2.3 which act as recombination or sensitizing centres. Since the film deposition and passivation techniques used were the same for photoconductors and the photodiodes, it is reasonable to assume that these traps are also present here and limit the device performances.

6.3.4 Concluding remarks

In summary, IR photodiodes were fabricated using PbS QDs as the photoactive material deposited on a nanogap that separated coplanar Au/Al electrodes. These were enabled by adhesion lithography, which allowed fabrication of devices with an arbitrarily large aspect ratio. The devices were made by a simple coating of solution-processed QDs as optimized in Section 6.2. The QD layer was electrically activated with an EDT treatment which was thought to promote adhesion to the gold contacts and to present favorable energy band alignment for the creation of a Schottky barrier at the aluminium contact. TEM cross sectional spectroscopy and EDX elemental analysis showed that the PbS bridged and partially filled the nanogap formed between the Au and Al electrode. In the dark, the device showed a clear diode like behavior suggesting the presence of a built-in potential due to the Schottky contact at the PbS/Al interface. Under IR light, the devices showed a responsivity of R = 38.7A/W in reverse bias combined with a detectivity of 3.5×10^{12} and a bandwidth of 180 Hz. The bandwidth was shown to be faster than that of simple PbS photocondcutors (15Hz, Section 6.2.3), as expected for a photodiode. Even though an improvement was observed, the response time was still of the order of a few milliseconds, and the presence of long recombination centres due to traps is thought to limit the response time. These results highlight the compatibility of colloidal PbS QDs with adhesion lithography fabrication processes and enables the development of IR detectors for next generation of flexible and transparent electronics.

7 PATTERNED 1D PBS QDS PHOTODETECTORS VIA TRANSFER PRINTING

7.1 Concept

In the previous chapter, the integration of PbS QDs in photodetectors using conventional fabrication methods and innovative device structure was discussed. The deposition of thin QD films was obtained via spin-coating which, together with doctor blading and drop casting, has been the main layer by layer deposition method for QDs [16], [73], [191], [208]. These methods integrate smoothly with colloidal semiconductors, operate a room temperature and are easily tunable. As such they have been considered for integration of QDs on plastic substrates has been considered for the next generation of flexible and transparent electronics[17].

In order to be present a viable solution for device manufacturing, CQDs must be compatible with large wafer scale integration, which involves the patterning of thin film layers on a substrate wafer. The aforementioned techniques result in the deposition of continuously homogeneous, non-patterned layers and require post deposition patterning usually involving a combination of lithography and etching processes[209], [210]. These extra processing steps expose the materials to numerous solvents and annealing temperatures which promotes cross contamination and material degradation due to oxidation. As such the throughput is limited and the performance yield is unduly affected.

On the other hand, microcontact printing, or transfer printing, is based on a pick and print approach, where the materials primarily deposited on a source substrate are picked with a polymer stamp and printed with high precision onto the target area[211], [212]. The stamps, usually made from PDMS, can be patterned prior to the picking up step, which allows for the solvent free deposition of patterned materials on the target substrates. This fabrication technique has been explored for cadmium based quantum dots (QDs) LEDs, where the red, blue and green QD layers were successively printed on the target substrates to form pixels[129], [135], [213].

Aside from cadmium QDs, lead based quantum dots such as lead sulphide (PbS) QDs have gained a lot of attention thanks to their widely tunable bandgap and facile preparation technique, with potential applications in energy harvesting and infrared photodetection[11], [13], [78], [191], [193]. Recently, Mahmoud *et al* have reported the demonstration of photodetectors via the transfer printing of lead sulphide (PbS) QDs layers onto interdigitated electrodes[136]. It was the first reported realisation of PbS QDs based devices via micro-contact printing. The dimensions of the micropatterned QDs were, however, rather large with a QD mesa width of around 50μm. In this Chapter, this approach is developed further by printing arrays of micro scale PbS QDs patterns on both solid and flexible substrates. Arrayed lines of PbS QDs are successfully transferred onto the substrates, with a minimal linewidth of 2.5μm. An optimisation route is also explored by successfully stacking nanometre thin QDs layers on top of each other via alignment techniques borrowed from conventional UV lithography process. If the devices showed low light responsivity, which was attributed to the ultra-thin photoactive layers, it was also showed that they could match the time response performances of spin coated QD photoconductors having transient rise and fall times of respectively 29ms and 44ms in line with what we obtained in Chapter 6.

7.2 Stamp fabrication and printing optimization

7.2.1 Stamp design

The subtractive transfer approach employed in this chapter is summarised in Figure 7.1. Micro patterned stamps are brought in contact with the donor substrates onto which PbS QDs were initially deposited via spin coating (Figure 7.1a-b). Fast removal of the stamp then delaminates the QDs for the donors and inks the stamp patterned areas (Figure 7.1c). The inked stamps are subsequently pressed onto the target substrates and slowly pulled up, which then releases the QDs from the stamp

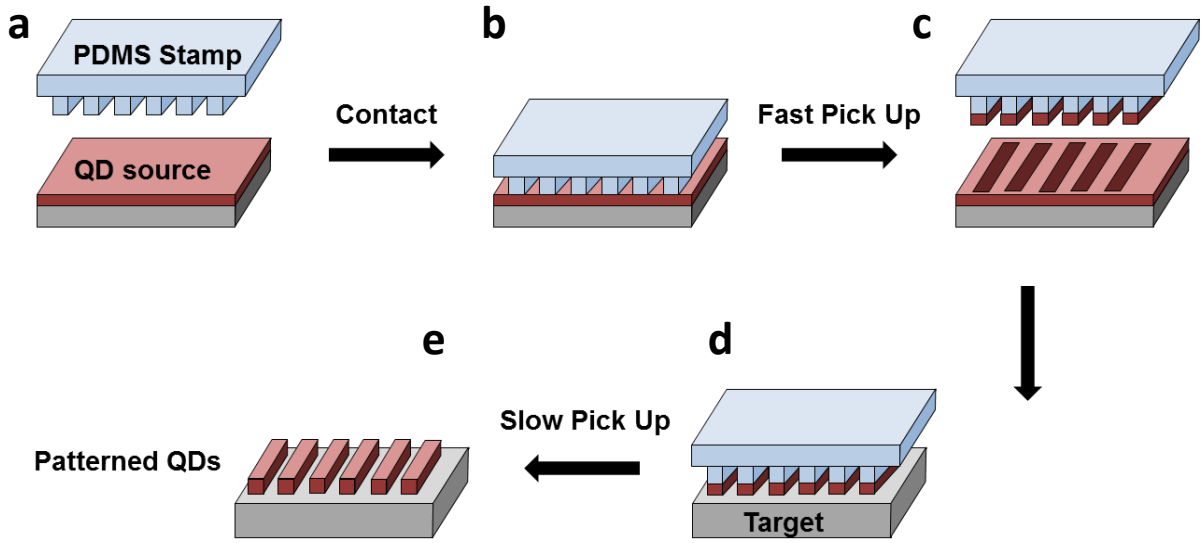

Figure 7.1 . Transfer printing of patterned QDs arrays. a) Stamp patterning and QD source substrate preparation. b) pick-up and c) inking of the QD layer on the stamp. d-e) slow printing of the QD patterns on the target area.

(Figure 7.1d) and prints them onto the target substrate (Figure 7.1e). By controlling the speed at which the stamp is removed from the substrate, one can ensure that the QD layer can be effectively printed onto materials with different surface energies and thus onto various types of substrates.

A key challenge in this process lies in the reliable fabrication of elastomeric stamps whose patterning and aspect ratios must be controlled during the design process. Indeed, there is a risk that the stamp can collapse under strain resulting in inaccurate printing of the QDs. The collapse of the stamp corresponds to the moment where the stamp recess areas (called the roof), encounter the surface of the substrate. A schematic of a patterned stamp with protruding and recessed lines is presented in Figure 7.2a. The critical dimensions are labelled as H the height of the patterns, W the pattern linewidth, and D the interline spacing. The collapse of a stamp with $H = 10$ µm, $D = 15$ µm, $W = 5$ µm parameters was modelled in COMSOL and is shown in Figure 7.2b. As the applied pressure

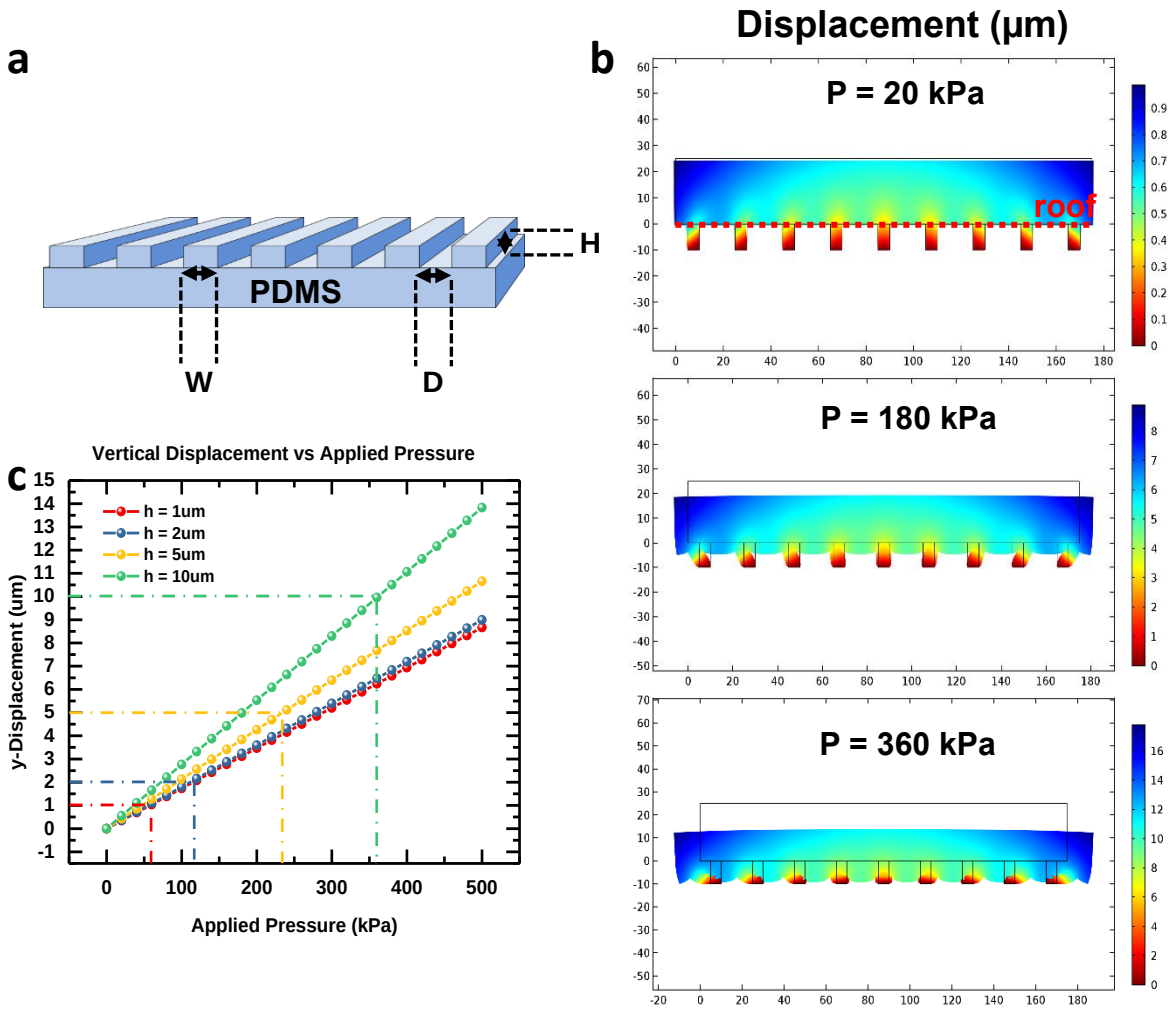

Figure 7.2. Patterned microstamp design. a) Schematic of the stamp with design parameters as described in the text. b) COMSOL modelling of the roof collapse as a function of the applied pressure P. c) Roof vertical displacement as a function of the applied pressure for different stamp heights (1μm, 2μm, 5μm, 10μm).

increases, the vertical displacement from the roof increases as well until collapse on the substrate (P = 360kPa). The critical pressure is defined as the pressure at which the vertical displacement from the roof reaches the value of the stamp height *H*. The plot in Figure 7.2c shows the vertical displacement as a function of the applied pressure for several stamp heights. For $H = 2$ μm, the calculated critical pressure was found to be 120kPa, which for a stamp area of 0.5cm^2 corresponds to an applied static force of 0.6kg; slightly higher than the pick-up load value for which our transfer printing process was optimized (0.5kg). Qin *et al* have written an extensive paper detailing the protocol that should be

followed regarding the fabrication of structured stamps. Therein, they recommend that the optimal aspect ratios fall within the range of $0.5 < \frac{H}{W} < 5$ and $\frac{H}{D} > 0.05$ [214].

7.2.2 Stamp fabrication

Masters for the moulding of the PDMS stamp were fabricated by photolithography of commercially available epoxy (SU8 2002 and SU8 2010) of various thicknesses to provide different aspect ratios. The photoresist was spun cast on 4" silicon wafers which were cleaved into 2×2 cm^2 squares after the lithography step. The developed photoresist was then hard baked at 150ºC for 15 mins to improve the chemical stability of the master and remove the cracks that appeared during the UV exposure and subsequent development process. A self-assembled monolayer (SAM) of octadecyltrichlorosilane (ODTS) was grown on each SU8 master to modify the surface properties from hydrophilic to hydrophobic to prevent the cured PDMS from sticking to the master during removal from the mould. A 10:1 mixture of PDMS to curing agent was poured over each SU8 master placed in a petri dish. After pouring, the total thickness of the PDMS was found to be 0.5 cm. The samples were then left to degas for 1hr in a desiccator to remove the air bubbles that appeared during mixing and pouring of the PDMS. PDMS was subsequently cured for 2hr at 60ºC with the implementation of a temperature ramp. The temperature ramp from ambient room temperature to 60ºC was necessary to leave enough time for the viscous PDMS to relax before curing in order to obtain substrates that were as flat as possible. To ensure complete drying of the PDMS, the stamps were left for at least 12hr in ambient conditions before peeling them off the SU8 masters. The SU8 masters could be reused several times for stamp fabrication and were only limited by particle contamination that occurred during storage. The characterisation of the stamps made from an SU8-2002 master is shown in Figure 7.3. AFM imaging reveals that the stamps have a flat surface with a height H of about 2 μm, which is consistent with the use of a SU8 2002 photoresist (Figure 7.3a). Furthermore, after removal of the stamps, the patterned features maintained a high quality and consistency over a large scale, as shown by in SEM

images of an array of lines with a L/W ratio of 50:5 (Figure 7.3b). The critical feature length only depends on the limits of conventional lithography, provided that an appropriate stamp height is chosen to avoid stamp collapse.

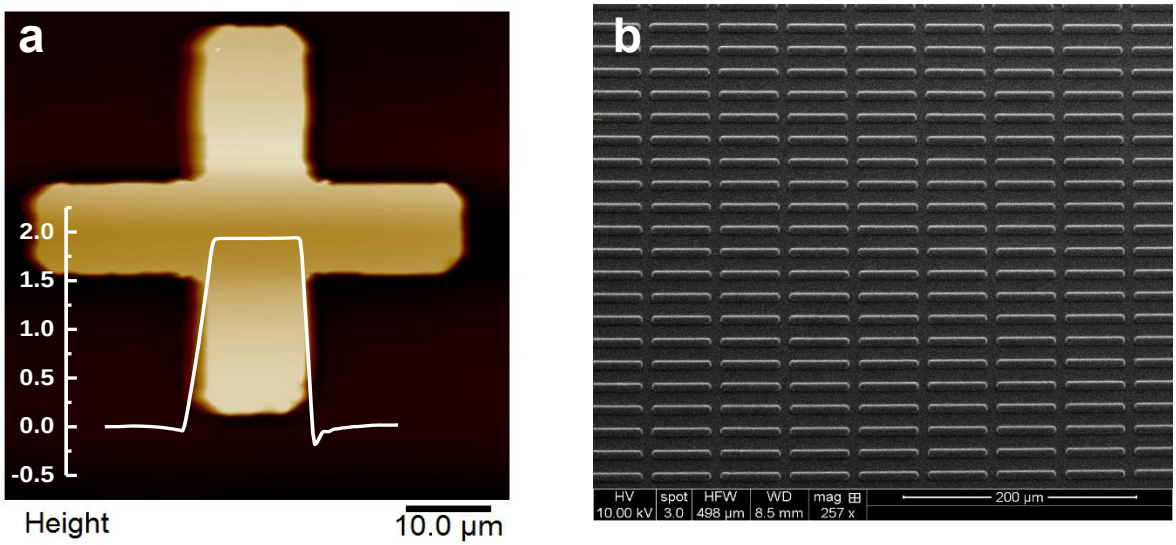

Figure 7.3. Stamp characterisation. a) AFM of a stamp representing a pattern alignment cross. Step profile measures a height of $H = 2\mu m$. b) SEM image of PDMS arrays of lines, H/W was 2:5 and H/D was 2:15. Each line length was 50 µm.

7.2.3 Printing of arrays of PbS QDs

Source Substrate Preparation

We now turn to the pickup and transfer of PbS quantum dots with the patterned stamps. The source substrate was made by spin coating a layer of PbS QDs onto a 1×1 cm^2 silicon (Si) wafer onto which a SAM of ODTS was grown beforehand. The ODTS silane precursor bonds with the silanol groups present at the Si surface results in the formation of highly ordered molecules perpendicular to the substrate. This reduces the surface energy of the silicon and helps to encourage the delamination of the QDs from the source substrate. The Si substrates were previously cleaned with an O2 plasma exposure (5mins, 100w) to remove the organic groups and promote a better SAM coverage. The SAM

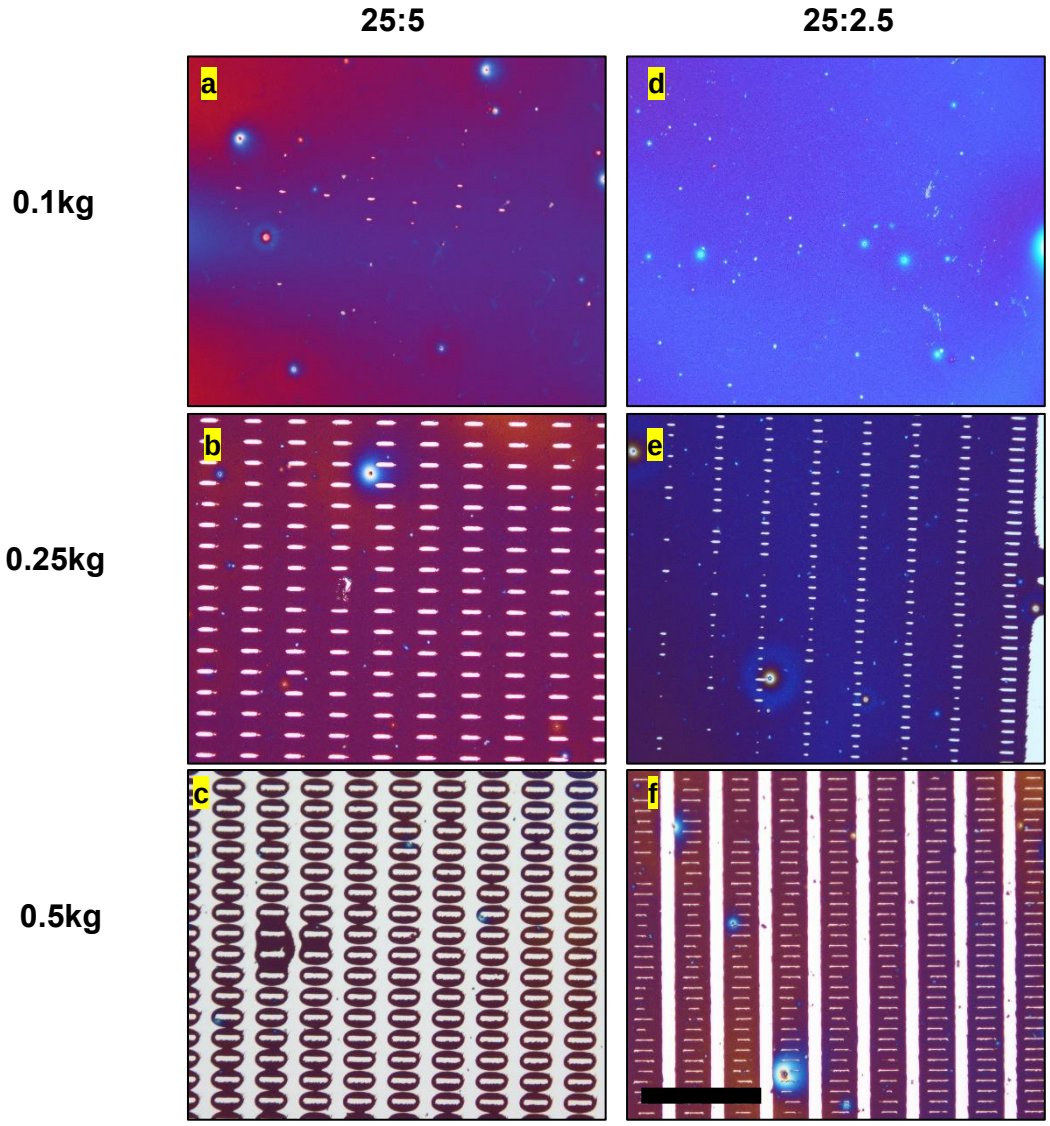

Figure 7.4. Optimisation of the pick-up (delamination process). Optical microscope images of the QD source substrates after stamp removal. Purple and blue areas correspond to areas where QDs are present, while bright areas correspond to areas where they have been removed and inked on the stamp. a-c) Line length 25μm, linewidth 5μm. d-f) Length 25μm, linewidth 2.5μm. For all images: scale bar 100μm.

deposition conditions were derived from the methods described in Ref. [135] and processed as follows. In an argon filled glovebox, Si substrates were placed in glass petri dishes filled with anhydrous hexane. 100 μL of ODTS were poured into the petri dish and the samples were left to react for 20 mins. The substrates were then thoroughly rinsed with hexane and sonicated to remove ODTS residues. The samples were gently dried with compressed air and the deposition of PbS QDs was performed

immediately afterwards. One layer (drop) of PbS QDs was spin cast on the source substrate at 3000 rpm for 30s.

Pick-up optimization

Several stamps consisting of arrays of lines of 2 μm height with various W/L ratios were made to identify the optimum peel off pressure. Figure 7.4 shows optical microscope images of the source substrates after having been brought into contact with the stamps at different loads (0.1kg, 0.25kg and 0.5kg) for 30 s and quickly pulled up. The images can be seen as a 'negative' of the pattern where the dark areas are the part of the QD film that have not been picked up and the bright areas correspond to the QDs that have been inked on the stamp. The peel off was performed by quickly detaching the stamps from the source substrates (0.5 $cm \cdot s^{-1}$). At low applied loads, there is no pickup, independent of the ratio, which suggests that the applied pressure is below the critical pressure required to delaminate the QDs from the source substrate (Figure 7.4 a, d).

Pick up begins to be observed at larger applied force (0.25kg, Figure 7.4 b, e), however the lines appear as poorly defined especially for the higher aspect ratios (25:2.5) which suggests that there is a minimal linewidth necessary to achieve pick-up. As a rule of thumb, the higher the applied pressure during the delamination step, the better defined the features. However, applying excessive pressure will cause 'over picking' of the QDs. Over picking is due to the partial collapse of the stamp as some recessed areas are brought into contact with the source and picked up together with the raised features (Figure 7.4d, f). If the desired pattern will indeed be picked up, other unwanted areas are inked on the stamp as well and could potentially be transferred to the target during the printing step.

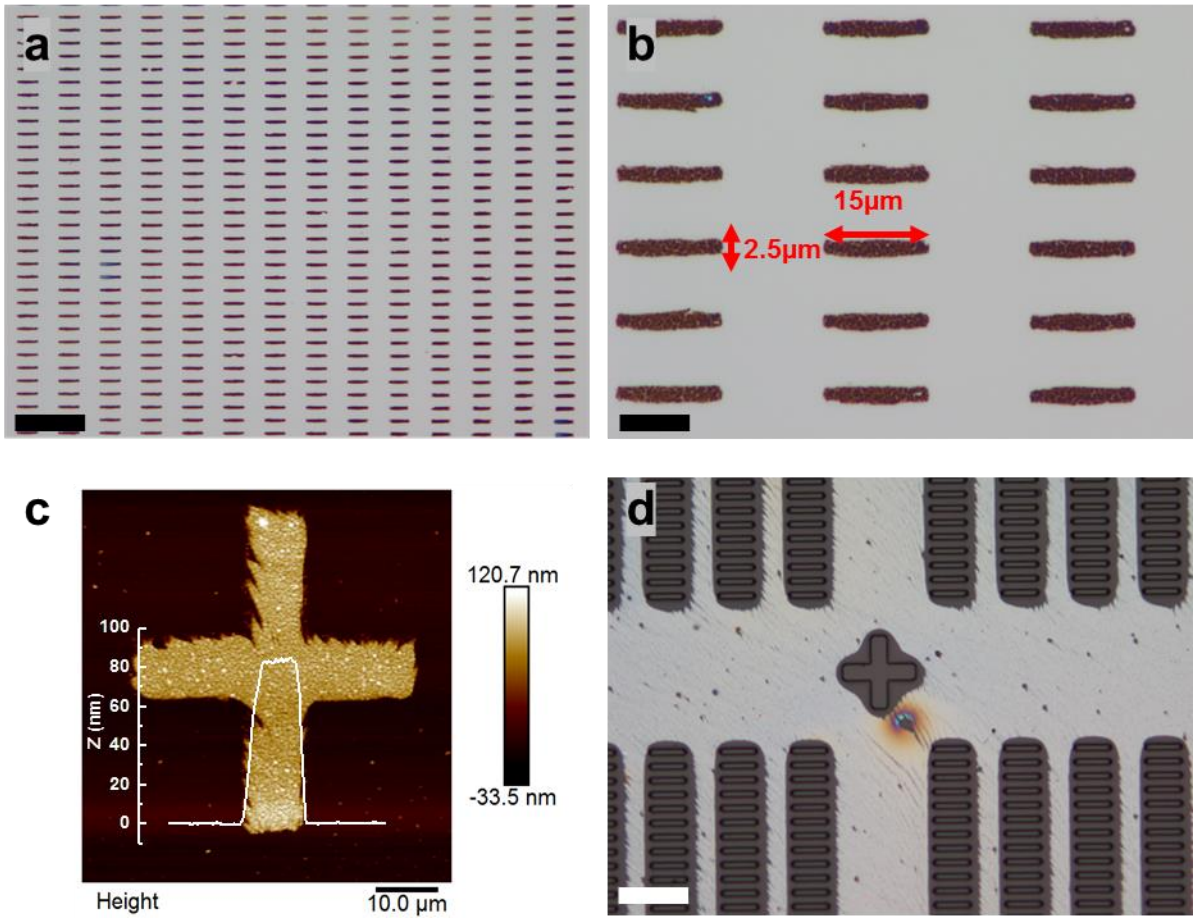

Figure 7.5. Characterisation of printed QD arrays. Optical microscope image of 15:2.5 lines of printed PbS QDs. a) Scale bar 50 µm. b) Scale bar 10 µm. c) AFM of a cross of printed PbS QDs in accordance with the stamp shown in Figure 7.3a. Step height of the QDs was 80 nm. d) Image of a stamp after printing. Dark areas correspond to the raised parts (25:2.5 lines and alignment cross) where no QDs can be seen. Bright areas in the recessed parts correspond to the leftover QDs that did not transfer.

Array printing

Once the stamps have been inked, they are brought into contact with the target substrate to print the patterned QDs. The targets can be exposed to O2 plasma treatment before printing to lower their surface energy and promote adhesion of the QDs, although this is not a critical step. So far, we have printed QDs on various substrates such as silicon and silicon dioxide, glass and polyethylene terephthalate (PET). Optical images of printed array lines of PbS QDs (15:2.5 L/W ratio) show that the lines are reproduced with high fidelity at a relatively large scale (Figure 7.5) and are well defined (Figure 7.5b). AFM of a printed alignment feature (cross) indicates a thickness of 80 nm before ligand

exchange (Figure 7.5c). The printing pressures were found to be much lower than that required for pick-up as the necessary condition to release the QDs from the elastomeric stamps lies in the slow removal of the stamp from the substrates rather than the applied pressure[211].

The speed at which the stamps were released from the target substrates was kept constant and equal to 0.2 $mm \cdot s^{-1}$. We observed successful printing for applied loads as low as 0.01kg. A great advantage of this low-pressure transfer is that the risk of the stamp collapsing during printing is largely reduced (Figure 7.2b). As such, QDs that may have inked the recessed areas of the stamps due to over picking are then not transferred. The optical microscope image of a stamp after printing at 0.1kg is shown in Figure 7.5d. The observed raised areas present on the stamp are 25:5 μm lines and an alignment cross. All the features are dark coloured meaning that the QDs that previously inked those parts of the stamp have been successfully printed onto the target. On the other hand, the recessed areas exhibit a bright contrast indicating the presence of a leftover QD film. This indicates that the recessed parts that have been inked during the pick-up step due to over picking will not be transferred to the target due to the low applied pressure, which prevents the stamp collapsing.

7.3 Printed 1D arrays of PbS QDs photodetectors

7.3.1 Fabrication

Arrays of PbS QDs were printed on top of contact Au electrodes as illustrated in Figure 7.6a. The electrodes were thermally evaporated with a shadow mask and were separated by a gap of 20 ± 10 μm. The $L/W/D$ stamp parameters were 100/5/15. The length of the patterned lines was kept long enough to allow manual alignment with the prepatterned contact with the help of the transfer printer camera. The total device channel consisted of 50 lines of 5 μm width, bridging the 1 mm electrodes. The optical image of a printed device in Figure 7.6b reveals that the QD lines successfully printed over the electrodes with a large enough area covering the gold contacts to ensure good electrical contact.

As detailed in Chapter 6, PbS QDs must undergo a ligand exchange process to improve the conductivity of the film. Interestingly, no pickup could be achieved when the PbS QDs were treated with either TBAI or EDT after deposition on the source substrate, because of the higher surface energy of the film which is a consequence of the closer interparticle distance occurring after the ligand exchange.

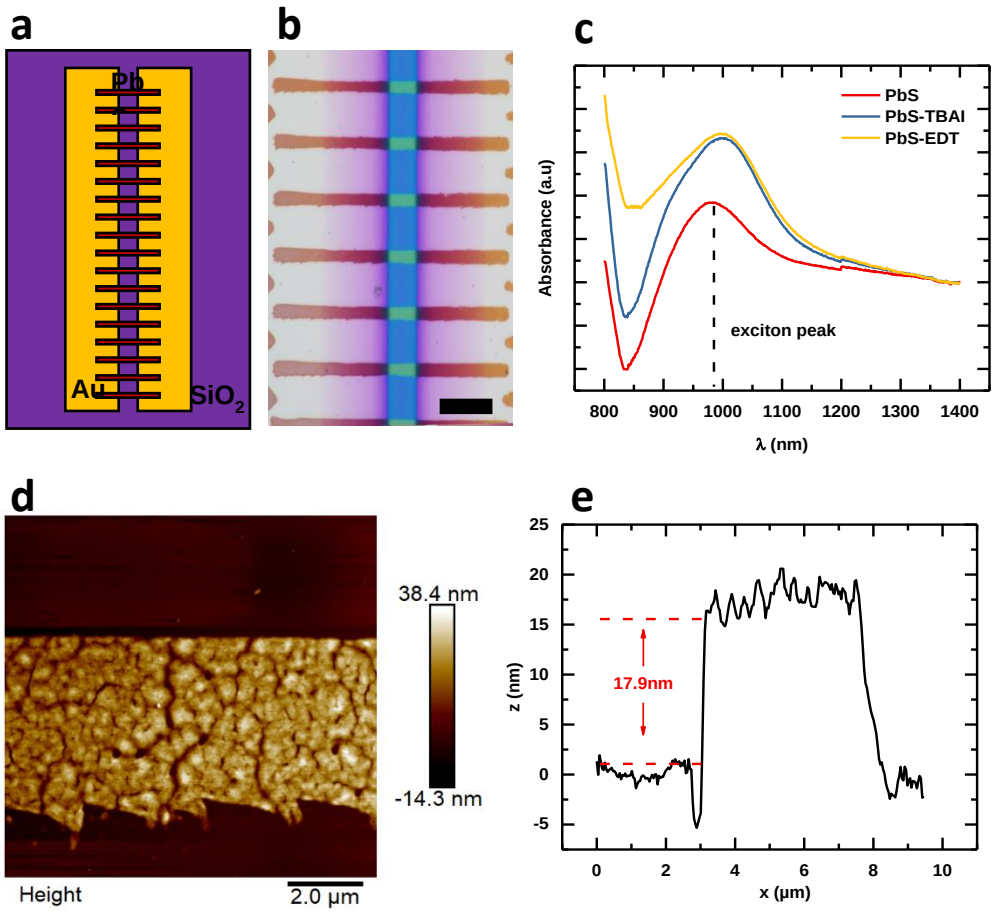

Figure 7.6. Characterisation of micro-patterned PbS QDs printed on gold electrodes. a) Schematic and b) optical microscope image of a transfer printed device. Line length was 100 μm and width 5 μm. Scale bar 20 μm. c) Absorption spectra of transfer printed PbS QDs before (red line) and after ligand exchange. Ligands were TBAI (blue) and EDT (yellow). d) AFM image of a printed line after TBAI exchange and the e) the corresponding step profile.

To bypass this issue, the ligand exchange step was performed after the printing of the layer on the source substrate. The ligand exchange can also be done on the stamp after having been inked by the QDs, but prior to printing on the target substrate. This is in order to keep the processes on the target

substrate completely solvent free. To ensure that the properties of the QDs were maintained after the transfer printing process, we printed non patterned layers of QDs onto a glass substrate for UV-Vis characterization. Figure 7.6c shows that after printing the exciton peak is still visible with either no ligand exchange, TBAI exchange, or EDT exchange. A red shift of about 50nm exists for the ligand exchanged film but the exciton peak is still visible which indicates that quantum confinement is maintained and that the QDs did not merge into an amorphous film during the printing process. Following the optimization work discussed in the previous paragraph, all of the lines were then printed with consistent widths and were of a high quality, which demonstrates the robustness of the transfer printing approach and its potential for scalability.

An AFM image in Figure 7.6d presents the structural profile of the printed lines after TBAI ligand exchange. One side of the line is clearly defined with a straight edge, while the other side (bottom) shows some irregularities. These irregularities could be due either to the imperfect flatness of the stamp or to an imperfect parallelism between the stamp and the substrate holders, which in either case induces an uneven removal of the stamp during the delamination phase and tears the QD film instead of cleanly picking it up. We tend to favour the latter reasoning since the AFM of the patterned stamps showed that they were reasonably flat (Figure 7.3a). The step height measurement across the line revealed a thickness of 18 nm after TBAI ligand exchange (Figure 7.6e) in accordance with the QD film thickness reduction occurring with the exchange step (Chapter 6, Section 6.2.2).

7.3.2 Photoconductor Characterization

Typical current-voltage characteristics of a single layered printed device consisting of 50 lines of width 5 μm is shown in Figure 7.7. A control device made from a plain non-patterned printed single layer is also shown. In both cases, the devices underwent 30s of TBAI ligand exchange before electrical measurements were carried out to improve the conductivity. The linear trend at low biases indicates good ohmic contacts even for thin QD films (17.9 nm, Figure 7.6e) which confirms that transfer printing can be used for the deposition of high quality conducting QDs. The two-probe conductivity in the dark was derived to be 10.6 pS in the patterned device compared to 244.5 pS for the control case. When normalised to device cross-section, this translates to a cross-sectional conductivity density of 13.7 $S \cdot m^{-2}$ for the control device compared to 2.39 $S \cdot m^{-2}$ for the patterned device.

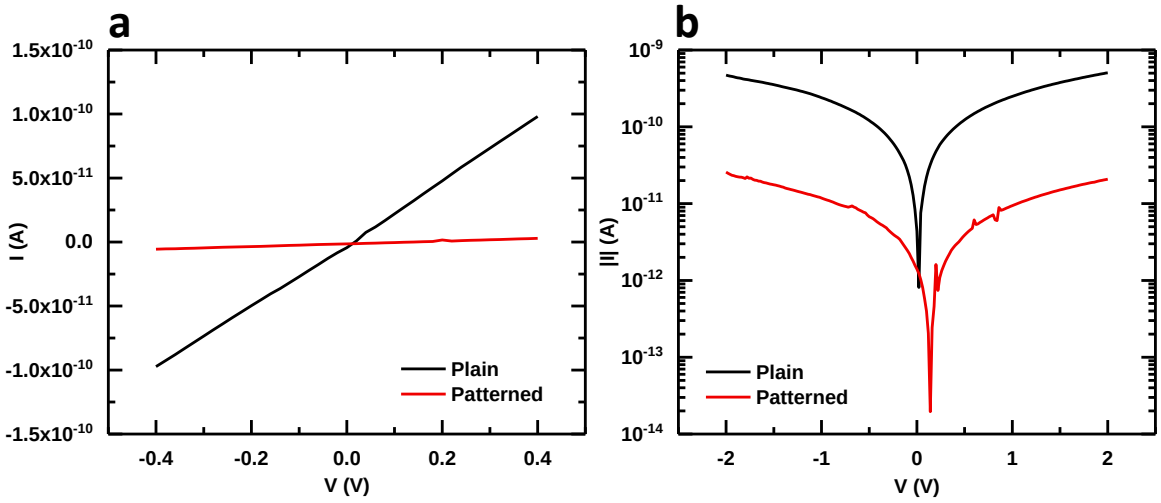

Figure 7.7. Dark current under bias of a 50×5 μm lines PbS QDs device (red) and a plain, non-patterned device (black) on a) linear scale and b) log scale. The QD layers were exchanged with TBAI.

EDT ligand exchange was also tested, but the measured dark current levels of the patterned devices were too low to ensure consistent results. However, the EDT control printed devices with no patterning showed electrical response that were similar to that of spin coated EDT devices (Figure 7.8a). Figure 7.8b displays the AFM image of treated printed lines with the EDT ligand and no significant difference in roughness can be observed from the TBAI treated case (Figure 7.6d). From

this information, we infer that no major morphological differences exist between the transfer printed EDT and TBAI lines and that TBAI and EDT treated QD films are, therefore, subject to different transport mechanisms.

Zhang *et al* reported the existence of percolation pathways in EDT treated QD films, where charges randomly hop from one QD to another and transport occurs where a path from one contact to another has been formed[198]. With such a hypothesis, transport would be highly localized and dependent on the area of the QD film in contact with the electrodes. In our device configuration, such an area is reduced and therefore transport is less likely to occur. TBAI treated devices, however, showed conduction independently of the topology of the QD film (plain or patterned), which suggests that percolation pathways are more likely to occur making the device less dependent on contact area between the electrodes and the QD film.

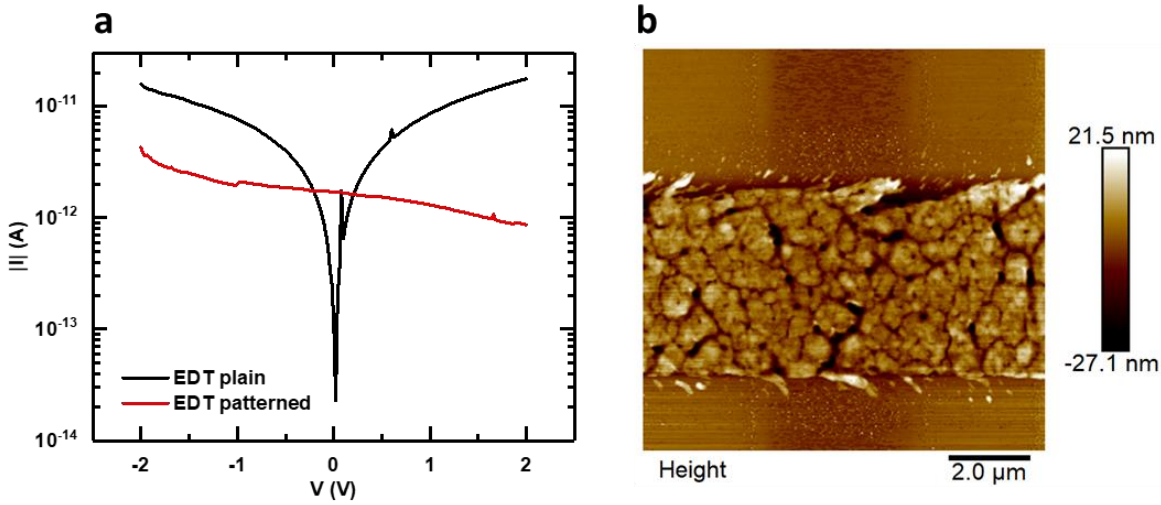

Figure 7.8. Electrical performances of EDT treated devices. a) I-V curves of (red) printed lines and (black) plain QD film (log scale). b) AFM image of an EDT treated printed line

7.3.3 Photoresponse

The devices were illuminated by an IR laser source and the measured photocurrent is plotted on Figure 7.9a. The light source was a 2.5mW 850 nm IR laser, with a spot size of approximately 1 mm. The active area consisted of 50 lines of length 20 µm and width 5 µm for the tested devices and 1 mm × 30µm for the control samples. According to Figure 7.9a, both the control and the patterned device

show an increase in conductivity under illumination, whereby the control device exhibit larger photocurrent because of its larger effective area.

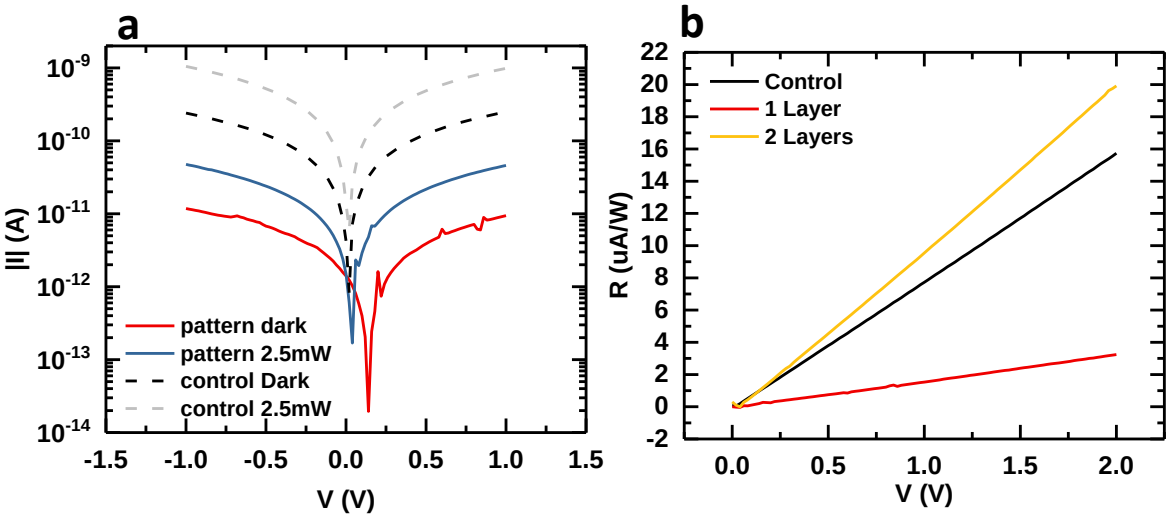

Figure 7.9 Photocurrent response of the printed device. a) I-V photo response of the control device consisting of a plain printed layer (dashed lines) and the patterned device (solid lines). b) Voltage dependent responsivity for a single plain layer (black), a single patterned (red) and a double patterned layer (yellow).

To enhance the patterned device photo-response, we increased the device thickness by stacking two QDs layers on top of each other. By increasing the device thickness, more photons are absorbed by the QDs and the photocurrent increases. An advantage of the transfer printing technology is that it can use alignment methods similar to that of conventional lithography to stack layers on top of each other, while requiring much fewer processing steps and offering the possibility to be completely solvent free. Two superposed layers of PbS QDs printed on top of each other can be seen in Figure 7.10a. Despite the 5 μm width of the patterned lines, the QDs could still be aligned and printed on top of each other. AFM imaging allows us to measure the step height of the printed layer stack (Figure 7.10b-c) and revealed a step height of 25.1 nm after ligand treatment for the first layer and 26.3 nm for the second layer. As for electrical characterisation, the I-V curves of Figure 7.10d clearly show a sharp increase of the photocurrent in the bilayer case, whereas the dark currents remain low, resulting in an

enhancement of the photoresponsivity. Unlike the single layer device, the dark characteristic of the bilayer device is centred on (0, 0) denoting an improved contact quality with the addition of the second layer.

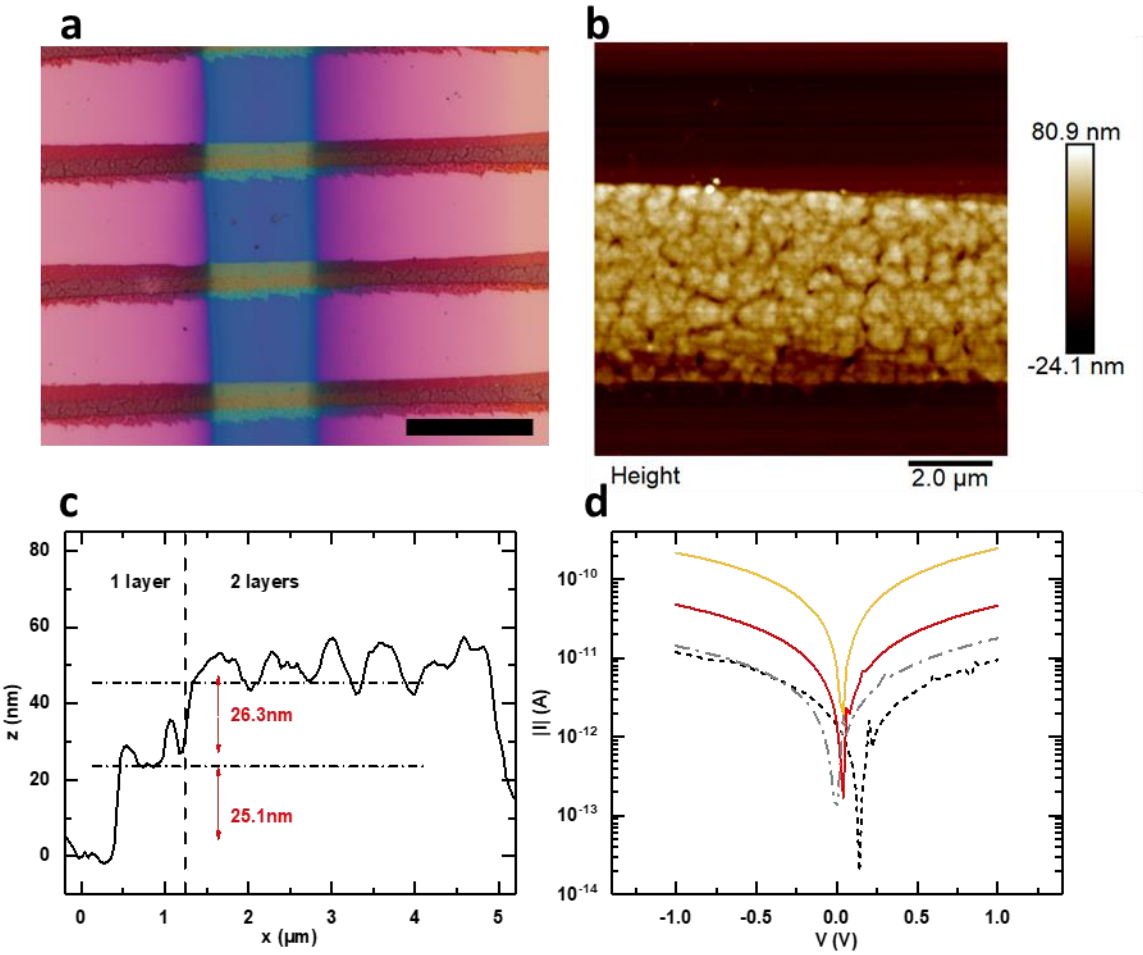

Figure 7.10. Bilayer stacking of 5 µm lines of PbS QDs. a) Optical microscope image of two arrays of 5 µm lines printed on top of each other. The darker area corresponds to the area where the two layers overlap. b) AFM and c) step profile of the stacked lines. d) Electrical comparison between the single layer patterned device (dark current: black dotted line, photocurrent: red line) and the bilayer pattern device (dark current: gray dash dotted, photocurrent: yellow solid line)

The voltage dependent responsivity was calculated according to the relation:

$$R = \frac{I_{light} - I_{dark}}{P_{in}} \tag{7.1}$$

where I_{light} is the current under light illumination, I_{dark} the dark current, and P_{in} the optical power defined as $P_{in} = P \times A$, with P the laser power density (320mW·cm^{-2}) and A the device effective area. For the control device the active area was taken to be 2×10^{-4}cm^2 and 5×10^{-5}cm^2 for the patterned devices. Figure 7.9b shows the responsivity as a function of the bias voltage for the control device (black line), a device after printing of a single layer (red), and after deposition of a second layer (yellow). At 2V bias voltage, the responsivity of the patterned device was found to be 4.86 μA/W, lower than that of the control device, which had a value of 23.60 μA/W. However, when the second patterned layer was added, the responsivity increased 6-fold to 29.87 μA/W confirming the critical influence of the device thickness on the photo response. The 6-fold increase suggests that the improvement comes not only from the thicker absorption layer but likely from other parameters affecting the electrical conductivity. As discussed above, this can come from the improved contact quality and by the same logic from the film quality itself. As QD layers are stacked on top of each other the cracks which appeared during solvent evaporation are filled improving the QD packing density and the electrical conductivity.

The normalized detectivity was derived from the responsivity using the relation $D^* = R\sqrt{A/(2qI_d)}$ with I_d the dark current and q is the electron charge. D^* was found to be 1.63×10^7 Jones for the single layer patterned device, 3.21×10^7Jones for the control plain device and increased up to 7.45×10^7 Jones for the two layer patterned device. Overall, these values are lower than the state-of-the-art PbS QDs photodetectors, which range from 10^9 Jones to 10^{11} Jones[108], [111]–[113] with best performing devices reaching 10^{13} Jones[215]. Because both the control and the patterned device showed similar performances, micro patterning techniques can be ruled out to explain the difference with the orders of magnitude observed in the literature. We speculate that the substantially lower detectivity is the result of an ultra-thin film thickness of the photoactive layer compared to that employed in more conventional devices. Nevertheless, this work shows that the usual approach

involving increasing the thickness of photo-conducting layer to improve the performance can also be applied to the case of patterned devices and can be done as a layer-by-layer approach with transfer printing. While in our experiment the alignment and layer printing was limited by the transfer printer optics and had to be done manually, Mahmoud *et al* have reported alignment accuracies of ±1.5 μm when printing QD layers on patterned electrodes, which would be suitable for the large scale printing of several layers and would allow one to match the performances of conventional photodetectors [136].

7.3.4 Temporal Response

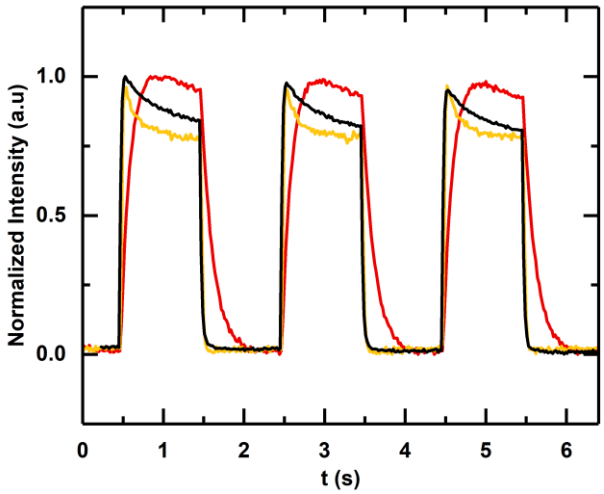

Figure 7.11. Normalised time response of a control, plain single layer device (black), a single layer patterned photodetector (red) and a bilayer patterned device (yellow).

When modulating the laser source at a fixed bias voltage, the photodetector showed transient response whose characteristics are reported in Figure 7.11. The time response was analyzed for patterned devices consisting of one or two layers, together with a control device, consisting of one non-patterned printed monolayer. The rise and fall times of the monolayer patterned device were found to be $\tau_r = 190$ ms and $\tau_f = 318$ ms, respectively. These times were noticeably shorter for the two printed layer device, having $\tau_r = 29$ ms and $\tau_f = 44$ ms, which in turn were comparable

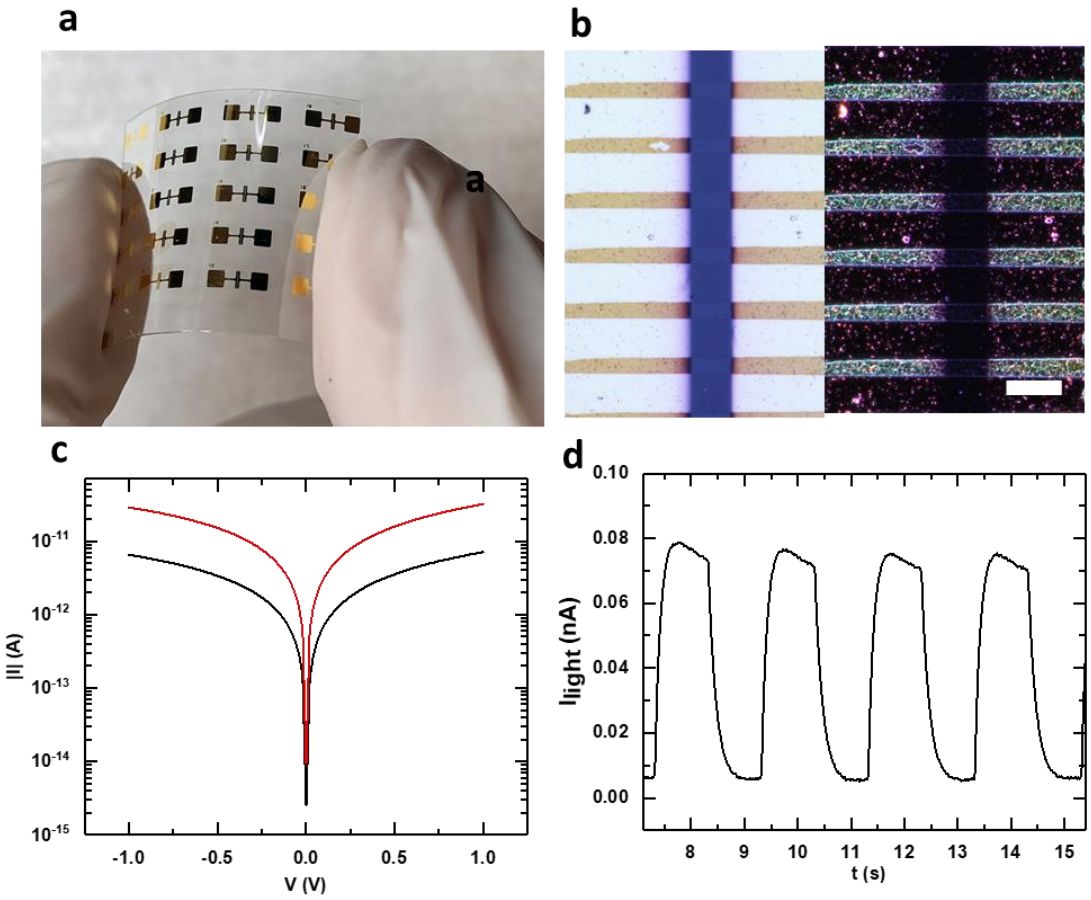

Figure 7.12. a) Flexible micropatterned PbS photoconductors. b) bright (left) and dark field optical microscope images of single layer 5 μm lines printed across gold electrodes on a PET substrate. Scale bar 20μm c) I-V photo response and d) response time of the printed device under IR light.

with the response times of the control device, found to be $\tau_r = 28$ ms and $\tau_f = 49$ ms. The time response of the control and the bilayer device was also comparable with that of spin-coated QDs devices developed in Chapter 6 via layer-by-layer deposition. The semiconductor patterning can be ruled out as the reason for the slower dynamics of the monolayer patterned device, since it was not observed in the bilayer case. Furthermore, the single layer parameter can also be factored out as both the control and tested device had identical thicknesses yet different time responses. The device thickness could also have had an impact in passivating the surface states, as the top layers and ligands protect the layers underneath. However, the impact of trap states passivation can also be minimized as the bilayer patterned device and the monolayered control device showed identical transient

response. As a result, we attribute the slower time response of the monolayered patterned device to its larger resistivity, caused by the lower cross section and higher sensitivity to cracks in the films, which in turn lower the carrier transit times and thus the response time.

7.3.5 Transparent and flexible devices

Finally, to assess the suitability of the printing of patterned QDs for transparent and flexible electronics a single layer of patterned PbS QDs was printed on a plastic PET substrate. A photograph of the printed devices is shown in Figure 7.12a. Because of the thinness of the devices, the transparency was high and the QDs layers were difficult to observe by the naked eye. Gold electrodes were deposited via shadow mask evaporation prior to printing of an array of 5×100 μm lines of PbS QDs. After deposition, the QDs were then treated with TBAI ligands, as discussed previously. Bright and dark field optical microscope images in Figure 7.12b reveals successful printing of well-defined lines bridging a 20 μm channel separating the gold contacts. As for the electrical performance, the devices were found to exhibit a responsivity of 3.20μA/W, a rise time of $\tau_r = 160$ ms and a fall time of $\tau_r = 300$ ms (Figure 7.12c-d). These values are consistent with single layered devices on silicon substrates, which suggests that the PET substrate does not affect the performances of the photodetector further.

7.4 Conclusion

In this chapter, I have described the fabrication of photoconductors using the transfer printing of micro patterned arrays of PbS QDs on gold electrodes. After optimization of the delamination and printing processes, lines of QDs could be printed with a minimal linewidth of 2.5 μm. If high definition could be achieved, the processes proved to be sensible to external parameters such as the flatness of the stamp as well as the freshness of the source QD substrate. These parameters are to be further investigated to achieve high printing yield. The photoconductor showed low photoresponsivity, which was attributed to the nanometer thinness of the photoactive layers, limiting photon absorption. However, it was shown that when printing additional layers thanks to the alignment method borrowed

from conventional UV lithography, the responsivity was found to increase 6-fold, providing a route for performance engineering. The transient rise and fall times proved to be as fast as 29ms and 44ms, respectively, which compares favorably with other PbS QDs photodetectors treated with similar ligands. Results were presented that demonstrate that the combination of transfer printing and micro patterning could be used to fabricate optoelectronic devices on various substrates, in a simple and scalable manner, requiring a limited amount of processing steps. This unique approach could be of interest for the integration of colloidal semiconductors with the next generation of flexible and transparent electronics.

8 CONCLUSION AND OUTLOOK

8.1 Summary

The overall aim of this thesis was to investigate the properties of optoelectronic devices based on PbS colloidal nanostructures, in view of future integration in near-infrared photodetection devices. The objectives were: i) develop knowledge at the material level of the interaction of the nanocrystals with their environment, ii) fabricate high performing devices capable of competing with the current state-of-the-art, iii) develop fabrication methods for large-scale manufacturing. In order to achieve this, I used two different forms of PbS nanostructures, nanowires and quantum dots, which were integrated in field effect transistors and photodetectors.

Colloidal synthesis was found to produce PbS nanowires with a high degree of crystallinity, which was confirmed using transverse electron microscopy and x-ray diffraction spectroscopy. As synthesized colloidal PbS nanowires were approximately 10 μm long for diameters ranging between 30 to 60 nm and could be easily integrated into back-gated transistors. The transistor showed p-type conductivity with record mobilities as high as 160 $cm^2V^{-1}s^{-1}$, which is nearing that of PbS nanowires grown via chemical vapour deposition, thus confirming colloidal synthesis as a viable route for the fabrication of PbS nanowire-based devices. Whilst investigating the performance of the nanowires, I stumbled across an interesting phenomenon in which the transistor modulation performance increased with aging under ambient conditions. Extensive analysis of this aging effect has led to the hypothesis that a change in stoichiometry and the reduction in sulphur concentration with time results in the reduction in the majority carrier concentration and thus improved modulation.

The nanowire FETs also showed substantial gate voltage hysteresis, which was further analysed in Chapter 5. With the aid of a time-dependent analysis it was shown that the hysteresis is caused by the presence of localized states that trap the majority carriers within the band gap when the transistor is

turned on. I also developed an innovative process for the fabrication of PbS nanowires/QDs hybrid structures using a combination of electron beam lithography and transfer printing, which helps to minimise the use of damaging solvent exposure. The hybrid structures were shown to have reduced hysteresis compared to the bare NWs FETs, which I attribute to the action of the added QD layer, and more specifically to the transfer of electrons from the QD layer to the underlying nanowire. This electron transfer temporarily passivates the aforementioned trap states leading to a reduction in the hysteresis.

After having studied nanowires and hybrid nanowire/QD devices I then focused on the fabrication of PbS QDs photoconductors, initially via layer-by-layer deposition of QD films. The impact of two common ligands, TBAI and EDT, on the performance of PbS QD photoconductors was first explored. EDT-treated devices showed higher photosensitivity when only a single layer of QD was deposited whereas TBAI had better sensitivity when 5 layers were deposited. This effect was caused by a different variation in the dark current with the number of layers, with a sharp increase in the EDT films and almost no change in TBAI films. This is attributed to the improved passivation of the QDs using TBAI, which meant that the conductivity (dark current) was less sensitive to the number of deposited layers.

The time response of the devices was also analysed and was found to be dependent on the light intensity, but largely independent of the ligand type. This preliminary study helped in the design and fabrication of PbS Schottky nanogap diodes in collaboration with Dr Dimitra Georgiadou at Imperial College London. The electrodes were made using adhesion lithography, an innovative fabrication technique which enabled the creation of 20 nm nanogaps between the gold and aluminium electrodes. The devices showed a responsivity of R = 38.7A/W in reverse bias combined with a detectivity of 3.5×10^{12} and a bandwidth of 180 Hz. These results demonstrate the compatibility of

colloidal PbS QDs with adhesion lithography fabrication processes, which is of interest in the development of IR detectors for next generation of flexible and transparent electronics.

In Chapter 7 results on flexible and transparent photodetectors were presented. These photodetectors were made from patterned PbS QDs films. The micro-patterning was enabled by transfer printing technology and the used of lithographically patterned stamps. The method proved to be efficient and reliable with the successful printing of arrayed lines with a minimal linewidth of 2.5 μm. The devices were initially found to exhibit poor device performances, but it was shown that the printing method was accurate enough to print several layers on top of each other which allowed the performances to be improved so that they were comparable with that observed for the spin-coated devices presented in Chapter 6.

8.2 Future Work

This thesis has studied PbS colloidal nanostructures for use in infrared detection devices. However, to secure their integration in next generation devices and to outperform the competition including organic and perovskites semiconductors, some of the challenges addressed in this work require further investigation.

A drawback of nanocrystal, perovskite, and organic-based devices is their stability in an ambient environment, which leads to performance degradation when operating in air. In that sense, the aging effect uncovered in Chapter 4 is interesting in that it showed that the device performances essentially improved with prolonged exposure to the atmosphere. From data analysis it was inferred that this was likely to be the result of a change of stoichiometry, but this requires a more extensive statistical analysis of the PbS composition over time to be certain. In the same vein, the passivation technique of PbS nanowires with PbS QDs was interesting since it enabled the reduction of the the device hysteresis, another common issue for nanostructures-based transistors measured in air. The fabrication yield of

these hybrid nanowire/QD devices was low due to the use of electron beam lithography, which increased the number of process steps and processing time.

I believe that the patterning method developed in Chapter 7 will help in improving the yield of the hybrid structures, with the added benefit of keeping the process completely solvent-free. The critical feature will be the ability to efficiently align the QD patterns to the nanowire (or any underlying substrate), but this should be attainable with the new generation of printers with alignment accuracies nearing 1 μm. This would also help in improving the performances of the device fabricated in Chapter 7, which were in part limited by the ability to repeatably align and print patterns on top of each other.

The next logical step would be the fabrication of PbS QDs field effect transistors using colloids, something that has been routinely done by other groups using rigorous air-free fabrication and measurement conditions (Chapter 2)m but which I have not been able to reproduce in ambient conditions. Improved passivation strategies, with for instance liquid phase ligand exchange (before deposition of the QD film) or dielectric encapsulation using atomic layer deposition, will help and should be investigated.

Nanogap-based devices are also interesting since they highlight different transport information compared to conventional FET designs. Indeed, the ultra-short channel length combined with the large electrode aspect ratio would be able to probe charge transport in QDs films over a short distance whilst measuring high current levels. This would improve the device mobility by minimising the distance over which the charges hop from one QD to another (nanosized channel), increasing the number of percolation pathways (large aspect ratio), and removing the long-range disorder effects existing in QD films. In order to achieve this, nanogap electrodes made of identical metals are needed (instead of Al-Au as in this work). While technically possible, this has proved to be challenging and an improved understanding of the adhesion lithography process is needed.

REFERENCES

[1] M. Faraday, "X. The Bakerian Lecture. —Experimental relations of gold (and other metals) to light," *Philos. Trans. R. Soc. London*, vol. 147, pp. 145–181, Jan. 1857.

[2] F. Dekker, L. Kool, A. Bunschoten, A. H. Velders, and V. Saggiomo, "Syntheses of gold and silver dichroic nanoparticles; looking at the Lycurgus cup colors," *Chem. Teach. Int.*, Mar. 2020.

[3] L. Brus, "Electronic wave functions in semiconductor clusters: experiment and theory," *J. Phys. Chem.*, vol. 90, no. 12, pp. 2555–2560, Jun. 1986.

[4] L. E. Brus, "Electron–electron and electron-hole interactions in small semiconductor crystallites: The size dependence of the lowest excited electronic state," *J. Chem. Phys.*, vol. 80, no. 9, pp. 4403–4409, May 1984.

[5] C. B. Murray, D. J. Norris, and M. G. Bawendi, "Synthesis and characterization of nearly monodisperse CdE (E = sulfur, selenium, tellurium) semiconductor nanocrystallites," *J. Am. Chem. Soc.*, vol. 115, no. 19, pp. 8706–8715, Sep. 1993.

[6] M. A. Hines and P. Guyot-Sionnest, "Synthesis and characterization of strongly luminescing ZnS-capped CdSe nanocrystals," *J. Phys. Chem.*, vol. 100, no. 2, pp. 468–471, Jan. 1996.

[7] C. R. Kagan, E. Lifshitz, E. H. Sargent, and D. V. Talapin, "Building devices from colloidal quantum dots," *Science (80-.).*, vol. 353, no. 6302, 2016.

[8] D. V Talapin, J.-S. Lee, M. V Kovalenko, and E. V Shevchenko, "Prospects of colloidal nanocrystals for electronic and optoelectronic applications.," *Chem. Rev.*, vol. 110, no. 1, pp. 389–458, Jan. 2010.

[9] J. Y. Kim, O. Voznyy, D. Zhitomirsky, and E. H. Sargent, "25th anniversary article: Colloidal quantum dot materials and devices: a quarter-century of advances.," *Adv. Mater.*, vol. 25, no. 36, pp. 4986–5010, Sep. 2013.

[10] M. A. Boles, D. Ling, T. Hyeon, and D. V. Talapin, "The surface science of nanocrystals," *Nat. Mater.*, vol. 15, no. 2, pp. 141–153, Jan. 2016.

[11] R. Saran and R. J. Curry, "Lead sulphide nanocrystal photodetector technologies," *Nat. Photonics*, vol. 10, no. 2, pp. 81–92, Jan. 2016.

[12] D. M. Balazs and M. A. Loi, "Lead-Chalcogenide Colloidal-Quantum-Dot Solids: Novel Assembly Methods, Electronic Structure Control, and Application Prospects," *Adv. Mater.*, vol. 30, no. 33, p. 1800082, Aug. 2018.

[13] C.-H. M. Chuang, P. R. Brown, V. Bulović, and M. G. Bawendi, "Improved performance and stability in quantum dot solar cells through band alignment engineering.," *Nat. Mater.*, vol. 13, no. 8, pp. 796–801, Aug. 2014.

[14] D. Kufer, I. Nikitskiy, T. Lasanta, G. Navickaite, F. H. L. Koppens, and G. Konstantatos, "Hybrid 2D-0D MoS 2 -PbS Quantum Dot Photodetectors," *Adv. Mater.*, vol. 27, no. 1, pp.

176–180, Jan. 2015.

[15] G. Konstantatos *et al.*, "Hybrid graphene–quantum dot phototransistors with ultrahigh gain," *Nat. Nanotechnol.*, vol. 7, no. 6, pp. 363–368, Jun. 2012.

[16] J. Yang, M. K. Choi, D.-H. Kim, and T. Hyeon, "Designed Assembly and Integration of Colloidal Nanocrystals for Device Applications.," *Adv. Mater.*, vol. 28, no. 6, pp. 1176–207, Feb. 2016.

[17] C. R. Kagan, "Flexible colloidal nanocrystal electronics," *Chem. Soc. Rev.*, 2018.

[18] Y. E. Panfil, M. Oded, and U. Banin, "Colloidal Quantum Nanostructures: Emerging Materials for Display Applications," *Angewandte Chemie - International Edition*, vol. 57, no. 16. Wiley-Blackwell, pp. 4274–4295, 09-Apr-2018.

[19] K. F. Brennan, "Optoelectronic Emitters," in *The Physics of Semiconductors*, Cambridge: Cambridge University Press, 1999, pp. 673–708.

[20] S. M. Sze and K. K. Ng, *Physics of Semiconductor Devices: Third Edition*. John Wiley & Sons, Inc., 2006.

[21] G. Konstantatos and E. H. Sargent, *Colloidal Quantum Dot Optoelectronics and Photovoltaics*. Cambridge: Cambridge University Press, 2013.

[22] A. L. Efros and M. Rosen, "The Electronic Structure of Semiconductor Nanocrystals," *Annu. Rev. Mater. Sci.*, vol. 30, no. 1, pp. 475–521, Aug. 2000.

[23] M. S. Gudiksen, J. Wang, and C. M. Lieber, "Size-dependent photoluminescence from single indium phosphide nanowires," *J. Phys. Chem. B*, vol. 106, no. 16, pp. 4036–4039, 2002.

[24] R. Dingle, "Confined carrier quantum states in ultrathin semiconductor heterostructures," in *Festkörperprobleme 15*, Berlin, Heidelberg: Springer Berlin Heidelberg, 1975, pp. 21–48.

[25] H. Yu, J. Li, R. A. Loomis, L.-W. Wang, and W. E. Buhro, "Two- versus three-dimensional quantum confinement in indium phosphide wires and dots," *Nat. Mater.*, vol. 2, no. 8, pp. 517–520, Aug. 2003.

[26] Y. Yin and A. P. Alivisatos, "Colloidal nanocrystal synthesis and the organic–inorganic interface," *Nature*, vol. 437, no. 7059, pp. 664–670, Sep. 2005.

[27] A. H. Ip *et al.*, "Hybrid passivated colloidal quantum dot solids.," *Nat. Nanotechnol.*, vol. 7, no. 9, pp. 577–82, Sep. 2012.

[28] J. M. Luther, M. Law, Q. Song, C. L. Perkins, M. C. Beard, and A. J. Nozik, "Structural, optical, and electrical properties of self-assembled films of PbSe nanocrystals treated with 1,2-ethanedithiol.," *ACS Nano*, vol. 2, no. 2, pp. 271–80, Feb. 2008.

[29] P. R. Brown *et al.*, "Energy level modification in lead sulfide quantum dot thin films through ligand exchange.," *ACS Nano*, vol. 8, no. 6, pp. 5863–72, Jun. 2014.

[30] N. T. K. Thanh, N. Maclean, and S. Mahiddine, "Mechanisms of nucleation and growth of nanoparticles in solution," *Chemical Reviews*. 2014.

[31] J. Schmitt *et al.*, "Formation of Superlattices of Gold Nanoparticles Using Ostwald Ripening in Emulsions: Transition from fcc to bcc Structure," *J. Phys. Chem. B*, 2016.

[32] R. S. Allgaier, "History of narrow-gap semiconductors and semimetals, 1945-65," *Semicond. Sci. Technol.*, vol. 5, no. 3S, pp. S326–S333, Mar. 1990.

[33] G. Bauer and H. Clemens, "Physics and applications of IV-VI compound quantum well and superlattice structures," *Semicond. Sci. Technol.*, vol. 5, no. 3S, pp. S122–S130, Mar. 1990.

[34] A. Rogalski, "History of infrared detectors," *Opto-electronics Rev.*, 2012.

[35] I. Moreels, Y. Justo, B. De Geyter, K. Haustraete, J. C. Martins, and Z. Hens, "Size-Tunable, Bright, and Stable PbS Quantum Dots: A Surface Chemistry Study," *ACS Nano*, vol. 5, no. 3, pp. 2004–2012, Mar. 2011.

[36] M. A. Hines and G. D. Scholes, "Colloidal PbS Nanocrystals with Size-Tunable Near-Infrared Emission: Observation of Post-Synthesis Self-Narrowing of the Particle Size Distribution," *Adv. Mater.*, vol. 15, no. 21, pp. 1844–1849, Nov. 2003.

[37] K. A. Abel, J. Shan, J. C. Boyer, F. Harris, and F. C. J. M. van Veggel, "Highly photoluminescent PbS nanocrystals: The beneficial effects of trioctylphosphine," *Chem. Mater.*, 2008.

[38] L. Cademartiri, J. Bertolotti, R. Sapienza, D. S. Wiersma, G. Von Freymann, and G. A. Ozin, "Multigram scale, solventless, and diffusion-controlled route to highly monodisperse PbS nanocrystals," *J. Phys. Chem. B*, vol. 110, no. 2, pp. 671–673, 2006.

[39] I. Moreels *et al.*, "Size-dependent optical properties of colloidal PbS quantum dots.," *ACS Nano*, vol. 3, no. 10, pp. 3023–30, Oct. 2009.

[40] S. M. Lee, Y. wook Jun, S. N. Cho, and J. Cheon, "Single-crystalline star-shaped nanocrystals and their evolution: Programming the geometry of nano-building blocks," *J. Am. Chem. Soc.*, 2002.

[41] D. Zherebetskyy *et al.*, "Hydroxylation of the surface of PbS nanocrystals passivated with oleic acid.," *Science*, vol. 344, no. 6190, pp. 1380–4, Jun. 2014.

[42] C. Schliehe *et al.*, "Ultrathin PbS sheets by two-dimensional oriented attachment.," *Science*, vol. 329, no. 5991, pp. 550–3, Jul. 2010.

[43] R. L. Penn, "Imperfect Oriented Attachment: Dislocation Generation in Defect-Free Nanocrystals," *Science (80-.).*, vol. 281, no. 5379, pp. 969–971, Aug. 1998.

[44] I. Patla, S. Acharya, L. Zeiri, J. Israelachvili, S. Efrima, and Y. Golan, "Synthesis, two-dimensional assembly, and surface pressure-induced coalescence of ultranarrow PbS nanowires.," *Nano Lett.*, vol. 7, no. 6, pp. 1459–62, Jun. 2007.

[45] S. Acharya, U. K. Gautam, T. Sasaki, Y. Bando, Y. Golan, and K. Ariga, "Ultra narrow PbS nanorods with intense fluorescence.," *J. Am. Chem. Soc.*, vol. 130, no. 14, pp. 4594–5, Apr. 2008.

[46] K.-S. Cho, D. V Talapin, W. Gaschler, and C. B. Murray, "Designing PbSe nanowires and nanorings through oriented attachment of nanoparticles.," *J. Am. Chem. Soc.*, vol. 127, no. 19, pp. 7140–7, May 2005.

[47] D. V. Talapin, C. T. Black, C. R. Kagan, E. V. Shevchenko, A. Afzali, and C. B. Murray, "Alignment, Electronic Properties, Doping, and On-Chip Growth of Colloidal PbSe Nanowires," *J. Phys. Chem. C*, vol. 111, no. 35, pp. 13244–13249, Sep. 2007.

[48] C. Fang, M. A. van Huis, D. Vanmaekelbergh, and H. W. Zandbergen, "Energetics of Polar and Nonpolar Facets of PbSe Nanocrystals from Theory and Experiment," *ACS Nano*, vol. 4, no. 1, pp. 211–218, Jan. 2010.

[49] F. Wang, A. Dong, and W. E. Buhro, "Solution–Liquid–Solid Synthesis, Properties, and Applications of One-Dimensional Colloidal Semiconductor Nanorods and Nanowires," *Chem. Rev.*, vol. 116, no. 18, pp. 10888–10933, Sep. 2016.

[50] T. J. Trentler, K. M. Hickman, S. C. Goel, A. M. Viano, P. C. Gibbons, and W. E. Buhro, "Solution-Liquid-Solid Growth of Crystalline III-V Semiconductors: An Analogy to Vapor-Liquid-Solid Growth," *Science (80-.).*, vol. 270, no. 5243, pp. 1791–1794, Dec. 1995.

[51] F. Wang, A. Dong, J. Sun, R. Tang, H. Yu, and W. E. Buhro, "Solution-liquid-solid growth of semiconductor nanowires.," *Inorg. Chem.*, vol. 45, no. 19, pp. 7511–21, Sep. 2006.

[52] K.-T. Yong, Y. Sahoo, K. R. Choudhury, M. T. Swihart, J. R. Minter, and P. N. Prasad, "Control of the Morphology and Size of PbS Nanowires Using Gold Nanoparticles," *Chem. Mater.*, vol. 18, no. 25, pp. 5965–5972, Dec. 2006.

[53] A. C. Onicha, N. Petchsang, T. H. Kosel, and M. Kuno, "Controlled synthesis of compositionally tunable ternary PbSe(x)S(1-x) as well as binary PbSe and PbS nanowires.," *ACS Nano*, vol. 6, no. 3, pp. 2833–43, Mar. 2012.

[54] A. Javey, J. Guo, Q. Wang, M. Lundstrom, and H. Dai, "Ballistic carbon nanotube field-effect transistors," *Nature*, vol. 424, no. 6949, pp. 654–657, Aug. 2003.

[55] D. Jariwala, V. K. Sangwan, L. J. Lauhon, T. J. Marks, and M. C. Hersam, "Emerging device applications for semiconducting two-dimensional transition metal dichalcogenides.," *ACS Nano*, vol. 8, no. 2, pp. 1102–20, Feb. 2014.

[56] D. M. Balazs *et al.*, "Colloidal Quantum Dot Inks for Single-Step-Fabricated Field-Effect Transistors: The Importance of Postdeposition Ligand Removal," *ACS Appl. Mater. Interfaces*, vol. 10, no. 6, pp. 5626–5632, Jan. 2018.

[57] C. B. Murray, C. R. Kagan, and M. G. Bawendi, "Synthesis and Characterization of Monodisperse Nanocrystals and Close-Packed Nanocrystal Assemblies," *Annu. Rev. Mater. Sci.*, vol. 30, no. 1, pp. 545–610, Aug. 2000.

[58] M. H. Zarghami, Y. Liu, M. Gibbs, E. Gebremichael, C. Webster, and M. Law, "p-Type PbSe and PbS quantum dot solids prepared with short-chain acids and diacids.," *ACS Nano*, vol. 4, no. 4, pp. 2475–85, Apr. 2010.

[59] Y. Liu *et al.*, "Dependence of carrier mobility on nanocrystal size and ligand length in PbSe

nanocrystal solids.," *Nano Lett.*, vol. 10, no. 5, pp. 1960–9, May 2010.

[60] A. G. Pattantyus-Abraham *et al.*, "Depleted-heterojunction colloidal quantum dot solar cells.," *ACS Nano*, vol. 4, no. 6, pp. 3374–80, Jun. 2010.

[61] W.-K. Koh, S. R. Saudari, A. T. Fafarman, C. R. Kagan, and C. B. Murray, "Thiocyanate-capped PbS nanocubes: ambipolar transport enables quantum dot based circuits on a flexible substrate.," *Nano Lett.*, vol. 11, no. 11, pp. 4764–7, Nov. 2011.

[62] M. V Kovalenko, M. Scheele, and D. V Talapin, "Colloidal nanocrystals with molecular metal chalcogenide surface ligands.," *Science*, vol. 324, no. 5933, pp. 1417–20, Jun. 2009.

[63] Z. Ning *et al.*, "Air-stable n-type colloidal quantum dot solids.," *Nat. Mater.*, vol. 13, no. 8, pp. 822–8, Aug. 2014.

[64] D. Kim, D.-H. Kim, J.-H. Lee, and J. C. Grossman, "Impact of stoichiometry on the electronic structure of PbS quantum dots.," *Phys. Rev. Lett.*, vol. 110, no. 19, p. 196802, May 2013.

[65] J. Tang *et al.*, "Colloidal-quantum-dot photovoltaics using atomic-ligand passivation.," *Nat. Mater.*, vol. 10, no. 10, pp. 765–71, Oct. 2011.

[66] J. Tang *et al.*, "Quantum dot photovoltaics in the extreme quantum confinement regime: the surface-chemical origins of exceptional air- and light-stability.," *ACS Nano*, vol. 4, no. 2, pp. 869–78, Feb. 2010.

[67] F. S. Stinner *et al.*, "Flexible, High-Speed CdSe Nanocrystal Integrated Circuits," *Nano Lett.*, vol. 15, no. 10, pp. 7155–7160, Oct. 2015.

[68] D. K. Kim, Y. Lai, B. T. Diroll, C. B. Murray, and C. R. Kagan, "Flexible and low-voltage integrated circuits constructed from high-performance nanocrystal transistors.," *Nat. Commun.*, vol. 3, no. 1, p. 1216, Jan. 2012.

[69] D. S. Chung, J.-S. Lee, J. Huang, A. Nag, S. Ithurria, and D. V. Talapin, "Low voltage, hysteresis free, and high mobility transistors from all-inorganic colloidal nanocrystals.," *Nano Lett.*, vol. 12, no. 4, pp. 1813–20, Apr. 2012.

[70] J.-H. Choi *et al.*, "Bandlike Transport in Strongly Coupled and Doped Quantum Dot Solids: A Route to High-Performance Thin-Film Electronics," *Nano Lett.*, vol. 12, no. 5, pp. 2631–2638, May 2012.

[71] J.-S. Lee, M. V Kovalenko, J. Huang, D. S. Chung, and D. V Talapin, "Band-like transport, high electron mobility and high photoconductivity in all-inorganic nanocrystal arrays.," *Nat. Nanotechnol.*, vol. 6, no. 6, pp. 348–52, Jun. 2011.

[72] D. S. Dolzhnikov *et al.*, "Materials chemistry. Composition-matched molecular "solders" for semiconductors.," *Science*, vol. 347, no. 6220, pp. 425–8, Jan. 2015.

[73] D. V Talapin and C. B. Murray, "PbSe nanocrystal solids for n- and p-channel thin film field-effect transistors.," *Science*, vol. 310, no. 5745, pp. 86–9, Oct. 2005.

[74] Y. Liu *et al.*, "PbSe Quantum Dot Field-Effect Transistors with Air-Stable Electron Mobilities above 7 cm ^{2} V $^{-1}$ s $^{-1}$," *Nano Lett.*, vol. 13, no. 4, pp. 1578–1587, Apr. 2013.

[75] S. J. Oh *et al.*, "Engineering Charge Injection and Charge Transport for High Performance PbSe Nanocrystal Thin Film Devices and Circuits," *Nano Lett.*, vol. 14, no. 11, pp. 6210–6216, Nov. 2014.

[76] S. J. Oh *et al.*, "Stoichiometric control of lead chalcogenide nanocrystal solids to enhance their electronic and optoelectronic device performance.," *ACS Nano*, vol. 7, no. 3, pp. 2413–21, Mar. 2013.

[77] D. M. Balazs *et al.*, "Electron Mobility of 24 cm ^{2} V $^{-1}$ s $^{-1}$ in PbSe Colloidal-Quantum-Dot Superlattices," *Adv. Mater.*, vol. 30, no. 38, p. 1802265, Sep. 2018.

[78] I. J. Kramer and E. H. Sargent, "The architecture of colloidal quantum dot solar cells: materials to devices.," *Chem. Rev.*, vol. 114, no. 1, pp. 863–82, Jan. 2014.

[79] S. J. Oh *et al.*, "Designing high-performance PbS and PbSe nanocrystal electronic devices through stepwise, post-synthesis, colloidal atomic layer deposition," *Nano Lett.*, vol. 14, no. 3, pp. 1559–1566, Mar. 2014.

[80] T. P. Osedach *et al.*, "Bias-stress effect in 1,2-ethanedithiol-treated PbS quantum dot field-effect transistors," *ACS Nano*, vol. 6, no. 4, pp. 3121–3127, Apr. 2012.

[81] S. Z. Bisri, C. Piliego, M. Yarema, W. Heiss, and M. A. Loi, "Low driving voltage and high mobility ambipolar field-effect transistors with PbS colloidal nanocrystals.," *Adv. Mater.*, vol. 25, no. 31, pp. 4309–14, Aug. 2013.

[82] D. Zhitomirsky *et al.*, "N-type colloidal-quantum-dot solids for photovoltaics.," *Adv. Mater.*, vol. 24, no. 46, pp. 6181–5, Dec. 2012.

[83] D. M. Balazs *et al.*, "Counterion-Mediated Ligand Exchange for PbS Colloidal Quantum Dot Superlattices.," *ACS Nano*, Nov. 2015.

[84] C. H. Jo *et al.*, "Low-temperature annealed PbS quantum dot films for scalable and flexible ambipolar thin-film-transistors and circuits," *J. Mater. Chem. C*, vol. 2, no. 48, pp. 10305–10311, Oct. 2014.

[85] W. Koh, S. R. Saudari, A. T. Fafarman, C. R. Kagan, and C. B. Murray, "Thiocyanate-Capped PbS Nanocubes: Ambipolar Transport Enables Quantum Dot Based Circuits on a Flexible Substrate," *Nano Lett.*, vol. 11, no. 11, pp. 4764–4767, Nov. 2011.

[86] D. M. Balazs, M. I. Nugraha, S. Z. Bisri, M. Sytnyk, W. Heiss, and M. A. Loi, "Reducing charge trapping in PbS colloidal quantum dot solids," *Appl. Phys. Lett.*, vol. 104, no. 11, p. 112104, Mar. 2014.

[87] R. H. Harada and H. T. Minden, "Photosensitization of PbS films," *Phys. Rev.*, vol. 102, no. 5, pp. 1258–1262, Jun. 1956.

[88] A. G. Shulga *et al.*, "An All-Solution-Based Hybrid CMOS-Like Quantum Dot/Carbon Nanotube Inverter," *Adv. Mater.*, vol. 29, no. 35, p. 1701764, Sep. 2017.

[89] D. K. Kim, T. R. Vemulkar, S. J. Oh, W.-K. Koh, C. B. Murray, and C. R. Kagan, "Ambipolar and unipolar PbSe nanowire field-effect transistors.," *ACS Nano*, vol. 5, no. 4, pp. 3230–6, Apr. 2011.

[90] D. K. Kim, Y. Lai, T. R. Vemulkar, and C. R. Kagan, "Flexible, low-voltage, and low-hysteresis PbSe nanowire field-effect transistors.," *ACS Nano*, vol. 5, no. 12, pp. 10074–83, Dec. 2011.

[91] S. J. Oh *et al.*, "Selective p- and n-Doping of Colloidal PbSe Nanowires To Construct Electronic and Optoelectronic Devices," *ACS Nano*, vol. 9, no. 7, pp. 7536–7544, Jul. 2015.

[92] S. Y. Jang *et al.*, "Three synthetic routes to single-crystalline PbS nanowires with controlled growth direction and their electrical transport properties.," *ACS Nano*, vol. 4, no. 4, pp. 2391–401, Apr. 2010.

[93] W. S. Loc *et al.*, "Facet-controlled facilitation of PbS nanoarchitectures by understanding nanocrystal growth," *Nanoscale*, vol. 7, no. 45, pp. 19047–19052, 2015.

[94] F. Xu, X. Ma, L. F. Gerlein, and S. G. Cloutier, "Designing and building nanowires: directed nanocrystal self-assembly into radically branched and zigzag PbS nanowires.," *Nanotechnology*, vol. 22, no. 26, p. 265604, Jul. 2011.

[95] P. Giraud *et al.*, "Field effect transistors and phototransistors based upon p-type solution-processed PbS nanowires," *Nanotechnology*, vol. 29, no. 7, Feb. 2018.

[96] R. L. Petritz, "Theory of Photoconductivity in Semiconductor Films," *Phys. Rev.*, vol. 104, no. 6, pp. 1508–1516, Dec. 1956.

[97] H. Fang and W. Hu, "Photogating in Low Dimensional Photodetectors," *Advanced Science*, vol. 4, no. 12. p. 1700323, 04-Oct-2017.

[98] H. Liu, E. Lhuillier, and P. Guyot-Sionnest, "1/f noise in semiconductor and metal nanocrystal solids," *J. Appl. Phys.*, vol. 115, no. 15, p. 154309, Apr. 2014.

[99] F. P. García De Arquer, A. Armin, P. Meredith, and E. H. Sargent, "Solution-processed semiconductors for next-generation photodetectors," *Nature Reviews Materials*, vol. 2, no. 3. Nature Publishing Group, p. 16100, 24-Jan-2017.

[100] Z. Ren *et al.*, "Bilayer PbS Quantum Dots for High-Performance Photodetectors," *Adv. Mater.*, vol. 29, no. 33, p. 1702055, Sep. 2017.

[101] J. He *et al.*, "Synergetic Effect of Silver Nanocrystals Applied in PbS Colloidal Quantum Dots for High-Performance Infrared Photodetectors," *ACS Photonics*, vol. 1, no. 10, pp. 936–943, Oct. 2014.

[102] J. P. Clifford, K. W. Johnston, L. Levina, and E. H. Sargent, "Schottky barriers to colloidal quantum dot films," *Appl. Phys. Lett.*, vol. 91, no. 25, p. 253117, Dec. 2007.

[103] G. Konstantatos *et al.*, "Ultrasensitive solution-cast quantum dot photodetectors.," *Nature*, vol. 442, no. 7099, pp. 180–3, Jul. 2006.

[104] G. Konstantatos, J. Clifford, L. Levina, and E. H. Sargent, "Sensitive solution-processed visible-wavelength photodetectors," *Nat. Photonics*, vol. 1, no. 9, pp. 531–534, Sep. 2007.

[105] G. Konstantatos, L. Levina, A. Fischer, and E. H. Sargent, "Engineering the Temporal Response of Photoconductive Photodetectors via Selective Introduction of Surface Trap States," *Nano Lett.*, vol. 8, no. 5, pp. 1446–1450, May 2008.

[106] G. Konstantatos and E. H. Sargent, "PbS colloidal quantum dot photoconductive photodetectors: Transport, traps, and gain," *Appl. Phys. Lett.*, 2007.

[107] S. Yakunin *et al.*, "High Infrared Photoconductivity in Films of Arsenic-Sulfide-Encapsulated Lead-Sulfide Nanocrystals," *ACS Nano*, vol. 8, no. 12, pp. 12883–12894, Dec. 2014.

[108] C. Hu *et al.*, "Air-stable short-wave infrared PbS colloidal quantum dot photoconductors passivated with Al 2 O 3 atomic layer deposition," *Appl. Phys. Lett.*, vol. 105, no. 17, p. 171110, Oct. 2014.

[109] L. Mi *et al.*, "Ultrasensitive PbS-Quantum-Dot Photodetectors for Visible-Near-Infrared Light Through Surface Atomic-Ligand Exchange," *Part. Part. Syst. Charact.*, vol. 32, no. 12, pp. 1102–1109, Dec. 2015.

[110] K. Szendrei *et al.*, "Solution-Processable Near-IR Photodetectors Based on Electron Transfer from PbS Nanocrystals to Fullerene Derivatives," *Adv. Mater.*, vol. 21, no. 6, pp. 683–687, Feb. 2009.

[111] T. P. Osedach *et al.*, "Interfacial Recombination for Fast Operation of a Planar Organic/QD Infrared Photodetector," *Adv. Mater.*, vol. 22, no. 46, pp. 5250–5254, Dec. 2010.

[112] F. P. García De Arquer, T. Lasanta, M. Bernechea, and G. Konstantatos, "Tailoring the electronic properties of colloidal quantum dots in metal-semiconductor nanocomposites for high performance photodetectors," *Small*, vol. 11, no. 22, pp. 2636–2641, Jun. 2015.

[113] Z. Ren *et al.*, "Bilayer PbS Quantum Dots for High-Performance Photodetectors," *Adv. Mater.*, vol. 29, no. 33, p. 1702055, Sep. 2017.

[114] P. Nagpal and V. I. Klimov, "Role of mid-gap states in charge transport and photoconductivity in semiconductor nanocrystal films.," *Nat. Commun.*, vol. 2, p. 486, Jan. 2011.

[115] K. S. Novoselov *et al.*, "2D materials and van der Waals heterostructures.," *Science*, vol. 353, no. 6298, p. aac9439, Jul. 2016.

[116] S. Pak *et al.*, "Consecutive Junction-Induced Efficient Charge Separation Mechanisms for High-Performance MoS 2 /Quantum Dot Phototransistors," *ACS Appl. Mater. Interfaces*, vol. 10, no. 44, pp. 38264–38271, Nov. 2018.

[117] V. Adinolfi, I. J. Kramer, A. J. Labelle, B. R. Sutherland, S. Hoogland, and E. H. Sargent, "Photojunction Field-Effect Transistor Based on a Colloidal Quantum Dot Absorber Channel Layer," *ACS Nano*, vol. 9, no. 1, pp. 356–362, Jan. 2015.

[118] D. Zhitomirsky, O. Voznyy, S. Hoogland, and E. H. Sargent, "Measuring Charge Carrier

Diffusion in Coupled Colloidal Quantum Dot Solids," *ACS Nano*, vol. 7, no. 6, pp. 5282–5290, Jun. 2013.

[119] J. P. Clifford, G. Konstantatos, K. W. Johnston, S. Hoogland, L. Levina, and E. H. Sargent, "Fast, sensitive and spectrally tuneable colloidal-quantum-dot photodetectors," *Nat. Nanotechnol.*, vol. 4, no. 1, pp. 40–44, Jan. 2009.

[120] D. B. Strasfeld, A. Dorn, D. D. Wanger, and M. G. Bawendi, "Imaging Schottky Barriers and Ohmic Contacts in PbS Quantum Dot Devices," *Nano Lett.*, vol. 12, no. 2, pp. 569–575, Feb. 2012.

[121] L. Mi *et al.*, "High performance visible–near-infrared PbS-quantum-dots/indium Schottky diodes for photodetectors," *Nanotechnology*, vol. 28, no. 5, p. 055202, Feb. 2017.

[122] A. Maulu *et al.*, "Strongly-coupled PbS QD solids by doctor blading for IR photodetection," *RSC Adv.*, vol. 6, no. 83, pp. 80201–80212, 2016.

[123] M. Yuan, M. Liu, and E. H. Sargent, "Colloidal quantum dot solids for solution-processed solar cells," *Nat. Energy*, vol. 1, no. 3, p. 16016, Feb. 2016.

[124] E. H. Sargent, "Colloidal quantum dot solar cells," *Nat. Photonics*, vol. 6, no. 3, pp. 133–135, Feb. 2012.

[125] B. N. Pal, I. Robel, A. Mohite, R. Laocharoensuk, D. J. Werder, and V. I. Klimov, "High-Sensitivity p-n Junction Photodiodes Based on PbS Nanocrystal Quantum Dots," *Adv. Funct. Mater.*, vol. 22, no. 8, pp. 1741–1748, Apr. 2012.

[126] K. Qiao *et al.*, "Efficient interface and bulk passivation of PbS quantum dot infrared photodetectors by PbI 2 incorporation," *RSC Adv.*, vol. 7, no. 83, pp. 52947–52954, 2017.

[127] R. Dong *et al.*, "An Ultraviolet-to-NIR Broad Spectral Nanocomposite Photodetector with Gain," *Adv. Opt. Mater.*, vol. 2, no. 6, pp. 549–554, Jun. 2014.

[128] A. Carlson, A. M. Bowen, Y. Huang, R. G. Nuzzo, and J. A. Rogers, "Transfer printing techniques for materials assembly and micro/nanodevice fabrication.," *Adv. Mater.*, vol. 24, no. 39, pp. 5284–318, Oct. 2012.

[129] T.-H. Kim *et al.*, "Heterogeneous stacking of nanodot monolayers by dry pick-and-place transfer and its applications in quantum dot light-emitting diodes.," *Nat. Commun.*, vol. 4, p. 2637, Jan. 2013.

[130] N. E. Hjerrild, D. C. J. Neo, A. Kasdi, H. E. Assender, J. H. Warner, and A. A. R. Watt, "Transfer Printed Silver Nanowire Transparent Conductors for PbS-ZnO Heterojunction Quantum Dot Solar Cells.," *ACS Appl. Mater. Interfaces*, Mar. 2015.

[131] A. Thanniyil Sebastian, R. De Alba, N. Zhelev, H. Craighead, and J. Parpia, "Transfer Printing of CVD Graphene FETs on Patterned Substrates," *Nanoscale*, Jul. 2015.

[132] S. Cha, M. Cha, S. Lee, J. H. Kang, and C. Kim, "Low-Temperature, Dry Transfer-Printing of a Patterned Graphene Monolayer.," *Sci. Rep.*, vol. 5, p. 17877, Jan. 2015.

[133] P. Björk, S. Holmström, and O. Inganäs, "Soft lithographic printing of patterns of stretched DNA and DNA/electronic polymer wires by surface-energy modification and transfer," *Small*, vol. 2, no. 8–9, pp. 1068–1074, Aug. 2006.

[134] J. H. Ahn *et al.*, "Heterogeneous three-dimensional electronics by use of printed semiconductor nanomaterials," *Science (80-.).*, vol. 314, no. 5806, pp. 1754–1757, Dec. 2006.

[135] T.-H. Kim *et al.*, "Full-colour quantum dot displays fabricated by transfer printing," *Nat. Photonics*, vol. 5, no. 3, pp. 176–182, Feb. 2011.

[136] N. Mahmoud, W. Walravens, J. Kuhs, C. Detavernier, Z. Hens, and G. Roelkens, "Micro-Transfer-Printing of Al_2O_3 -Capped Short-Wave-Infrared PbS Quantum Dot Photoconductors," *ACS Appl. Nano Mater.*, vol. 2, no. 1, pp. 299–306, Jan. 2019.

[137] X. Feng, M. A. Meitl, A. M. Bowen, Y. Huang, R. G. Nuzzo, and J. A. Rogers, "Competing fracture in kinetically controlled transfer printing.," *Langmuir*, vol. 23, no. 25, pp. 12555–60, Dec. 2007.

[138] A. N. Gent and J. Schultz, "Effect of Wetting Liquids on the Strength of Adhesion of Viscoelastic Materials," *J. Adhes.*, vol. 3, no. 4, pp. 281–294, Mar. 1972.

[139] E. Barthel and S. Roux, "Velocity-dependent adherence: An analytical approach for the JKR and DMT models," *Langmuir*, vol. 16, no. 21, pp. 8134–8138, 2000.

[140] N. P. Dasgupta *et al.*, "25th Anniversary Article: Semiconductor Nanowires - Synthesis, Characterization, and Applications," *Adv. Mater.*, vol. 26, no. 14, pp. 2137–2184, Apr. 2014.

[141] X. Duan, Y. Huang, Y. Cui, J. Wang, and C. M. Lieber, "Indium phosphide nanowires as building blocks for nanoscale electronic and optoelectronic devices.," *Nature*, vol. 409, no. 6816, pp. 66–9, Jan. 2001.

[142] Y. Huang, "Logic Gates and Computation from Assembled Nanowire Building Blocks," *Science (80-.).*, vol. 294, no. 5545, pp. 1313–1317, Nov. 2001.

[143] Q. Wan *et al.*, "Fabrication and ethanol sensing characteristics of ZnO nanowire gas sensors," *Appl. Phys. Lett.*, vol. 84, no. 18, pp. 3654–3656, May 2004.

[144] C. Soci, A. Zhang, X.-Y. Bao, H. Kim, Y. Lo, and D. Wang, "Nanowire photodetectors," *J. Nanosci. Nanotechnol.*, vol. 10, no. 3, pp. 1430–49, Mar. 2010.

[145] V. I. Klimov *et al.*, "Optical gain and stimulated emission in nanocrystal quantum dots," *Science (80-.).*, vol. 290, no. 5490, pp. 314–317, Oct. 2000.

[146] M. S. Gudiksen, L. J. Lauhon, J. Wang, D. C. Smith, and C. M. Lieber, "Growth of nanowire superlattice structures for nanoscale photonics and electronics," *Nature*, vol. 415, no. 6872, pp. 617–620, Feb. 2002.

[147] P. Yang *et al.*, "Controlled Growth of ZnO Nanowires and Their Optical Properties," *Adv. Funct. Mater.*, vol. 12, no. 5, p. 323, May 2002.

[148] F. Wang, A. Dong, J. Sun, R. Tang, H. Yu, and W. E. Buhro, "Solution−Liquid−Solid

Growth of Semiconductor Nanowires," *Inorg. Chem.*, vol. 45, no. 19, pp. 7511–7521, Sep. 2006.

[149] H. Zhang *et al.*, "Interatomic Coulombic interactions as the driving force for oriented attachment," *CrystEngComm*, vol. 16, no. 8, pp. 1568–1578, 2014.

[150] X. Xue *et al.*, "Crystal growth by oriented attachment: kinetic models and control factors," *CrystEngComm*, vol. 16, no. 8, p. 1419, 2014.

[151] W. Liang, O. Rabin, A. I. Hochbaum, M. Fardy, M. Zhang, and P. Yang, "Thermoelectric properties of p-type PbSe nanowires," *Nano Res.*, vol. 2, no. 5, pp. 394–399, Mar. 2010.

[152] V. Scardaci, R. Coull, P. E. Lyons, D. Rickard, and J. N. Coleman, "Spray Deposition of Highly Transparent, Low-Resistance Networks of Silver Nanowires over Large Areas," *Small*, vol. 7, no. 18, pp. 2621–2628, Sep. 2011.

[153] J. Krantz, M. Richter, S. Spallek, E. Spiecker, and C. J. Brabec, "Solution-Processed Metallic Nanowire Electrodes as Indium Tin Oxide Replacement for Thin-Film Solar Cells," *Adv. Funct. Mater.*, vol. 21, no. 24, pp. 4784–4787, Dec. 2011.

[154] M. S. Pawar, P. K. Bankar, M. A. More, and D. J. Late, "PbS Nanostar-Like Structures as Field Emitters," *ChemistrySelect*, vol. 2, no. 18, pp. 5175–5179, Jun. 2017.

[155] B. Hou *et al.*, "Red green blue emissive lead sulfide quantum dots: heterogeneous synthesis and applications," *J. Mater. Chem. C*, vol. 5, no. 15, pp. 3692–3698, Apr. 2017.

[156] B. Hou *et al.*, "Highly Monodispersed PbS Quantum Dots for Outstanding Cascaded-Junction Solar Cells," *ACS Energy Lett.*, vol. 1, no. 4, pp. 834–839, Oct. 2016.

[157] O. Wunnicke, "Gate capacitance of back-gated nanowire field-effect transistors," *Appl. Phys. Lett.*, vol. 89, no. 8, p. 083102, Aug. 2006.

[158] R. Graham, C. Miller, E. Oh, and D. Yu, "Electric Field Dependent Photocurrent Decay Length in Single Lead Sulfide Nanowire Field Effect Transistors," *Nano Lett.*, vol. 11, no. 2, pp. 717–722, Feb. 2011.

[159] Y. Yang, X. Peng, and D. Yu, "High intensity induced photocurrent polarity switching in lead sulfide nanowire field effect transistors.," *Nanotechnology*, vol. 25, no. 19, p. 195202, May 2014.

[160] Y. Yang, J. Li, H. Wu, E. Oh, and D. Yu, "Controlled Ambipolar Doping and Gate Voltage Dependent Carrier Diffusion Length in Lead Sulfide Nanowires," *Nano Lett.*, vol. 12, no. 11, pp. 5890–5896, Nov. 2012.

[161] S. Lee *et al.*, "The Optoelectronic Properties of PbS Nanowire Field-Effect Transistors," *IEEE Trans. Nanotechnol.*, vol. 12, no. 6, pp. 1135–1138, Nov. 2013.

[162] E. . Rogacheva *et al.*, "Influence of oxidation on the transport properties of IV–VI-thin films," *Phys. E Low-dimensional Syst. Nanostructures*, vol. 17, pp. 310–312, Apr. 2003.

[163] E. I. Rogacheva, I. M. Krivulkin, O. N. Nashchekina, A. Y. Sipatov, V. V. Volobuev, and M. S. Dresselhaus, "Effect of oxidation on the thermoelectric properties of PbTe and PbS

epitaxial films," *Appl. Phys. Lett.*, vol. 78, no. 12, p. 1661, Mar. 2001.

[164] A. Stoesser *et al.*, "Facile fabrication of electrolyte-gated single-crystalline cuprous oxide nanowire field-effect transistors," *Nanotechnology*, vol. 27, no. 41, p. 415205, Oct. 2016.

[165] K. C. Pradel, W. Wu, Y. Zhou, X. Wen, Y. Ding, and Z. L. Wang, "Piezotronic Effect in Solution-Grown p-Type ZnO Nanowires and Films," *Nano Lett.*, vol. 13, no. 6, pp. 2647–2653, Jun. 2013.

[166] J. Tang *et al.*, "Single-crystalline Ni2Ge/Ge/Ni2Ge nanowire heterostructure transistors.," *Nanotechnology*, vol. 21, no. 50, p. 505704, 2010.

[167] G. A. Li, C. Y. Wang, W. C. Chang, and H. Y. Tuan, "Phosphorus-Rich Copper Phosphide Nanowires for Field-Effect Transistors and Lithium-Ion Batteries," *ACS Nano*, vol. 10, no. 9, pp. 8632–8644, 2016.

[168] W. Kim, A. Javey, O. Vermesh, Q. Wang, Y. Li, and H. Dai, "Hysteresis Caused by Water Molecules in Carbon Nanotube Field-Effect Transistors," *Nano Lett.*, vol. 3, no. 2, pp. 193–198, Feb. 2003.

[169] C. M. Aguirre *et al.*, "The Role of the Oxygen/Water Redox Couple in Suppressing Electron Conduction in Field-Effect Transistors," *Adv. Mater.*, vol. 21, no. 30, pp. 3087–3091, Aug. 2009.

[170] H.-S. Kang, C.-S. Choi, W.-Y. Choi, D.-H. Kim, and K.-S. Seo, "Characterization of phototransistor internal gain in metamorphic high-electron-mobility transistors," *Appl. Phys. Lett. Appl. Phys. Lett. Appl. Phys. Lett.*, vol. 84, no. 93, pp. 203506–23310, 2004.

[171] M. Buscema *et al.*, "Photocurrent generation with two-dimensional van der Waals semiconductors," *Chem. Soc. Rev.*, vol. 44, no. 11, pp. 3691–3718, May 2015.

[172] R. R. LaPierre, M. Robson, K. M. Azizur-Rahman, and P. Kuyanov, "A review of III–V nanowire infrared photodetectors and sensors," *J. Phys. D. Appl. Phys.*, vol. 50, no. 12, p. 123001, Mar. 2017.

[173] J. Kim *et al.*, "Optical properties and bridge photodetector integration of lead sulfide nanowires," *Nanotechnology*, vol. 28, no. 47, p. 475706, Nov. 2017.

[174] X. Fang *et al.*, "High-Performance Blue/Ultraviolet-Light-Sensitive ZnSe-Nanobelt Photodetectors," *Adv. Mater.*, vol. 21, no. 48, pp. 5016–5021, Dec. 2009.

[175] M. Constantinou *et al.*, "Interface Passivation and Trap Reduction via a Solution-Based Method for Near-Zero Hysteresis Nanowire Field-Effect Transistors.," *ACS Appl. Mater. Interfaces*, vol. 7, no. 40, pp. 22115–20, Oct. 2015.

[176] D. B. Straus, E. D. Goodwin, E. A. Gaulding, S. Muramoto, C. B. Murray, and C. R. Kagan, "Increased Carrier Mobility and Lifetime in CdSe Quantum Dot Thin Films through Surface Trap Passivation and Doping.," *J. Phys. Chem. Lett.*, vol. 6, no. 22, pp. 4605–9, Nov. 2015.

[177] J. Goldberger, D. J. Sirbuly, M. Law, and P. Yang, "ZnO nanowire transistors.," *J. Phys. Chem. B*, vol. 109, no. 1, pp. 9–14, Jan. 2005.

[178] D. M. Balazs *et al.*, "Stoichiometric control of the density of states in PbS colloidal quantum dot solids," *Sci. Adv.*, vol. 3, no. 9, p. eaao1558, Sep. 2017.

[179] O. Voznyy, D. Zhitomirsky, P. Stadler, Z. Ning, S. Hoogland, and E. H. Sargent, "A charge-orbital balance picture of doping in colloidal quantum dot solids.," *ACS Nano*, vol. 6, no. 9, pp. 8448–55, Sep. 2012.

[180] Z. Sun, Z. Liu, J. Li, G.-A. Tai, S.-P. Lau, and F. Yan, "Infrared photodetectors based on CVD-grown graphene and PbS quantum dots with ultrahigh responsivity.," *Adv. Mater.*, vol. 24, no. 43, pp. 5878–83, Nov. 2012.

[181] D. Zhang, D. Z.-R. Wang, R. Creswell, C. Lu, J. Liou, and I. P. Herman, "Passivation of CdSe Quantum Dots by Graphene and MoS2 Monolayer Encapsulation," *Chem. Mater.*, p. 150619100737000, Jun. 2015.

[182] Y. Kim, H. Ko, and B. Park, "Interfacial dynamic surface traps of lead sulfide (PbS) nanocrystals: Test-platform for interfacial charge carrier traps at the organic/inorganic functional interface," *J. Phys. D. Appl. Phys.*, vol. 51, no. 14, p. 145306, Apr. 2018.

[183] M. Egginger, S. Bauer, R. Schw?diauer, H. Neugebauer, and N. S. Sariciftci, "Current versus gate voltage hysteresis in organic field effect transistors," *Monatshefte f?r Chemie - Chem. Mon.*, vol. 140, no. 7, pp. 735–750, Jul. 2009.

[184] C. Ucurum, H. Goebel, F. A. Yildirim, W. Bauhofer, and W. Krautschneider, "Hole trap related hysteresis in pentacene field-effect transistors," *J. Appl. Phys.*, vol. 104, no. 8, p. 084501, Oct. 2008.

[185] C. Ucurum, H. Siemund, and H. Göbel, "Impact of electrical measurement parameters on the hysteresis behavior of pentacene-based organic thin-film transistors," *Org. Electron.*, vol. 11, no. 9, pp. 1523–1528, Sep. 2010.

[186] G. Gu, M. G. Kane, J. E. Doty, and A. H. Firester, "Electron traps and hysteresis in pentacene-based organic thin-film transistors," *Appl. Phys. Lett.*, vol. 87, no. 24, pp. 1–3, Dec. 2005.

[187] A. Carlson, A. M. Bowen, Y. Huang, R. G. Nuzzo, and J. A. Rogers, "Transfer printing techniques for materials assembly and micro/nanodevice fabrication," *Advanced Materials*. 2012.

[188] T. S. Mentzel *et al.*, "Nanopatterned electrically conductive films of semiconductor nanocrystals," *Nano Lett.*, vol. 12, no. 8, pp. 4404–4408, Aug. 2012.

[189] R. S. Park *et al.*, "Hysteresis in Carbon Nanotube Transistors: Measurement and Analysis of Trap Density, Energy Level, and Spatial Distribution.," *ACS Nano*, Mar. 2016.

[190] R. Vogel, P. Hoyer, and H. Weller, "Quantum-sized PbS, CdS, Ag2S, Sb2S3, and Bi2S3 particles as sensitizers for various nanoporous wide-bandgap semiconductors," *J. Phys. Chem.*, vol. 98, no. 12, pp. 3183–3188, Mar. 1994.

[191] Y. Cho *et al.*, "Balancing Charge Carrier Transport in a Quantum Dot P–N Junction toward Hysteresis-Free High-Performance Solar Cells," *ACS Energy Lett.*, vol. 3, no. 4, pp. 1036–

1043, Apr. 2018.

[192] B.-S. Kim *et al.*, "High Performance PbS Quantum Dot/Graphene Hybrid Solar Cell with Efficient Charge Extraction," *ACS Appl. Mater. Interfaces*, vol. 8, no. 22, pp. 13902–13908, Jun. 2016.

[193] Y. Cho *et al.*, "Charge Transport Modulation of a Flexible Quantum Dot Solar Cell Using a Piezoelectric Effect," *Adv. Energy Mater.*, vol. 8, no. 3, p. 1700809, Jan. 2018.

[194] A. Wolcott *et al.*, "Anomalously Large Polarization Effect Responsible for Excitonic Red Shifts in PbSe Quantum Dot Solids," *J. Phys. Chem. Lett.*, vol. 2, no. 7, pp. 795–800, Apr. 2011.

[195] S. Coe-Sullivan, J. S. Steckel, W.-K. Woo, M. G. Bawendi, and V. Bulović, "Large-Area Ordered Quantum-Dot Monolayers via Phase Separation During Spin-Casting," *Adv. Funct. Mater.*, vol. 15, no. 7, pp. 1117–1124, Jul. 2005.

[196] M. V. Jarosz, N. E. Stott, M. Drndic, N. Y. Morgan, M. A. Kastner, and M. G. Bawendi, "Observation of Bimolecular Carrier Recombination Dynamics in Close-Packed Films of Colloidal CdSe Nanocrystals," *J. Phys. Chem. B*, vol. 107, no. 46, pp. 12585–12588, Nov. 2003.

[197] B. Ullrich and H. Xi, "Photocurrent limit in nanowires.," *Opt. Lett.*, vol. 38, no. 22, pp. 4698–700, 2013.

[198] Y. Zhang *et al.*, "Charge Percolation Pathways Guided by Defects in Quantum Dot Solids.," *Nano Lett.*, Apr. 2015.

[199] I. Hwang, C. R. McNeill, and N. C. Greenham, "Drift-diffusion modeling of photocurrent transients in bulk heterojunction solar cells," *J. Appl. Phys.*, vol. 106, no. 9, p. 094506, Nov. 2009.

[200] C. R. McNeill, I. Hwang, and N. C. Greenham, "Photocurrent transients in all-polymer solar cells: Trapping and detrapping effects," *J. Appl. Phys.*, vol. 106, no. 2, p. 024507, Jul. 2009.

[201] S. A. McDonald *et al.*, "Solution-processed PbS quantum dot infrared photodetectors and photovoltaics.," *Nat. Mater.*, vol. 4, no. 2, pp. 138–42, Feb. 2005.

[202] D. J. Beesley *et al.*, "Sub-15-nm patterning of asymmetric metal electrodes and devices by adhesion lithography," *Nat. Commun.*, vol. 5, no. 1, p. 3933, Dec. 2014.

[203] G. Wyatt-Moon, D. G. Georgiadou, J. Semple, and T. D. Anthopoulos, "Deep Ultraviolet Copper(I) Thiocyanate (CuSCN) Photodetectors Based on Coplanar Nanogap Electrodes Fabricated via Adhesion Lithography," *ACS Appl. Mater. Interfaces*, vol. 9, no. 48, pp. 41965–41972, Dec. 2017.

[204] J. Semple, S. Rossbauer, and T. D. Anthopoulos, "Analysis of Schottky Contact Formation in Coplanar Au/ZnO/Al Nanogap Radio Frequency Diodes Processed from Solution at Low Temperature," *ACS Appl. Mater. Interfaces*, vol. 8, no. 35, pp. 23167–23174, Sep. 2016.

[205] J. Semple *et al.*, "Large-area plastic nanogap electronics enabled by adhesion lithography," *npj Flex. Electron.*, vol. 2, no. 1, p. 18, Dec. 2018.

[206] M. A. Lampert, "Simplified theory of space-charge-limited currents in an insulator with traps," *Phys. Rev.*, vol. 103, no. 6, pp. 1648–1656, Sep. 1956.

[207] M. A. Green, *Solar Cells: Operating Principles, Technolgoy, and System Applications*. Prentice-Hall, Inc.,Englewood Cliffs, NJ, 1982.

[208] A. Maulu *et al.*, "Strongly-coupled PbS QD solids by doctor blading for IR photodetection," *RSC Adv.*, vol. 6, no. 83, pp. 80201–80212, Aug. 2016.

[209] C. Hu *et al.*, "The micropatterning of layers of colloidal quantum dots with inorganic ligands using selective wet etching," *Nanotechnology*, vol. 25, no. 17, p. 175302, May 2014.

[210] V. Nandwana *et al.*, "Direct patterning of quantum dot nanostructures via electron beam lithography," *J. Mater. Chem.*, vol. 21, no. 42, p. 16859, Oct. 2011.

[211] M. A. Meitl *et al.*, "Transfer printing by kinetic control of adhesion to an elastomeric stamp," *Nat. Mater.*, vol. 5, no. 1, pp. 33–38, Dec. 2005.

[212] T.-H. Kim *et al.*, "Kinetically controlled, adhesiveless transfer printing using microstructured stamps," *Appl. Phys. Lett.*, vol. 94, no. 11, p. 113502, Mar. 2009.

[213] M. K. Choi *et al.*, "Wearable red–green–blue quantum dot light-emitting diode array using high-resolution intaglio transfer printing," *Nat. Commun.*, vol. 6, p. 7149, May 2015.

[214] D. Qin, Y. Xia, and G. M. Whitesides, "Soft lithography for micro- and nanoscale patterning," *Nat. Protoc.*, vol. 5, no. 3, pp. 491–502, 2010.

[215] G. Konstantatos *et al.*, "Ultrasensitive solution-cast quantum dot photodetectors," *Nature*, 2006.

[216] K. Mathew *et al.*, "MPInterfaces: A Materials Project based Python tool for high-throughput computational screening of interfacial systems," *Comput. Mater. Sci.*, 2016.

[217] D. Zherebetskyy, "Colloidal nanoparticle of lead sulfide (selenide) with complete passivation," 2014. [Online]. Available: https://en.wikipedia.org/wiki/Quantum_dot#/media/File:Colloidal_nanoparticle_of_lead_sulfide_(selenide)_with_complete_passivation.png. [Accessed: 18-Feb-2019].